EXPERIMENTAL AND THEORETICAL HEAT TRANSFER STUDIES IN VACUUM ARC REMELTING

Laxmappa G. Hosamani

B. E., K. R. E. C., Surathkal, India, 1973
M. Tech., I. I. T., Bombay, India, 1975

A dissertation submitted to the faculty
of the Oregon Graduate Center
in partial fulfillment of the
requirement for the degree
Doctor of Philosophy
in
Materials Science and Engineering

April, 1988

The dissertation "Experimental and Theoretical Heat Transfer Studies in Vacuum Arc Remelting" by Laxmappa G. Hosamani has been examined and approved by the following Examination Committee:

William E. Wood, Thesis Advisor
Professor and Chairman
Department of Materials Science and Engineering

Jack H. Devletian
Professor
Department of Materials Science and Engineering

David G. Atteridge
Associate Professor
Department of Materials Science and Engineering

V.S. Rao Gudimetla
Assistant Professor
Department of Applied Physics
and Electrical Engineering

DEDICATION

This dissertation is dedicated to my father whom I lost during its completion.

ACKNOWLEDGEMENTS

I wish to express my gratitude to Professor W. E. Wood for his advice and encouragement throughout this work. I am grateful to Drs. J. H. Devletian, D. G. Atteridge and Rao Gudimetla for examining my thesis. I am also grateful to Pacific Power and Light for financial support, Oregon Metallurgical Corporation and Special Metals Corporation for providing the equipment and materials. I thank Mr R. B. Turpin and Mr G. H. Boehme for their help in various stages of this work. I am also grateful to Dr. Frank Zanner of Sandia National Laboratories for his advice during the course this work. I also would like to thank Vivek Dikshit, Tyrus Monson and Ashok Advani for their help in preparing this manuscript.

TABLE OF CONTENTS

LIST OF FIGURES

LIST OF TABLES

ABSTRACT

EXPERIMENTAL AND THEORETICAL HEAT TRANSFER STUDIES IN VACUUM ARC REMELTING

Laxmappa G. Hosamani, Ph. D.
Oregon Graduate Center, 1988

Supervising Professor: Dr. William E. Wood

Vacuum arc remelting is the most important and dominant remelting process in the production of double vacuum melted superalloys and titanium alloys for the aerospace industry. Also there is an increased demand for larger and better quality vacuum arc melted ingots of these alloys. However, as the size of the ingot increases, the tendency for segregation increases. This is due to deeper molten metal pool, deeper mushy zone and longer local solidification time. These in turn are influenced by the electrode melt rate and the cooling condition of the ingot. The segregation can be minimized either by decreasing the melt rate or by improving the heat transfer from the ingot. The former technique results in decreased productivity and increased energy consumption during melting. Hence, the latter technique is preferred. The heat transfer from the ingot can be increased by introducing a gas of high thermal conductivity like helium in the shrinkage gap between the ingot and crucible. This technique was patented and is being used by superalloys manufacturers, but, no systematic study has been carried out to quantify the effect of helium gas pressure. Hence the present exper-

imental work was under taken to study the effect of helium gas pressure on the heat extraction rate, metal pool depth, solidification structure, mushy zone size and segregation.

The experiments were carried out in a laboratory vacuum arc furnace. Temperature measurements were made on the outside surface of 165 mm diameter crucible by imbedding 18 electrically insulated, chromel/alumel thermocouples along the length of the crucible. The heat flux distribution on the outside surface of the crucible were then computed, and an increase in helium gas pressure resulted in a increased heat flux removal by the cooling water. A theoretical model for heat transfer by gas conduction between the ingot and crucible was derived from the first principles and the heat transfer coefficients were calculated from the model at various gas pressures. The effect of helium gas pressure on molten metal pool depth, dendrite arm spacing (DAS), mushy zone size, Laves phase distribution and segregation for Inconel- 718 were studied. The increase in helium gas pressure resulted in a decreased molten metal pool depth. For example with 60 mm of helium gas pressure, the pool depth decreased from 200 mm to 127 mm i.e. about 36% decrease. The calculated mushy zone sizes using the DAS measurements showed decrease in mushy zone size with the helium gas cooling. Also the amount Laves phase formed was decreased with gas cooling. Hence, with gas cooling technique between the ingot and crucible, it is possible to minimize segregation in large size ingots.

1. INTRODUCTION

Vacuum arc remelting (VAR) is a secondary melting process used to produce ingots of reactive metals and their alloys, like titanium and zirconium, and segregation sensitive alloys like superalloys and special steels. The main competitors for the vacuum arc remelting process are Electro slag remelting (ESR), Electron beam remelting (EBR) and Plasma arc remelting (PAR). These processes essentially involve the remelting of a consumable electrode in a water cooled copper crucible, producing an ingot which solidifies, continuously, from the bottom upwards. The impetus for the development of these processes has been the need for high performance, high purity materials required for aerospace applications. The main advantages of these remelting techniques are reduced inclusion and gas contents, reduced macro- and micro-segregation, higher yield and general property reproducibility. These characteristic properties are achieved due to the limited molten metal pool produced during remelting conditions, thereby providing a means to closely control ingot solidification rates and thus influence and control segregation and the chemical refining of the molten metal either by slag reaction, as in ESR or by processing under vacuum, as in VAR or EBR.

Vacuum arc remelting is the most important and dominant remelting process in the production of double vacuum melted advanced superalloys which must meet extremely stringent specifications for their use in rotating engine parts

and many other critical applications. The double vacuum remelting process consists of vacuum induction melting (VIM) to produce an alloy of the specified composition followed by vacuum arc remelting (VAR) for cleanliness and ingot structure control. Vacuum arc remelting is still the widely used melting process for producing the ingots of reactive metals, although, other melting processes are slowly gaining acceptance and are being used to produce ingots from sponge and scrap.

The present day vacuum arc remelting practice for superalloys involves typically, making ingots of 432 mm (17") to 508 mm (20") in diameter and weighing up to 2700 kgs (6000 lbs) to 4500 kgs (10,000 lbs), respectively (1). Even larger diameter forging stock is desirable. However, beyond 400 mm, ingots of superalloys, like Inconel 718, are increasingly prone to gross segregation of niobium, known as "freckles" in forged billets and articles, unless solidification is adequately controlled. Similarly, the demand for high strength and high temperature capability titanium alloys is increasing in aerospace applications. These high strength titanium alloys are highly alloyed and prone to segregation.

It has been shown (2-6) that the flow of solute rich interdendritic liquid in the mushy zone is responsible for most types of macro-segregation. The movement of this interdendritic liquid occurs as a result of solidification contraction, gravitational force acting on a liquid of variable density and electromagnetic forces. The magnitude of the fluid flow in the interdendritic region depends on the depth of molten metal pool and mushy zone size. High power input results in a deeper metal pool and deeper mushy zone size, which enhances the interdendritic liquid flow. The problem becomes more severe as the ingot size increases.

The technique generally used to minimize segregation is to melt at lower power inputs, hence at lower melt rates, resulting in a shallower molten metal pool and mushy zone. Lower melt rates lead to higher energy consumption per kg. of the ingot and lower productivity of the plant. Hence, it is necessary to examine other techniques to minimize segregation without decreasing the melt rate. One technique which comes to mind immediately is the cooling condition of the ingot. By increasing the cooling rate of the ingot, it should be possible to reduce the molten metal pool depth and the mushy zone depth, resulting in reduced segregation.

Hence electrode melt rate and ingot cooling conditions are the two most important factors influencing the solidification structure and severity of segregation in VAR ingots. Although several investigations (7-9) have been carried out to study the operating parameters affecting the melt rate, no systematic models have been developed for melt rate as a function of operating variables. Recently Zanner et al (10) have developed a model for melt rate based on experiments conducted in production shops. The present work focuses on developing models for melt rate and metal pool depth based on laboratory size melts and then verifying these models with production size melts.

The other factor influencing the segregation is the cooling condition of the ingot. In order to increase the cooling rate, it is necessary to understand the heat transfer mechanism from the ingot to the cooling water in vacuum arc remelting. As the ingot solidifies, it shrinks and pulls away from the crucible wall, creating a gap between the ingot and the crucible. As the melting is carried out in vacuum, the gap is essentially a vacuum gap. In this condition, the ingot-

crucible system may be regarded as a "Vacuum Flask" in which, with the exception of a narrow contact band at the top part of the ingot, heat transfer is effected mainly by radiation.

Heat transfer studies conducted on continuous casting crucibles show (11) that, the air gap between the ingot and the crucible constitutes the largest resistance, being 84 % of the total, while the crucible wall and cooling water interface account for only 2 % and 14 % of the total respectively. The mechanisms of heat transfer in continuous casting crucible can be compared to that of vacuum arc remelting, except for the air gap instead of a vacuum gap, which is still worst. In vacuum arc remelting, the temperature drop across the ingot-crucible interface is about 1000°C, and this exceeds the temperature drop in the crucible wall by a factor of 20. Hence, changes in the crucible wall thickness or an increase in water flow rate would not greatly increase the heat transfer rate in vacuum arc remelting.

The heat transfer rate in vacuum arc remelting is controlled by the heat transfer coefficient between the ingot and the crucible. If substances having a good thermal conductivity are introduced in the gap between the ingot and the crucible, the heat transfer from the ingot to the crucible can be substantially increased. Examples of such substances are gasses of high thermal conductivity like hydrogen and helium. Helium is in fact ideal for this purpose, as it has a high thermal conductivity, is non explosive and does not react with remelted material. With helium gas in the gap between the ingot and the crucible, the heat transfer takes place by radiation and by gas conduction, resulting in increased heat transfer rate. The contact between the crown and the crucible

forms a seal which prevents leakage of the helium gas. Hence, by regulating the helium gas pressure, it is possible to vary the cooling rate of the ingot within a certain range.

The idea and technique of introducing helium gas into the gap between the ingot and the crucible during vacuum arc remelting was patented by Joseph M. Wentzell (12) and the patent was assigned to Special Metals Corporation, New Hartford, New York. Even though this technique is being used by superalloy manufacturers on a regular basis, no experimental investigation has been carried out to understand the effect of helium gas cooling on heat extraction rate, metal pool depth, solidification structure, mushy zone size and segregation. Hence this investigation was undertaken to study experimentally and theoretically the effect of helium gas cooling between the ingot and crucible on heat transfer rate, metal pool depth, solidification structure and segregation in VAR ingots.

2. LITERATURE SURVEY

2.1. Historical Background of Vacuum Arc Remelting

In 1839, Robert Hare described an arc furnace before the American Philosophical Society (13). It is generally regarded as the first controlled atmospheric arc furnace and included most of the essentials of a modern furnace, i.e., a movable electrode, a hearth capable of retraction, provision for evacuation and for backfilling with a selected gas and good visibility. The final step in the development of the vacuum arc furnace consisted of the introduction of a water cooled crucible and is attributed to Von Bolton (7). The ideas and principles established by Hare and Von Bolton were applied sporadically as experimental techniques until about 1937, when the M. W. Kellog Company utilized the "Cold Crucible" principle in the Hopkins or "electric ingot" process to produce high quality alloy steels. During the same period, work was initiated by several investigators, which eventually led to the present day developments. Noted among these investigators was Dr. Wilhelm Kroll who established the necessary technique for melting titanium. Parke and Ham, in 1943, used a vacuum arc furnace to melt molybdenum. Members and staff at the Bureau of Mines, Albany, Oregon (7), have also made significant contributions to the development of this technique for melting zirconium and titanium.

>From 1940's to the present day, the equipment design and melting practices have been steadily improved. Since 1970, research work has been underway at Sandia National Laboratories, Albuquerque, New Mexico, to understand the basics of metal vapor arc and its coupling with the metallurgy of the process. Arc physics and behavior, metal transfer and electrode gap measurement, boundary conditions on the crucible wall, pool dynamics and macro-segregation have been studied (14-21). The experimental ingots ranged from large industrial ingots of 510 mm diameter to small laboratory ingots of 155 mm diameter.

2.2. VAR Process Principles.

A schematic of the VAR process is shown in Figure 2.1. The process involves remelting of an electrode in a water cooled crucible at low pressures. Heat is generated by the application of a low voltage and high current arc between the electrode and the surface of the molten metal pool. As the metal droplets pass through the arc, they are exposed to vacuum at extremely high temperatures, producing extensive de-gassification as well as breakdown and dispersion of the inclusions. The process basically involves the following four stages : a) Melting of the electrode tip; b) Transfer of metal droplets to pool through vacuum; c) Collection of metal in liquid pool; d) Solidification and build up of ingot. The main advantages of vacuum arc melted steels and superalloys over conventional air melted materials are: elimination of center porosity, improved cleanliness and minimized segregation. Reactive metals like titanium and zirconium and their alloys are melted in vacuum arc furnace due to their chemical reactivity.

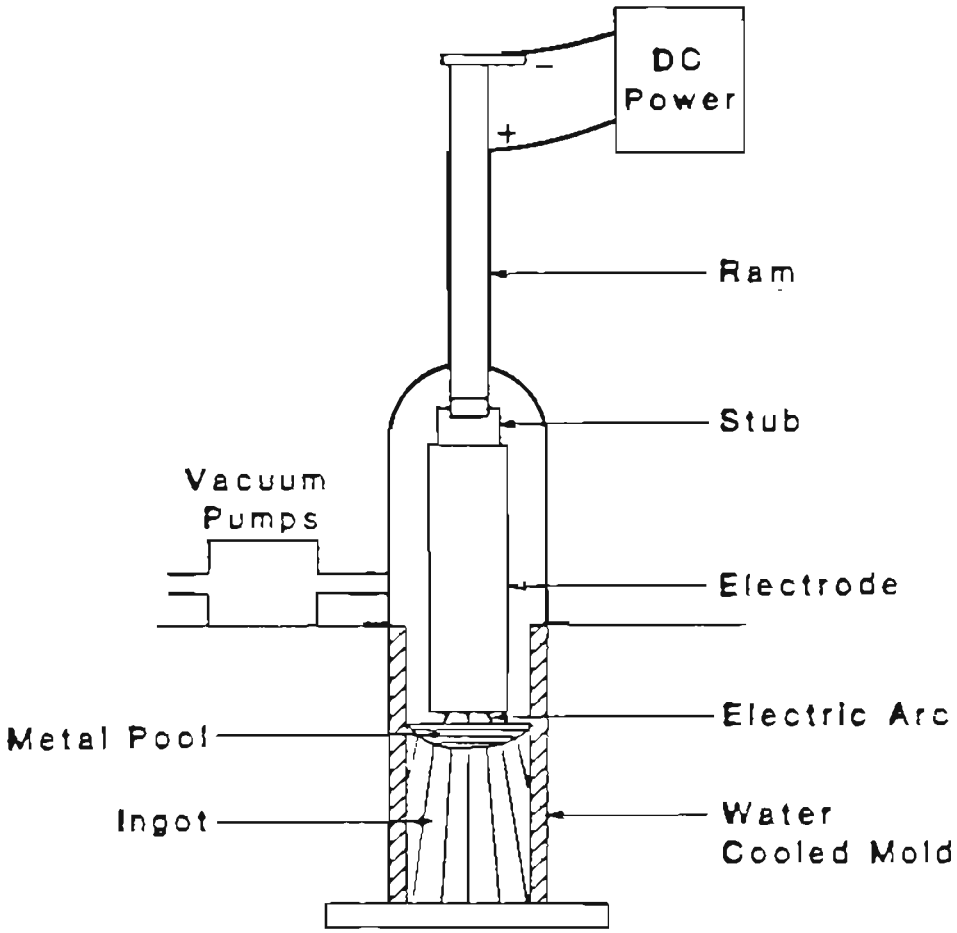

Figure 2.1. Schematics of VAR Process.

2.3. Melting techniques

The vacuum arc process starts with a consumable electrode having the required overall composition of the final product. For titanium and its alloys, the electrodes are formed by pressing blended sponge and alloying elements in compacting dies to form briquettes or compacts. These compacts are assembled into an electrode and usually welded by plasma, metal inert gas or electron beam methods (22). The welded electrode is suspended in the vacuum arc furnace. After closing the chamber, the furnace is evacuated. The arc is usually struck on either a small pile of sponge or a briquette of suitable size and shape. Generally, the arc is struck with a low power and power is increased to the required level after stabilization of the process. The titanium ingots are normally double-melted. Some specifications require triple-melting. Double- and triple-melting reduce the chances of the occurrence of macro-segregation.

Maximum current levels used in titanium melting industrial furnaces are in the range of 500-1000 Amperes per inch of the crucible diameter (23). This maximum current directly affects the melting rate, depth of the molten pool, surface condition and internal quality of the ingot (with respect to segregation). During the final melt, hot tapping is always done in order to get maximum yield and minimum shrinkage cavities.

The vacuum arc remelting process for steels and superalloys differs from that for titanium in that the electrode preparation is different. Generally, the electrodes for steels and superalloys are cast into slightly tapered molds (24). Some surface conditioning of the cast electrode is required which, depending on the material and final quality standards, may consist of shot blasting, wire

brushing, grinding or machining. Trimming of the top and bottom end is generally required. Normally, lower current levels are used during melting of superalloys, as they are prone to segregation.

2.4. Solidification Structure and Melt Rate in VAR

2.4.1. Segregation in VAR Ingots

The ultimate properties of the vacuum arc remelted material depend largely upon the structure and homogeneity of the ingot. These in turn depend on the depth of the molten metal pool and the mushy zone size, which are controlled during the remelting process by the rates of solidification and melting. In vacuum arc remelting process, electrode melting and ingot solidification occur simultaneously. Since an increase in the melt rate results in an increased molten metal pool depth where as an increase in the solidification rate results in a decreased molten metal pool depth, these parameters may be regarded as having opposite effects.

The rate of solidification depends on the intensity of heat transfer from the ingot to the crucible and is, at the same time, a function of the melt rate. Hence, melt rate and the cooling conditions should be controlled carefully to achieve the desired ingot structure and homogeneity in VAR ingots. This is especially important in case of segregation sensitive superalloys like Inconel 718. Typical segregation problems for Inconel 718 are, freckles and white spots. Freckles are rich in niobium and contain significant amounts of Laves phase. The size of freckles is much larger than the dendrite arm spacing of as cast ingots. Also the solid state diffusion rate of niobium is negligible. The combined effect of size factor and diffusion rate makes freckles virtually unremovable by

any amount of thermomechanical processing. The effect of freckles on mechanical properties is therefore detrimental. Eiselstein (25) showed that specimens containing freckles had a yield strength of approximately 120,000 psi, as compared to the normally expected value of 150,000 psi. Ductility of such specimens was also poor. Hence, an important objective is to minimize the occurrence of freckles in Inconel 718.

Research work done at Massachusetts Institute of Technology (2-6) has shown that the flow of solute rich interdendritic liquid in the mushy zone during solidification is responsible for most types of macro-segregation. Since the interdendritic liquid is rich in solute, its physical displacement can lead to considerable solute redistribution and result in macro-segregation. This flow of solute rich interdendritic liquid is caused primarily by two driving forces (26). The first is the solidification shrinkage which causes the interdendritic liquid to flow towards solidus isotherm in order to satisfy continuity. The second driving force is gravity which causes convection since the density varies within the interdendritic liquid. The other less important driving forces are bulk liquid convection and electromagnetic forces (26,27).

The calculation of the interdendritic liquid flow caused by solidification shrinkage and gravity, and the resulting macro-segregation was first performed by Mehrebian et al (6). In general, for predicting macro-segregation, the pressure distribution in the mushy zone is calculated initially from the measured shape of mushy zone, cooling rate and the properties of the semisolid alloy. Once the pressure distribution is known, the velocity of the interdendritic liquid in the mushy zone is calculated using D ' Arcy's law. Then, the solidification equations

(26) are used to calculate the local average composition.

Macro-segregation in consumable electrode remelted ingots has also been described by Mehrebian et al (28) as shown in Figure 2.2. If interdendritic liquid flow lines are vertical, as in Figure 2.2a., and under steady state heat flow and solidification, no segregation results across the ingot. Hydrodynamic considerations do not permit this simple flow pattern. If liquid density is constant, then flow lines fan outward, as shown in Figure 2.2b. In this case the interdendritic liquid flow (from hotter to cooler regions), is largest near the centerline of the ingot, and negative segregation results at that location. If the density of the interdendritic liquid increases during solidification, then flow lines fan inward (from cooler to the hotter regions) as shown in Figure 2.2c, and positive segregation results near the centerline of the ingot.

S. Kou et al (29) studied the effect of mushy zone depth and solidification rate on macro-segregation in ESR ingots. Macro-segregation increases with increasing depth of mushy zone and decreasing solidification rate (higher local solidification time). Local solidification time is given by mushy zone depth/solidification rate. The higher the solidification rate, the smaller is the local solidification time. The operating conditions which favor a deep mushy zone and longer solidification time are the major causes of macro-segregation. A deeper molten metal pool always results in a deeper mushy zone. The deeper metal pool is the result of higher melt rate and slower cooling conditions. According to macro-segregation theory (26), the main reason why a deep mushy zone causes more macro-segregation in VAR ingots is that the solute rich interdendritic liquid flow can be strongly affected by the solidification shrinkage and

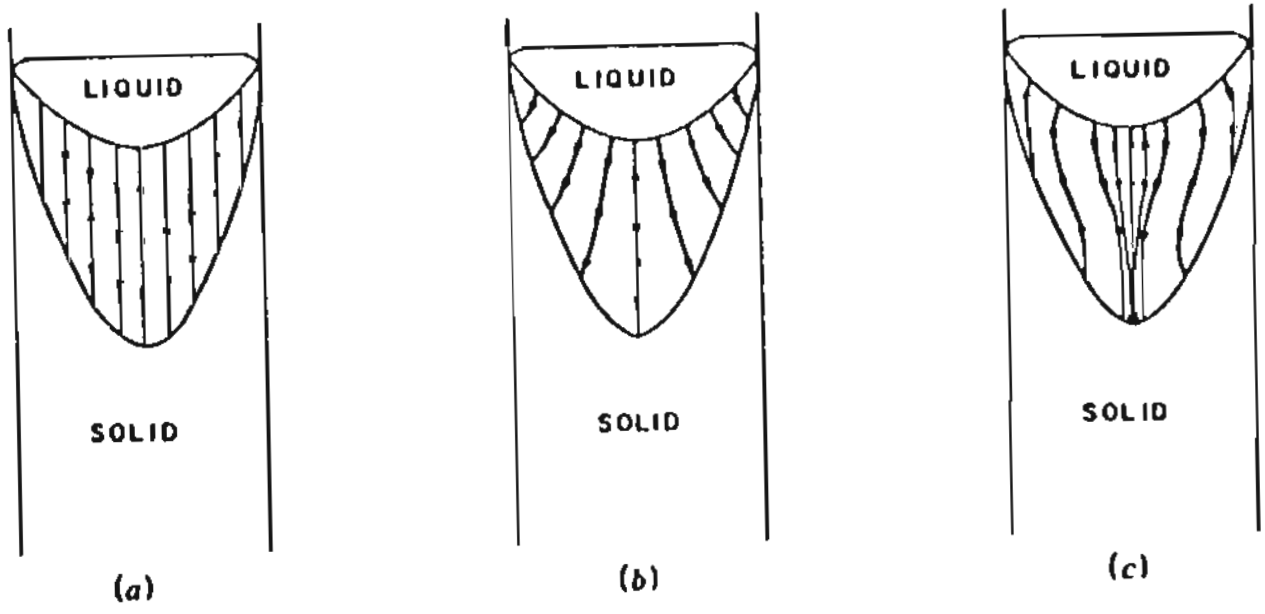

Figure 2.2. Interdendritic fluid flow in consumable electrode or continuous casting: a) limiting case, all flow vertical; no segregation , b) flow resulting in negative segregation, c) flow resulting in positive segregation (28).

gravity in a deep mushy zone. Hence, it is necessary to understand the factors affecting the molten metal pool depth and the mushy zone size. Numerous workers (30-37) have examined ESR and VAR ingots with a view towards relating the molten metal pool, mushy zone size and the solidification structure with the melt rate.

2.4.2. Effect of Melt Rate on Solidification Structure

DeVaries and Mumau (30) investigated the relationship between the secondary dendrite arm spacing and the melt rate for several alloys. They reported an increase in the secondary dendrite arm spacing with an increase in the melt rate. The dendrite arm spacing also increased with an increase in the ingot cross sectional area and to some extent, with the complexity of the alloy. The decrease in dendrite arm spacing with the decreased melt rate is effective in reducing segregation and provides a significant improvement in property uniformity. Niimi et al (31) also reported that, for a large ESR ingot of carbon steel, the dendrite arm spacing decreased with the decrease in melt rate.

Holzgruber (32) investigated the effect of ingot size and melt rate on dendrite arm spacing and macro-segregation during electroslag remelting of Cr-Ni-Mo low alloy steels. The dendrite arm spacing was found to increase with increasing ingot size as observed by DeVaries. With an increase in the diameter of the ingot, the latent heat of solidification has to be conducted away from the solidification front through a thicker layer of solid material which in turn results in a lower temperature gradient in front of and behind the liquid/solid interface. This lower temperature gradient, together with the lower local rate of solidification in larger ingots results in an increase in the metals residence time in

the two phase region which leads to an increase in the secondary dendrite arm spacing. The dendrite arm spacing close to the surface of the ingot was not strongly effected by the increase in melt rate. However, dendrite arm spacing in the mid-radius and center position increased with the increase in melt rate up to 500 kg/hr and after that, further increases in the melt rate resulted in decreased dendrite arm spacing, ie, a maximum dendrite arm spacing was observed at some intermediate melt rate and surprisingly this corresponded to lowest in microsegregation.

Dewsnap and Schlatter (33) investigated the effect of melt rate on solidification of high carbon tool steels. It was found that cell size of carbide network decreases with increasing melt rate. They also concluded that there is an optimum intermediate melt rate range which assured satisfactory carbide segregation ratings which is in agreement with the observation made by Holzgruber (32). At lower and higher melt rates, carbide segregation ratings decreased.

K. O. Yu and co-workers (27,34) reported that the dendrite arm spacing decreased with an increase in the melt rate. The difference between dendrite arm spacings in the ingot at the center and surface also decreased with increased melt rates. The higher melt rate resulted in a deeper metal pool and a deeper mushy zone as expected. With a deeper metal pool the heat extraction rate increased and hence local cooling rate might have increased resulting in a decreased dendrite arm spacing.

From the above discussion, it is clear that the influence of melt rate on ingot structure seems to be contradictory. This may be due to the fact that the relationship between melt rate and ingot structure is a complicated phenomenon

involving other parameters like molten metal pool shape and cooling conditions.

P.O. Mellberg (35) conducted experiments on the electroslag remelting process to understand the effect of various process parameters on the average cooling rate. Cooling rate increased slightly with increasing melt rate but depended mainly on the molten metal pool shape. According to Mellberg, the average cooling rate at the center of the ingot, for the case where molten metal pool shape has a small liquid metal contact area is higher, as compared to the one with a large liquid metal contact area. The molten metal pool with a large contact area has small temperature differences within the metal pool, while larger temperature gradients are maintained if the contact area is small. Hence, this may explain some of the differences between the various results discussed above on the effect of melt rate on the ingot structure, viz, the dendrite arm spacing.

2.4.3. Melt Rate and Mushy Zone Size

Suarez et al (36) investigated the effect of melt rate and ingot size on the mushy zone size and the local solidification time and the effect of these on segregation during electroslag remelting of Inconel 706. The main objective of their investigation was to determine whether local solidification time or the depth of mushy zone is the predominant factor in forming freckles. Computer predictions and experimental results were used in their analysis. The mushy zone size calculated from the computer model for 25, 30 and 40 inches diameter ingots did not change significantly at the same melt rate. But, the local solidification time calculated for the 40 inch diameter ingot was almost double the value calculated at a similar melt rate for the 25 inch diameter ingot. The experimental ingots of 40 inch diameter at intermediate melt rate did not have any freckles and the

optimum melt rate with respect to the macrostructure was the same as that of the 25 inch diameter ingot. Hence, it was inferred that the predominant factor in the formation of freckles is the depth of the mushy zone rather than the local solidification time. The effect of the melt rate on the mushy zone depth was also analyzed. At low melt rates the mushy zone depth remained fairly constant, but as the melt rate increased, the mushy zone became deeper at an increasing rate.

Jeanfils et al (37,38) carried out a computer prediction of the effect of melt rate on molten metal pool depth and mushy zone depth. The higher the melt rate, the deeper are the molten metal pool and the mushy zone, and the steeper is the slope of the isotherms. It has also been shown that the response of change in metal pool and mushy zone depth to changes in the melt rate is slow. The pool depth reached a maximum 10 -15 minutes after the melt rate has reached a maximum and the mushy zone depth lagged behind the melt rate by 30 minutes.

K. O. Yu et al (27,34) calculated the mushy zone depth from the dendrite arm spacing measurements during vacuum arc remelting of Inconel 718. The mushy zone depth increased with increasing melt rate. It has been reported that the tendency for freckle type segregation is more for ESR ingots than for VAR ingots. The reason is due to the difference in the molten metal pool profile, mushy zone depth and the slope of the isotherms.

Mitchell and Smailer reported (39) that the local solidification time at steady state is a complex function of melt rate and not a monotonic function of the melt rate. There is an intermediate melt rate under which the local solidification time is minimum and dendrite arm spacing is finest. This suggests that two ingots of the same alloy can be produced at different melt rates but experience the same

local solidification time at comparable locations. Since the pool characteristics in the two ingots would not be the same, the intensity of the mechanism driving the interdendritic fluid flow would differ, and the extent of macro-segregation would not be expected to be the same in the two ingots.

2.4.4. Factors Effecting Melt Rate

It is clear from the above discussion that the melt rate is an important factor in controlling the solidification structure and segregation in VAR ingots. At the same time, melt rate also influences the productivity of the furnace and the specific energy consumption. Hence it is necessary to understand the operating parameters effecting the melt rate.

Although a large amount of research work was carried out at the U.S. Bureau of Mines, Albany, Oregon, on vacuum arc remelting (7), no systematic study for the melt rate was done. K. Burgardt and K. Tromel (8), established the following equation for the melt rate,

$$VA=(0.6\times I)-b \tag{2.1}$$

Where,

VA = fusing rate in kg/min

I = current in kA

b = constant, the value of which is between 0.05 and 0.55.

This equation was probably developed for steels. It was reported (8) that, the above equation differs slightly in form from the equation given by F. Sperner and G. Persson, which was developed based on industrial melts.

They proposed a general equation for melt rate as a function of current :

$$A = K \times I \tag{2.2}$$

where, K assumes values between 0.5 and 0.7 depending upon the grade of the steel. However, in all of the above equations, melt rate is related to the current and no other variable.

V. V. Tetyukhin et al (9) defined an equation,

$$V = \frac{(-4 + I_g)}{60} \tag{2.3}$$

where,

V = melt rate in kg/sec

I_g = arc current in KA.

The above equation was developed based on the results of melting industrial ingots of 430 - 1000 mm in diameter for two phase titanium alloys. Again, in this particular study, melt rate is related only to the current.

The first experimental work to relate melt rate to all the other important operating variables has been carried out very recently by Zanner et al (10) for Inconel 718. They conducted statistically designed experiments in two different production shops. 406 mm diameter electrodes were vacuum arc remelted into 457 mm diameter ingots. Approximately, 11000 kgs of Inconel 718 were melted. A regression model for melt rate (M) given below was developed using a stepwise regression method :

$$\begin{aligned} M = {} & -3.50 \pm 14.6 + 1.9 \text{ (arc power in kW)} \\ & -0.0033 \text{ ((arc power) (CO pressure in microns))} \\ & -0.0115 \text{ ((arc power) (electrode gap in mm))} \pm 24.0 \end{aligned} \tag{2.4}$$

The above model has a standard error of $\pm$ 24 kg/hr based on an overall average

melt rate of 235 kg/hr. This model has interactive terms, viz, arc power - CO pressure and arc power - electrode gap. The model shows that the melt rate is decreased by increasing the pressure of CO and the electrode gap and the decrease becomes greater as the arc power is increased. They related this to the change in arc behavior and mode of metal transfer.

2.4.5. Factors Effecting Molten Metal Pool Depth

As discussed in the earlier sections, the degree of macro-segregation depends on the pool depth, mushy zone size and local solidification time. Longer solidification times and deeper mushy zones result in severe macro-segregation. A deeper metal pool always results in a deeper mushy zone. Hence, it is necessary to understand the factors influencing the molten metal pool depth and the models developed for metal pool. The size and shape of the molten metal pool is a result of the rate of heat input in to the metal pool (melt rate), the rate of heat out of the ingot and various losses.

The earliest model (8) for molten metal pool profile is based on the assumption that the metal pool resembles a paraboloid of revolution with a height l_{max}, (equal to the depth of the metal pool measured at its center).

$$l_{max} = \frac{0.8 \times V}{\pi \times D^2} \tag{2.5}$$

where,

V = volume of the molten pool in cm^3

D = diameter of the basal surface in cm.

Bungardt and Vollmer (8) developed an expression for metal pool depth as a function of melting current :

$$l_{max}=3.58\times I \tag{2.6}$$

where I is current in kA. The voltage was assumed to be constant at 25 V. Bungardt and Tromel (8) derived an equation based on their results of the form :

$$l_{max}=5.72\times(I^{0.745}) \tag{2.7}$$

The above equation shows that the molten metal pool depth increases with the current, but not linearly. This is attributed to the fact that the energy distribution in the arc, the anode temperature and consequently the radiation losses vary with increased current.

V. V. Tetyukhin et al (9) obtained an equation for quasi-steady state pool depth for titanium alloys of the form :

$$H=5V \tag{2.8}$$

where,

H = depth of pool in m

V = mass rate of melting in kg/sec

$$V=\frac{(-4+Ig)}{60} \tag{2.9}$$

where,

Ig = current in kA.

The above equations for titanium alloys were developed from industrial ingots in the range of 430 -1000 mm in diameter. It has been reported that the metal pool in the top part of the ingot has the shape of a cylinder passing into a paraboloid. The cylindrical part of the pool is known as the 'contact zone'. The height of the contact zone depended upon the current and V. V. Tetyukhin et al (9) reported that the length of the contact zone approaches values of 100 - 200 mm for ingots 430mm in diameter and 300 - 400 mm for those 750 mm in diameter.

They observed the highest crucible temperatures, at the contact zone level, 250–280°C on the inner surface and 150°C on the outer surface.

Dobatkin and Musatov (40) have developed an equation for the steady state molten metal pool depth for titanium alloys based on the analysis of the thermal processes occurring during solidification :

$$H = k \times (I - s) \times U \tag{2.10}$$

and

$$k = \frac{g + c\left(t_l - \frac{t_m + t_n}{2}\right)}{4\pi\lambda(t_m - t_n)} \tag{2.11}$$

where,

H = depth of the pool in m,

s = part of heat flow over the axis of the ingot

g = melting heat in kJ/kg,

c = heat capacity kJ/kg/°K

t_l = mean temperature of the liquid metal in K

t_m = melting point in K.

t_n = temperature of the lateral surface of the ingot in K.

λ = heat conductivity in kJ/m/sec/°K

U = mass velocity of filling the mold in kg/sec

R = radius of the ingot in m.

The above equation shows that the depth of the metal pool is proportional to the mass velocity of filling the crucible, i.e. the melt rate. The proportionality constant ' k ' depends on the thermophysical characteristics of the metal, the

diameter and the rate of heat transfer between the ingot and the crucible. For titanium alloy ingots from 0.2 to 1.0 m in diameter, it has been reported (40) that,

$$s=0.0015(1+5D)(D/U)^2 \tag{2.12}$$

$$K=5(1-0.25D) \tag{2.13}$$

where,

D = diameter of the ingot in m

U = rate of filling the crucible in kg/sec.

Dobatkin and Musatov (40) have also reported that, the profile of the pool changes from a cup shaped form to a conical form at higher melt rates according to :

$$h/H=(\rho/R)^2 \tag{2.14}$$

where, h and ρ are the co-ordinates of the point on the curve defining the profile the pool. It has also been reported (40) that the calculated pool depths for ingot diameters up to 850 mm differ from the measured pool depths by about 10%, at maximum.

Molten metal pool shape and size studies were also carried out at the Bureau of Mines, Albany, Oregon (7) during zirconium melting. The effect of individual parameters, viz, power, vacuum level and polarity were studied. Pool size increased as the power level increased. The pool broadened and increased in depth as the furnace pressure decreased, hence, it was concluded that, molten metal pool volume is a direct function of the melt rate. The polarity had no significant effect on the pool depth. With reverse polarity, the metal pool tended to be narrower and contained less metal. The molten metal pool with alternating

current seemed to be a compromise between straight and reverse polarities. Zanner and Bertram (19) have shown that for U - 6% Nb alloy, the metal pool volume varied linearly with the current.

2.5. Heat Transfer in VAR

2.5.1. Heat Transfer in VAR - General

The other factor influencing the depth of molten metal pool and mushy zone size is the cooling condition of the ingot. By increasing the cooling rate of the ingot, it is possible to decrease the depth of metal pool and mushy zone resulting in minimized segregation. In order to increase the cooling rate of the ingot, it is necessary to understand the heat transfer characteristics in VAR process. Relatively little work has been done on the heat transfer characteristics in VAR.

Experimental work (7) was carried out at the U. S. Bureau of Mines to understand the effect of melting parameters on the maximum heat flux and heat flux distribution along the crucible length. Heat transfer studies were conducted during non-consumable electrode melting and also during consumable electrode melting. The crucibles were divided into several pieces along the vertical direction and each piece had its own water cooling jacket and the average values of the heat flux in each piece were determined. The rate of heat transfer along the length of the crucible varied over a wide range of values of heat flux, with the high values of heat flux near the top of the ingot where molten metal from the pool splashes against the crucible wall. Melts with extremely long arcs indicated the existence of two areas of high wall temperatures above the ingot top. These two areas of high temperature coincided with the excessively high crowns formed during melting with long arcs.

The rate of heat transfer was greatly reduced along the lower portion of the ingot, where solidification and cooling of the ingot resulted in a shrinkage gap between the crucible and the ingot. Heat transfer rates were also relatively low above the ingot, where radiation from the hot electrode, the arc and the molten pool contributed heat to the crucible wall. The effect of melting current, voltage, electrode diameter and electrode material on heat flux distribution were studied. In general, increasing the current increased the maximum heat flux. Increasing the voltage increased the maximum heat flux and shifted the location of the maximum heat flux nearer to the top of the ingot. For a given crucible diameter, higher heat flux occurred with larger diameter electrodes and an increase in the electrode diameter shifted the peak heat flux upwards. The results of the study confirmed the existence of a high thermal resistance between the ingot and the crucible which results from the shrinkage of the ingot as the metal solidifies.

The ongoing research work on vacuum arc remelting, since the 1970's, at Sandia National Laboratories, involved the measurement of boundary conditions on the crucible wall (15). The experimental set-up consisted of an array of 40 stainless steel sheathed, electrically insulated, chromel-alumel thermocouples embedded in the outer surface of a copper crucible to measure its temperature during the course of melting. Attempts to measure the temperature of the inside surface of the crucible were not successful. The heat flux distribution on the outside of the crucible were estimated from the measured temperatures (on the outside), and inside fluxes were obtained by solving the inverse heat flow problem. The total flux extracted by the coolant was about 90% of the power input. About half of this flux was deposited above the molten metal pool. It was con-

cluded (15) that most of the deposition came from recombination and thermal radiation. The other half of the total heat flux came from below the pool. It was shown that, in order to capture all the significant heat flux, the temperature measurements have to be made up to 75 cms on either side of the molten metal pool. The peak temperature on the crucible wall was very close to the pool position, indicating that the contact zone was confined to a very small region near the meniscus of the pool.

2.5.2. Heat Transfer with Gas Cooling

The heat transfer rate between the ingot and the mold during ingot casting under vacuum and various gas atmospheres was studied by H. Jacobi (41). The investigation was carried out in a vacuum induction furnace using a mold lined with porous alumina bricks. One wall was equipped with a vertical water cooled copper-chill plate, thus approaching one dimensional heat flow. Experiments were carried out using different gas atmospheres, viz, Ar, N_2, CO, O_2, H_2S, He and H_2. From measurements of heat flux densities and ingot surface temperatures, the heat transfer coefficients in the gap region were calculated. The heat transfer coefficient values were the lowest in vacuum conditions as expected, where the heat transfer was only by radiation. The values then increase in proportion to the increasing thermal conductivity of the gas. Thus, the maximum values were found for hydrogen gas. The values of average heat flux taken between one and five minutes after the start of pouring were, 8.7 $cal/cm^2/sec$ in vacuum, 11.9 $cal/cm^2/sec$ in argon, 17.87 $cal/cm^2/sec$ in helium and 18.0 $cal/cm^2/sec$ in hydrogen atmospheres. The use of hydrogen as compared to vacuum reduced the overall solidification time by almost one half. Theoretical

heat flux densities due to radiation and due to gas conduction were calculated and were in good agreement with experimentally measured values.

Folk and Wunnenburg (42) studied the heat transfer along a continuous casting mould by dividing the mould into eight horizontal water passages and measuring the water quantity and raise in the water temperature for each. As expected, the heat flux varied with height and the pattern varied with casting speed. In addition, the heat flux was found to increase considerably towards the bottom of the mould. It was indicated that, this was due to the penetration of water from the secondary cooling sprays into the space between the casting and the mould, where, it dissociated into hydrogen and FeO, producing a hydrogen rich gas which exhibits excellent thermal conductivity. This pattern agrees remarkably well with the more recent work at Nippon (74) with thermocouples in the mould wall. This phenomenon was observed independent of the particular casting operation.

Cliff and Dain (43) used the Hill's integral profile technique to study the effect of various parameters on heat flux during continuous casting. One of the parameters studied was the injection of hydrogen gas into the gap between the ingot and the mould. Hydrogen in the gap increased the heat transfer rates, it also had undesirable effects such as higher mould wall temperatures at the meniscus. They have reported (43) an inner mould wall temperature at the meniscus of the metal pool of about 886°C with hydrogen in the gap as against 261°C with just air in the gap. However, these results were not verified by any experimental investigation.

The idea and the technique of introducing helium gas into the gap between

the ingot and the crucible during vacuum arc remelting was patented by Joseph M. Wentzell (12) and it was assigned to Special Metals Corporation, New Hartford, N.Y. According to the patent, it is possible to minimize segregation effectively by injecting helium gas into the gap between the ingot and the crucible. The helium gas is injected at the bottom of crucible into the gap. It has been shown (12) that the crucible outlet water temperature increased due to the injection of helium gas into the gap as compared to no gas in the gap region, indicating that the heat extraction rate is increased due to the helium gas in the gap. Although this technique is being used by superalloy manufacturers on a regular basis, no systematic study has been carried out to quantify the effect of helium gas cooling on heat extraction rate, metal pool depth, mushy zone depth and segregation in VAR ingots.

Boyarshinov and Gotin (44,45) investigated the effect of helium gas between the ingot and the crucible, for nickel and iron - nickel base alloys during vacuum arc remelting. The heat transfer coefficient in the gap increased more than two times by the introduction of helium gas in the gap. However, the investigation was not systematic, in that, the heat extraction rate as a function of helium gas pressure was not carried out.

They derived an empirical relation for maximum possible helium pressure which ensures a high rate of ingot cooling without causing bubbles of the gas to penetrate the bath, as given below :

$$p(\tau) \approx L_c = k\{H(\tau) - H_0\} \qquad (2.15)$$

where,

Lc = extent of contact zone and is proportional to the bath depth

Ho = depth of the bath corresponding to the formation of the contact zone

k = constant depending on the VAR practice and the properties of the material

τ = the time from the beginning of melting.

The molten metal pool depth is related to operating parameters by :

$$H(\tau)=k_1(I-I_0)(1-e^{-A}\tau) \tag{2.16}$$

The maximum pressure of the helium in the gap is determined by the expression for different times during melting as :

$$p(\tau)=p_0(1-e^{-A}\tau) \tag{2.17}$$

where τ is the time from the moment at which the formation of the bath terminates.

Depending on remelting conditions and grade of the steel, the pressure of helium gas varied from 15 mm to 60 mm of Hg. They have reported the development of an automatic regulator for varying the pressure of helium during the melt. The gas consumption was about 60 - 120 liters/hr and the vacuum level in the melting zone was about 1 micron, indicating that there was no increase in the pressure in the melting zone. The molten metal pool depth and mushy size decreased with gas cooling. It is also claimed (44,45) that, with helium gas cooling, the melt rate could be increased by about 20 - 60 % and energy consumption could be decreased by 6 - 8 %.

K. O. Yu (46) theoretically calculated the heat transfer coefficient by gas conduction between the ingot and the crucible. It was shown that, the heat transfer coefficient was dependent on the gas pressure, the gap width between the

ingot and the crucible and the thermal conductivity of the gas. As the helium gas pressure was increased from 10 to 20 and then to 30 mm of Hg, the over all heat transfer coefficient increased by about 40 % and 65 % respectively. Ballantyne (47,48) has reported computer simulation of VAR process with helium gas between the ingot and crucible. Only a limited number of simulation runs, one with 1 mm of helium pressure and the other with 10 mm of helium pressure have been reported (47). The predicted metal pool and mushy zone size decreased with the helium gas cooling. Since no experimental investigation was carried out, the predicted metal pool depth and mushy zone depth were not verified.

2.5.3. Heat Transfer Studies on Gas Conduction in Other Areas of Science and Engineering

Numerous investigators have carried out analytical and experimental work (49-56) on the problem of heat transfer in a rarefied gas confined between parallel plates, concentric cylinders and concentric spheres. In all these experiments, heat conducted through the gas was measured as a function of gas pressure. In particular, heat conduction through rarefied gasses contained between two concentric cylinders has been used most often to measure thermal conductivities and accommodation coefficients of gasses. A typical experimental set-up consisted of an inner cylinder, a fine tungsten wire whose temperature and power loss were determined by passing a known current through it. The outer cylinder was pyrex glass maintained at a constant temperature by an oil bath. The average temperature of the filament was determined by measuring its resistance. At each pressure, the heat conduction between the filament and the outer cylinder was determined.

The principle that heat transfer between a heated filament and a nearby wall is pressure dependent in a certain pressure ranges has been utilized in thermal conductivity gauges. At high pressures, the heat transfer is independant of pressure except for a small convection effect. At a few millibar of pressure, where the mean free path of the gas is of the same order of magnitude as the filament diameter, the heat transfer through the gas surrounding the filament becomes dependent upon the pressure. This continues to be so until low pressures of about 10^{-3} millibar. Below this pressure, heat transfer by gas conduction ceases and heat transfer takes place by radiation which is independent of pressure. The sensing filament in the gauge head forms one branch of a wheatstone bridge. This filament is heated by a constant current. With increasing gas pressure the temperature of the filament decreases because of the greater heat transfer through the gas, so that the bridge becomes out of order. The bridge current serves as a measure of the gas pressure which is indicated on a meter.

3. OBJECTIVES

The objectives of this present study may be summarized as follows.

1) Installation and Instrumentation of a unique University based Vacuum Arc Remelting furnace system.

2) Develop regression models for melt rate and metal pool depth as a function of operating parameters.

3) Predict melt rate from the model and verify the validity of the models for production scale ingots.

4) Experimentally study changes in heat transfer characteristics in VAR induced by helium gas cooling between the ingot and crucible.

5) Develop a theoretical model for heat transfer coefficient due to gas conduction between the ingot and crucible and predict from the model.

6) Experimentally study the effect of helium gas cooling on:

   a) Molten metal pool depth and Mushy zone depth

   b) Solidification structure

   c) Segregation

4. EQUIPMENT AND EXPERIMENTAL PROCEDURE

4.1. Equipment

4.1.1. Vacuum Arc Furnace

The VAR furnace at the Oregon Graduate Center is a Leybold - Heraeus model L 200 h/III and was donated by the Oregon Metallurgical Corporation, Albany, Oregon. The furnace can be used for both consumable and non-consumable electrode melting. It is also possible to melt under inert gas. The Figure 4.1 and 4.2 show photographs of the layout of the furnace along with the control room. The sectional view of the furnace is shown in Figure 4.3. The furnace chamber is cantilever mounted on a supporting frame. The dust separator and the pumps are frame mounted. As a safety feature, the clean out port for the dust separator is spring loaded to serve as a blow-out port. A gear box is provided for lowering and raising the electrode, control of which is made from a remote control desk. Technical details regarding the furnace are given in Table 4.1.

The vacuum system consists of a roots pump and a rotary piston pump. The roots pump has a pumping speed of 1600 cu.meters/hr and the two stage rotary piston pump has a pumping speed of 90 cu.meters/hr. Both of these pumps are connected in series. At a later stage, when experiments were carried

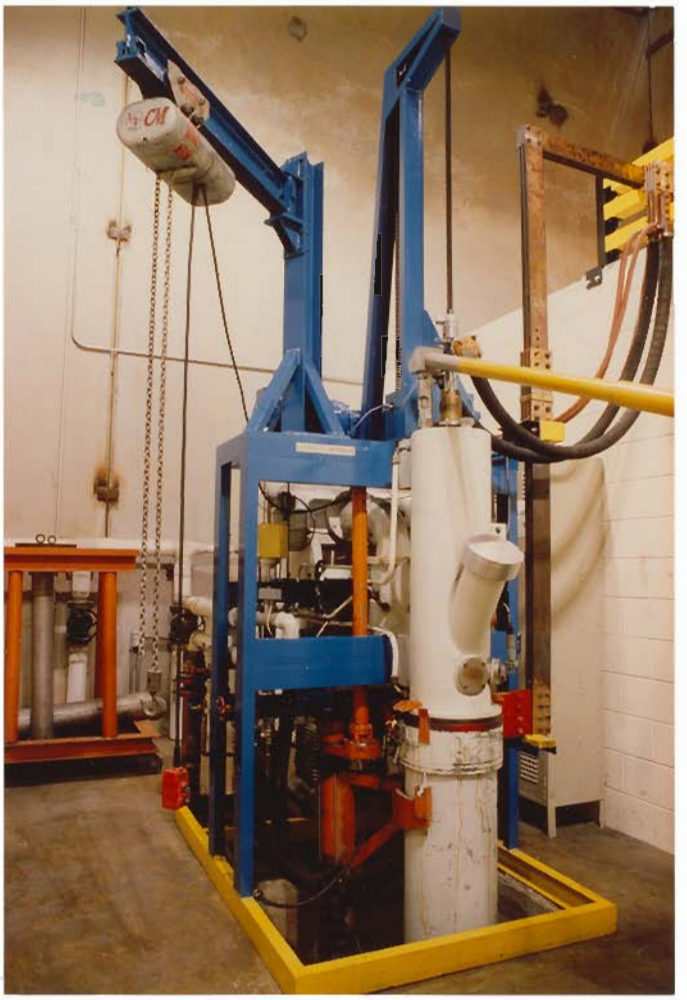

Figure 4.1. Vacuum Arc Furnace.

Figure 4.2. Vacuum Arc Furnace with control room.

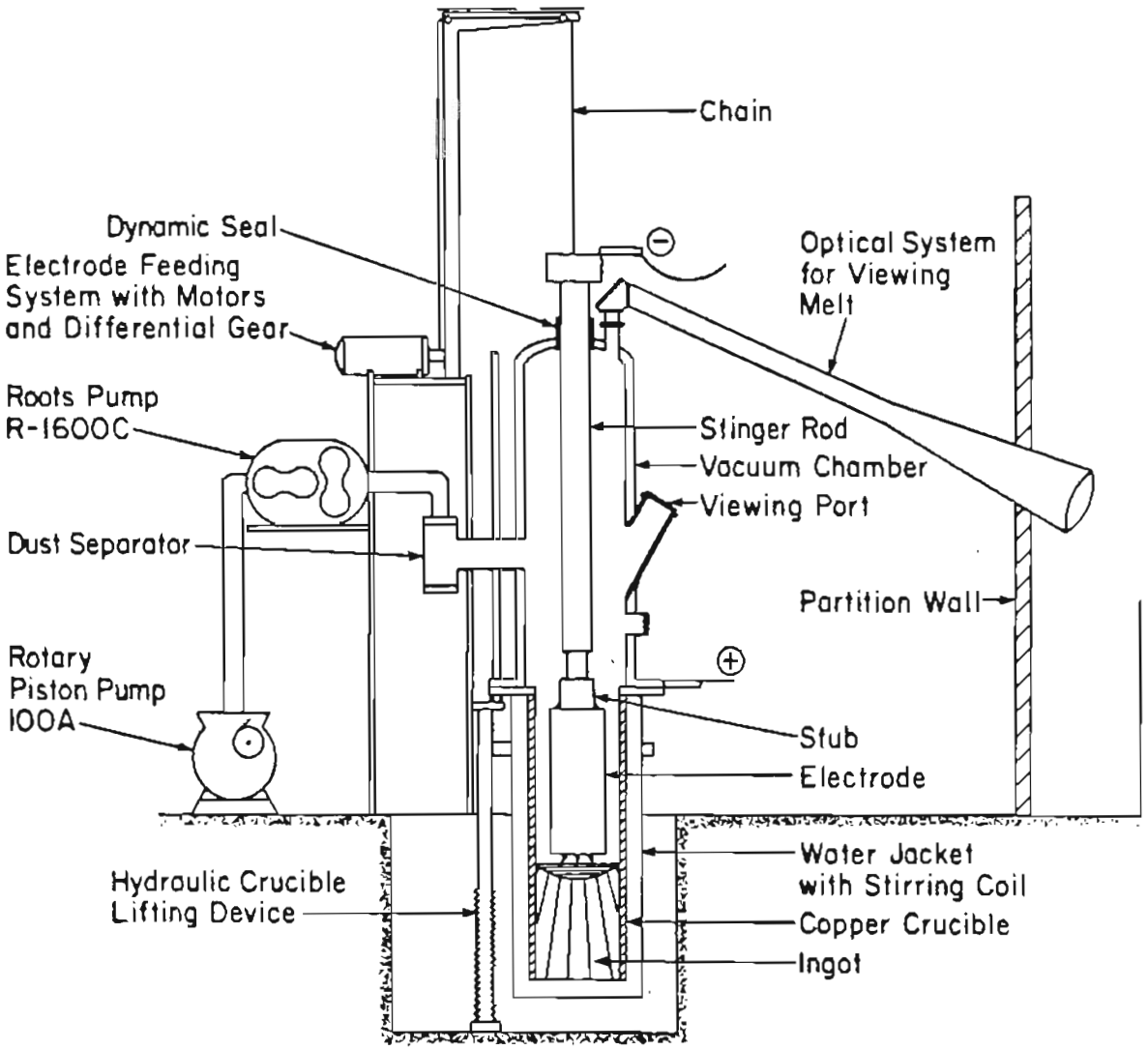

Figure 4.3. Sectional View of Vacuum Arc Furnace.

TABLE 4.1

TECHNICAL DETAILS OF VAR FURNACE

Maximum Crucible Diameter	208 mm (8.2")
Maximum Crucible Length	1067 mm (42")
Maximum Weight of Ingot	95 kgs. for Ti and 160 kg for steel
Stroke of Stinger Rod	1346 mm (53")
Final Vaccum	0.5 micron
Maximum Current	7500 Amps (D.C.)
Open Circuit Voltage	70-90 volts
Operating Voltage	25-30 volts

out with helium gas cooling, the rotary piston pump was replaced by a mechanical pump of higher capacity, viz, 250 cu.meters/hr. However, there did not seem to be much of an improvement in the vacuum level, either in the clean chamber or during melting. The vacuum level in the furnace chamber was measured with a Pirani gauge TM-230. The gauge has two ranges with automatic range switching. The power system consists of two rectifier systems each rated for 3750 amps and 80 volts open circuit.

Figure 4.4 shows the layout of the control room. All control and measuring instruments are located in the control room. The main control systems located in the control room are for the control of electrode feed, power supply, magnetic stirring, vacuum systems, helium/argon gas pressure, the data acquisition computer and a TV monitor.

4.1.2. Data Acquisition Computer

The furnace is equipped with a data acquisition Apple II+ computer with two disc drives. A Metrabyte corporation APM-08 was used for Analog and Digital control and a separate in-house design 8-bit digital I/O card was used to expand the needed digital output lines of the Metrabyte card. The Apple displays and saves on the disc the following informations: melting voltage, melting current, crucible cooling inlet and outlet water temperature, electrode position and the temperature readings of 15 thermocouples mounted on the crucible wall. The data could be displayed and stored at predetermined intervals and in this time interval, the data were taken 10 times and averaged. In the present experimental set up the time interval was 15 seconds. Hence, the chances of missing the peak temperatures on the crucible wall at such intervals of recording

Figure 4.4. Layout of control room.

were negligible.

4.1.3. Technique For Introducing Helium/Argon Gas In The Gap

It was decided to carry out all melting experiments in a 165 mm diameter crucible. Helium/Argon gas was introduced in the gap between the ingot and the crucible during melting through an inlet at the bottom of the crucible just above the bottom stool. The modification on the crucible for introducing the helium/argon gas was carried out by Zak Inc., New York. A stainless steel pipe of outer diameter 15.9 mm and inner diameter of 9.5 mm was laid along the length of the crucible. At the bottom of the crucible, a hole was drilled and the stainless steel pipe was welded. The pipe was taken out at the top of the crucible through the flange. Figure 4.5. shows the modification done on the crucible for introducing the helium/argon gas.

4.1.4. Instrumentation to Measure and Control Helium/Argon Gas Pressure

Figure 4.6. shows the layout of the instrumentation to measure and control helium/argon gas pressure in the gap between the ingot and the crucible. The main component of the system is the vacuum regulator. One side of the vacuum regulator was connected to the vacuum system and the other side to a gas cylinder. The inlet pressure from the gas cylinder to the vacuum regulator was maintained at about 20 psi. At that level, the regulator can control any vacuum down to 1 mm of Hg absolute. The regulator is equipped with a compound gauge. The vacuum portion shows the amount of vacuum below atmosphere (in mm of Hg), and the pressure portion shows the pressure above atmosphere (in

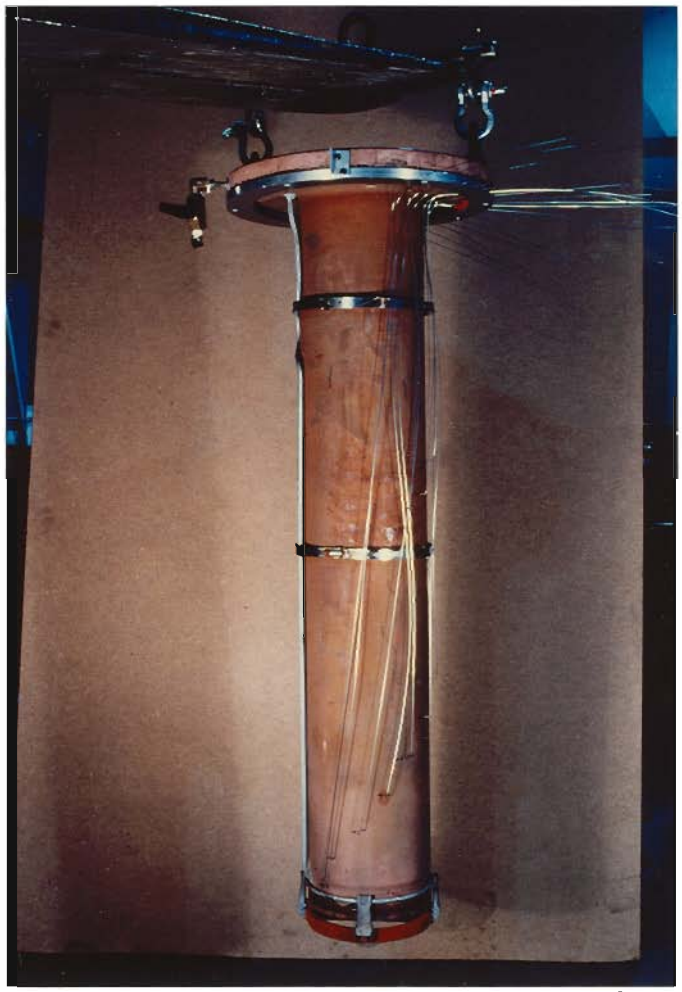

Figure 4.5. Modification on the crucible for introducing gas between the ingot and crucible.

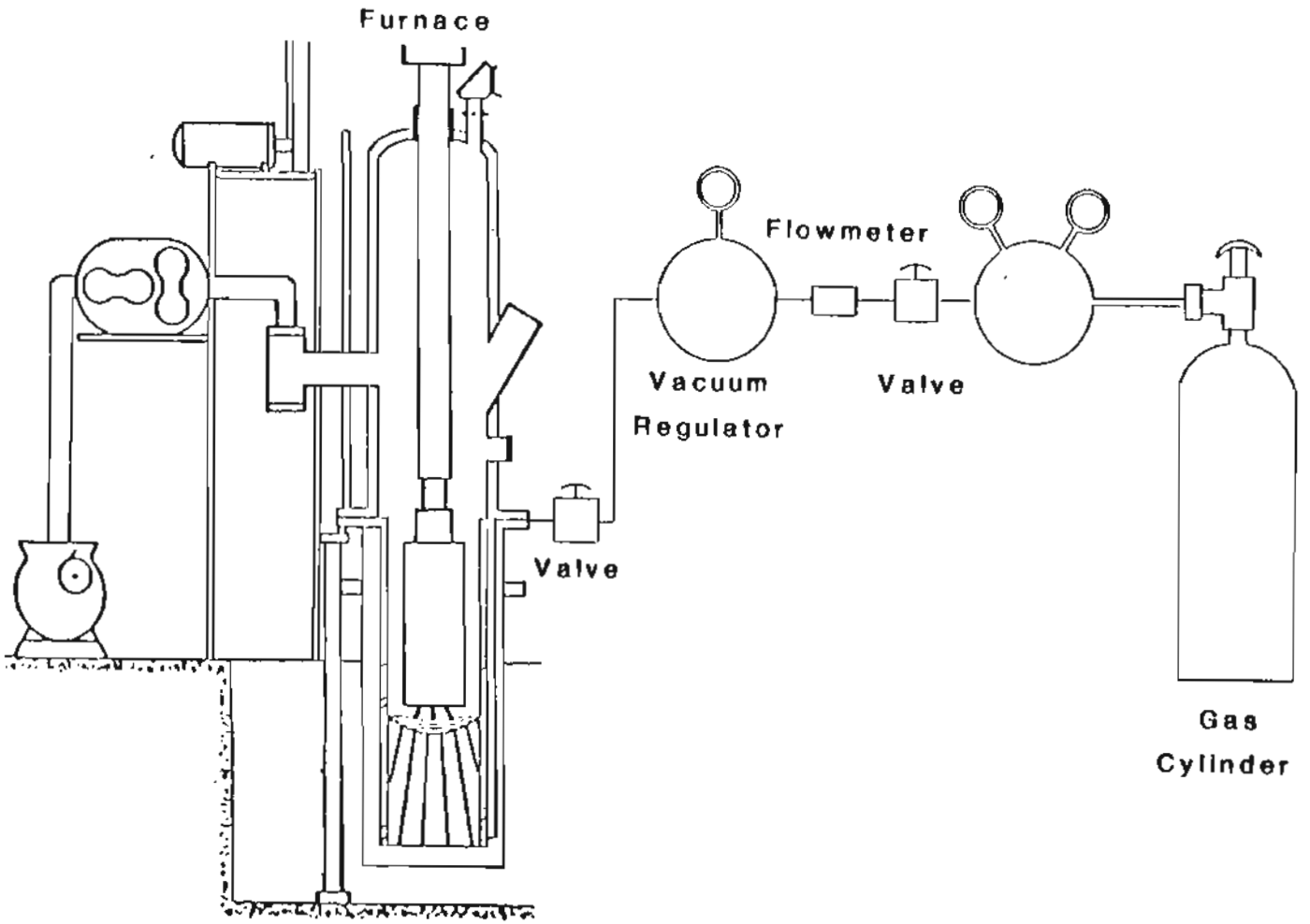

Figure 4.6. Layout of instrumentation to measure and control the gas pressure in the gap between the ingot and crucible.

kPa). At atmospheric pressure the needle shows zero regardless of the barometric pressure. Under full vacuum, the needle may be higher or lower than the 760 mm mark, depending on the barometric pressure. The barometric pressure in the experimental area was measured and it was found to be 760 mm Hg. The helium/argon gas pressure between the ingot and the crucible is the difference in the ambient barometric pressure which is 760 mm and the actual read out from the vacuum regulator. For example, at 740 mm reading on the vacuum gauge, the pressure of the gas in the gap is 20 mm Hg. By adjusting the knob on the vacuum regulator, it was possible to control the desired helium/argon gas pressure in the gap between the ingot and the crucible. The instrumentation also included a flow meter having a range of 0 - 2 LPM. The layout (Figure 4.6) shows two valves, one on the crucible and the other just beyond the vacuum regulator.

4.1.5. Assembly of the Thermocouples on the Crucible Wall

Measurement of temperature of the outside surface of the copper crucible during melting was one of the most difficult tasks. This was mainly due to the fact that the copper crucible carried current during melting and that could generate localized millivolt potentials of the same order as that generated by the thermocouples. In addition, during melting a magnetic field was applied to the molten metal pool for stirring, which may also influence the thermocouples reading. Therefore, the thermocouples had to be thermally coupled to, but electrically isolated from the crucible. There was also the other problem of taking out the thermocouple output terminals from the crucible to the data acquisition computer. Finally, thermocouples had to be arranged in such a way as to capture

most of the significant heat flux on the crucible wall during melting.

Two attempts were made to place the thermocouples on the outside of the crucible. In the first attempt, general purpose exposed junction chromel/alumel thermocouples were used. The thermocouples were mounted by drilling holes of 1.4 mm diameter and placing the thermocouple junction in the hole and peening the copper edges on it. Additionally, 4 more holes were punched around the hole, so that the peening was effective. Nineteen thermocouples were mounted on the crucible spirally. The first fifteen thermocouples were placed at a distance of 2.5 cm (1") from the bottom of the crucible, and the other 4 thermocouples were placed at a distance of 15 cm (6") in the upper half of the crucible surface. Two thermocouples were placed on the bottom surface of the bottom stool to determine the heat extracted from the bottom of the ingot. Four chromel/alumel thermocouples were also placed in the annulus between the crucible and the water guide tube to measure the bulk water temperature. All these thermocouples were laid along the crucible and were attached on to three steel clamps which were mounted on the copper crucible with the help of copper spacers as shown in Figure 4.7. The thermocouple leads were terminated on a switching circuit mounted on the bottom of the flange. Switching circuit was made watertight with RTV silicone rubber. A single output wire was taken out of the crucible through a slot at the bottom of the flange. The entire thermocouple assembly was made electrically floating by an isolated amplifier. This was confirmed by making electrode short circuit with the bottom plate as well as by applying a magnetic field and observing the changes, if any, in the thermocouple readings. No significant change in the thermocouple readings were noticed, implying

Figure 4.7. Crucible with chromel/alumel thermocouples on it (First attempt).

that the system was electrically isolated. Unfortunately, after a few melts, the RTV failed and water leaked into the switching circuit. Hence, the whole assembly had to be removed. The experience gained in this attempt was utilized, however, in the second attempt. It was observed that during the quasi-steady state condition, negligible amount of heat was extracted from the bottom of the ingot. Hence, the thermocouples on the bottom stool were removed. Besides it was noticed that, there was no significant difference in the bulk water temperature along the height of the crucible, hence the thermocouples placed in the water were removed.

In the second attempt, electrically isolated 1 mm (0.04"), diameter stainless sheathed chromel/alumel thermocouples were mounted on the outside of the crucible. In this case, 18 thermocouples were placed on the crucible wall and none on the bottom stool and in the bulk water as discussed earlier. A stainless steel ring of 12 mm (1/2") thickness, 39.5 cm (15.5") outer diameter and 31.75 cm (12.5") inner diameter was bolted to the bottom surface of the flange. Eighteen holes of 1.2mm diameter were drilled in the steel ring horizontally, through which the thermocouple leads were taken out, as shown in Figure 4.8. This time the thermocouples were placed at a distance of 5 cm (2"), from the bottom of the crucible except at 30.5 cm (12"), where the distance between the thermocouples was 12 mm (1/2") for three thermocouples. This arrangement was done to measure the temperature on the crucible wall when the metal pool was passing through quasi-steady state. The thermocouples were mounted on the crucible wall in the same way as they were in the first attempt. A supporting frame was bolted to the crucible flange on which the thermocouples were tied as shown in

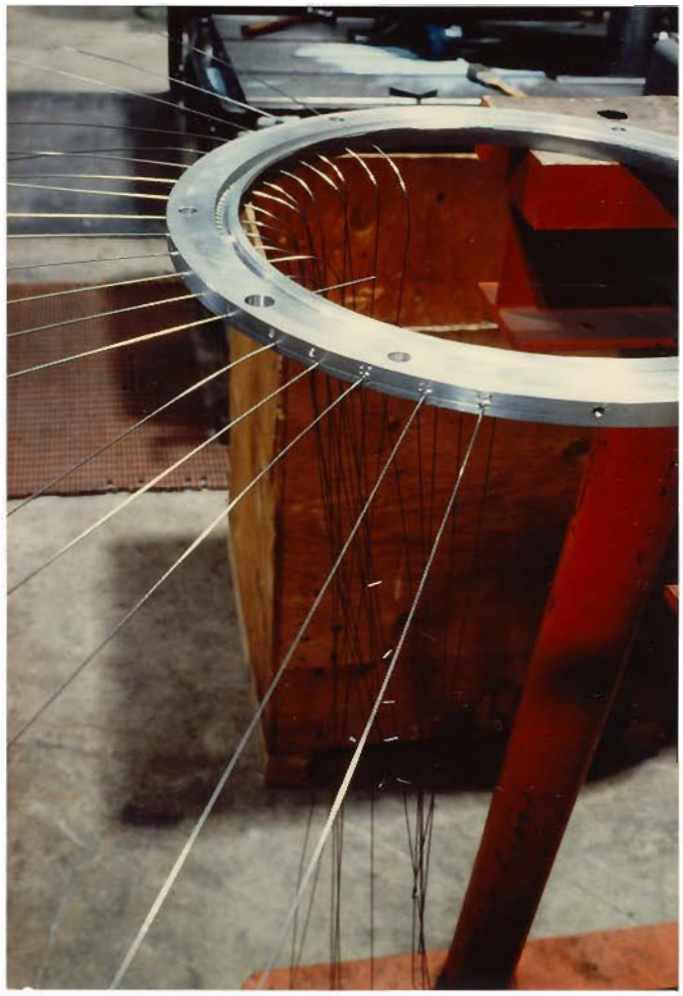

Figure 4.8. Steel ring with thermocouples.

Figure 4.9.

The thermocouple lead wires were connected to a reed relay multiplexer mounted in a box assembly. The output from the reed relay were fed into an analog device AD 595 monolithic thermocouple type K (chromel/alumel) amplifier with built in cold junction compensation having a resolution of 10 mv/°C. The output was then amplified by a gain of 2 and was fed to the data acquisition board using 8-bit resolution, and then the temperature readings were digitized. Before the start of each melt, the temperature readings of all the thermocouples were checked to see whether they all read the same temperature.

4.1.6. Crucible Inlet and Outlet Water Temperature and Flow Rate

Two chromel/alumel thermocouples were installed in the inlet and outlet water ports on the crucible. Both these thermocouples were connected to a Fluke 52 Digital Thermocouple Thermometer. The instrument has dual thermocouple inputs, one for outlet and the other for inlet water temperature. Hence, it was possible to record the inlet and the outlet water temperatures at the same time during melting. The Fluke 52 has a resolution of 0.1°C. Both the thermocouples were calibrated in the temperature range of interest and had an error of ±0.1°C. Water flow rate to the crucible was measured continuously with a Universal flow meter.

4.1.7. Measurement of Operating Parameters

The melting current was measured with a shunt having a resolution of 1 millivolt per 80 Amps. This output was amplified by 100 using an amplifier. The melting voltage was measured directly from the bus bars on the furnace.

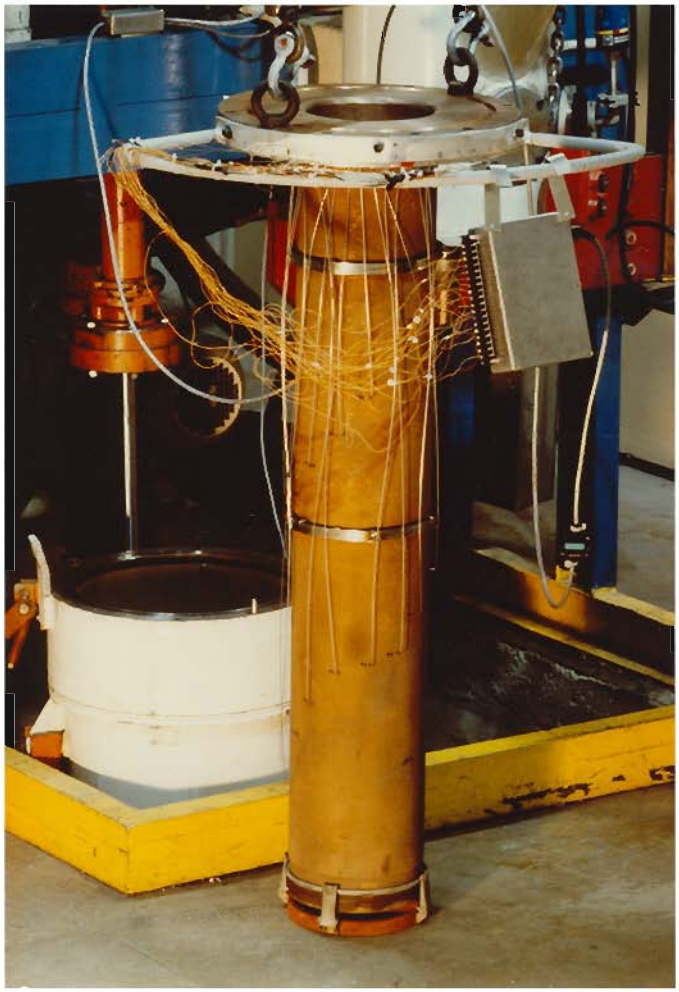

Figure 4.9. Crucible with isolated thermocouples (Second attempt).

For measuring the electrode position, a 10 turn potentiometer was installed on the shaft of the electrode driving motor, and the measured voltage was fed to an analog voltmeter and also digitized.

4.1.8. Monitoring the Melt

The furnace is equipped with a video camera to monitor and record the melt. It was possible to view only three fourths of the top surface of the liquid metal pool as there was only one viewing port. Also, with this system, it was not possible to define the distance between the electrode and the crucible.

4.1.9. Safety Precautions

The three side block walls surrounding the furnace assembly were strengthened with a 3.2 mm thick steel plate with a sand buffer between the wall and the steel plate. All the instrumentation and controls were installed in a room outside the block built of steel plates.

4.2. Design of Experiments

The "One-factor-at-a-time" method in which factors are varied one at a time while the remaining variables are held constant, provides only an estimate of the effect of a single variable at selected fixed levels of the others. This assumes that the effect would be the same at all settings of other variables, or the variables act on the response additively. The factorial analysis on the other hand, can detect and estimate the effect of individual variables and interactions of variables. Factorial designs are a powerful statistical methods for quantifying the effect of a number of variables on a response such as melt rate and metal pool depth. To perform a general factorial design, a fixed number of levels are

selected for each of the variables and experiments are conducted at all possible variable combinations. In the present investigation, three variables were examined at two levels, a 2^3 factorial. This required experiments at 8 different variable combinations. In addition, two experiments were done at the center point of current and electrode gap and two experiments were replicated at the corner points. The variables and the levels are shown in Figure 4.10.

4.3. Materials

For the present investigation, two alloy systems were selected. One was a titanium alloy Ti-6Al-4V and the other was a superalloy Inconel 718. Both of these alloys are considered as the "work horses" in their respective alloy groups, since they are extensively used. The titanium alloy Ti-6Al-4V was supplied by Oregon Metallurgical Corporation, Albany, Oregon, in forged and machined condition in various sizes ranging from 45 mm (1.75") to 114 mm (4.5") in diameter and in various lengths. The forged stock supplied by Oregon Metallurgical Corporation was previously double melted, eliminating any variation in the starting material. The alloy Inconel 718 was supplied by Special Metals Corporation, New York, in the forged and ground condition. The size of these electrodes was about 108 mm (4.25") in diameter and about 915 mm (36") in length. The Inconel 718 electrodes were also previously vacuum induction melted, followed by vacuum arc remelting.

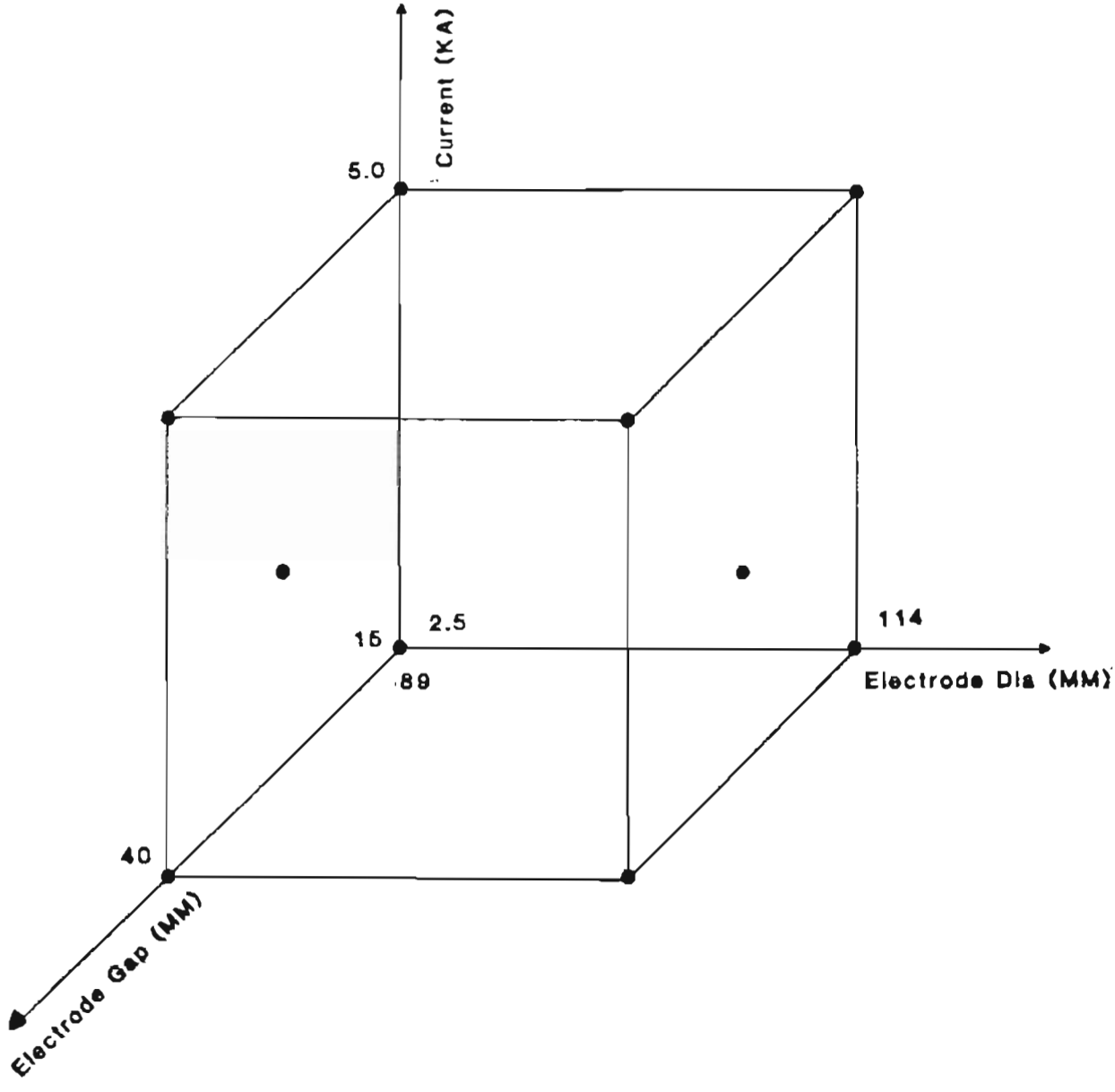

Figure 4.10. Factorial design of experiments.

4.4. Melting Technique

4.4.1. Preparation

In all the experimental melts, a 165 mm (6.5") diameter crucible was used. The forged bar stocks received from Oregon Metallurgical Corporation were cut into 762 mm (30") long electrodes. Starting blocks of 10 mm height were also cut from the bar stock. For adding Ni to reveal the molten metal pool, radial holes were drilled on the electrode at 610 mm (24") from the bottom face of the electrode. A stub made from Ti-6Al-4V was welded to the electrode using Tungsten Inert Gas. The filler wire used was Ti-6Al-4V. The Inconel 718 electrode was welded to a stainless steel stub using TIG. The filler wire in this case was Inconel-625. The electrodes were cleaned with acetone before loading into the furnace. Paint and any scale on the surface of the electrode were removed by grinding. The inside surface of the copper crucible was cleaned with an electrically powered wire brush after each melt. The bottom stool was also cleaned in the same manner, after each melt. A starting block of the same material as that of the electrode was placed on the bottom stool. The crucible was assembled to the bottom stool with the help of four quick disconnect clamps. Then the crucible assembly, along with the bottom stool was put into the water jacket and bolted. The welded electrode was slowly introduced into the crucible till it rested on the starting block and it was then clamped to the stinger rod. The electrode was centered with respect to the crucible at the top and the bottom. The furnace chamber was closed by lifting the crucible with the hydraulic system. At this point the furnace was ready for pumping. The normal pumping sequence consisted of starting the rotary piston pump and after achieving a vacuum level

of 10 mm of Hg, switching on the roots blower pump. It normally took a few hours of pumping to achieve 1u vacuum level in the clean chamber. The leak rate was normally in the range of 1.5 - 3.0 micron/minute.

4.4.2. Melting

Before starting the melt, the electrode was lowered till it touched the starting block placed on the crucible bottom. At this stage, the electrode position was noted, and the electrode was raised 50 mm above the starting block. The water inlet valves for all the cooling system were opened. In order to make sure that the electrode was not touching the crucible, an open circuit test was carried out before the start of each melt. After a satisfactory open circuit test, the electrode was lowered 40 mm leaving a gap of 10 mm between the electrode and the starting block. About 1000 amps of melting current was preselected on the potentiometer, and the melting current and the computer were switched on. By moving the electrode down and then up, an arc was struck between the electrode and the starting block. Usually the arc was struck around 20 volts and was visible on the viewing port. After about 1 minute, the potentiometer was adjusted to achieve the desired melting current. Depending on the current level, either one or both the rectifiers were switched on. Since the operating parameters, viz, melting current, electrode gap and electrode diameter were different for each melt, automatic electrode feed was not utilized in the present experimental work. Electrode feed was controlled manually.

After achieving a sufficient quantity of liquid metal, the electrode gap was measured by driving down the electrode to short circuit and registering the electrode travel in doing so. After a brief short circuit, the electrode was lifted up to

the desired level. This process was repeated a few times during the course of melting, to keep a close control on the electrode gap. The vacuum level during melting was measured from the Pirani gauge and it usually remained constant within a narrow range, for a particular melting conditions.

In all the melts, it was necessary to reveal the molten metal pool profile, hence the electrode was melted till the level of the holes. The approximate electrode position was calculated prior to the start of the melt. Before termination of the melt, it was normal practice to check the electrode through the viewing port. Hot topping was not done and the melt was terminated without decreasing the current slowly. After switching off the melting current, the electrode was raised. After about an hour, the vacuum pumps were switched off and the ingot and crucible were cooled for at least four hours or overnight. In order to break the vacuum, air inlet was was opened. The crucible along with the ingot was taken out from the water jacket. The clamps on the bottom stool were removed and the crucible was slowly lifted, leaving the ingot on the bottom stool. The ingot was then weighed and its surface condition was noted. The height of the crown and the length of the ingot were also measured.

4.4.3. Magnetic Stirring

The furnace is equipped with a magnetic stirring coil. The coil is wound around the inside of the water jacket. This coil can produce a vertical magnetic field, thus causing stirring of the liquid metal pool. The stirring of the liquid metal is used for a variety of reasons. Magnetic stirring is commonly used during the first stage melting of titanium and zirconium alloys, for intensive mixing of the alloying elements. This intentional stirring is used to counteract the stirring

caused due to magnetic field generated by the melting current. Also, the magnetic field causes stabilization of the arc, preventing stray arcs from going to the crucible wall. The magnetic stirring system on the OGC furnace has three modes of operation. Two of these are for the two directions and the third mode is for reversal of the direction. The third mode is a combination of modes one and two, and it has a time setting so that the reversal time can be selected. The magnetic field strength was calibrated with a Gauss-meter at different current settings and the calibration chart is shown in Table 4.2. The maximum field strength used was 45 gauss.

During melting, the magnetic stirring coil was switched on after a sufficient quantity of liquid metal was formed. It was decided to use the medium stirring field strength of 10 gauss in all the experiments, except for the melts which were designed to study the effect of stirring. In order to obtain a desired field strength, a corresponding DC current had to be set up using the calibration chart. Only the third mode of stirring was used in all the experiments and the reversal time was 10 seconds. No stirring was used during Inconel 718 melting.

4.4.4. Helium/Argon Gas Cooling Experiments

The knob on the vacuum regulator was normally in the closed position, except when the gas was needed to be admitted in the gap between the ingot and the crucible. The two valves, one on the crucible and the other, in the control room (in the line between the vacuum regulator and the crucible), were normally open during evacuation of the chamber. When the furnace chamber was evacuated and the vacuum level was in the 1 micron range, the reading on the regulator was 760 mm. The valve on the helium/argon gas cylinder was opened before

TABLE 4.2

CALIBRATION OF MAGNETIC STIRRING COIL FIELD STRENGTH (IN GAUSS)

Current	Switch Position		
Amps	Position 1	Position 2	Position 3
2	9.7	9.0	-
2.5	-	-	10.2 and -10.9
3	13.6	13.0	-
4	17.5	16.9	-
6	25.2	25.8	26.1 and -25.5
8	33.1	34.1	34.2 and -33.5
10	41.5	43	43.0 and -41.8
10.5	44.3	45	45.1 and -43.8

starting the melt. Then, the valve on the cylinder regulator was opened to obtain a delivery pressure of 20 psi, as suggested by the manufacturer of the vacuum regulator. The helium/argon gas was admitted into the gap between the ingot and the crucible after building up about 4 cm of the ingot. The normal technique consisted of slowly turning the knob on the vacuum regulator and reading the indicator gauge. For obtaining 20 mm helium/argon gas pressure in the gap, the knob was turned so as to read 740 mm on the gauge. Once a particular pressure was adjusted, it remained fairly constant through the melting period. The flow rate of the gas was noted from the flow meter. The pressure in the vacuum chamber increased slightly the moment the gas was admitted into the gap, indicating, that some of the gas escaped through the crown of the ingot.

4.5. Evaluation of Ingots

4.5.1. Molten Metal Pool Profile

The technique used in the present investigation was that of doping the molten metal pool with an element/compound that normally segregates. The method adopted in doping consisted of drilling radial holes on the electrode at a predetermined length and filling them with the element/compound and closing the hole by welding (leaving a small hole for evacuation). Several elements were tried for Ti-6Al-4V alloy, ultimately, only the experiments with Ni were successful. For Inconel 718, iron sulfide (FeS) was used. The ingot was sectioned to reveal the molten metal pool profile. First, a transverse cut was made at the top of the ingot near the crown and a second cut near the bottom or middle section of the ingot, depending on the height of the ingot. A longitudinal section was

taken from the central portion of the ingot. The longitudinal section of the ingot was mounted on a specially designed jig, and it was ground on a surface grinding machine. In some cases, the pool profile was seen without etching. 10ml HF + 10ml HNO_3 + 80ml H_2O was used as the etchant to reveal macrostructure and pool profile for the Ti-6Al-4V alloy. Attempts with sulfur prints for Inconel 718 were not successful, as sufficient quantities of sulfur did not enter the molten metal pool. For revealing the molten metal pool profile in Inconel 718 melts, electrolytic etching was used. The electrolytic solution was 15% H_2SO_4 and a current density of 1 Amps/square inch was used.

4.5.2. Chemical Composition

A slice of 25 mm thick was taken just below the bottom of metal pool for chemical analysis. Chemical analysis was done at the edge and center of the ingot. Chemical analysis of titanium alloys was done at Oregon Metallurgical Corporation and that of Inconel 718 at Special Metals Corporation.

4.5.3. Macrostructure

After measuring the depth of the molten metal pool and photographing it, the same longitudinal sections of the ingot were ground again and were used for grain structure and segregation on macro scale. For grain structure analysis, the samples were etched with hydrochloric - peroxide solution containing hydrogen peroxide (30%) - 1 part, hydrochloric acid - 2 parts and water - 3 parts. For segregation analysis (freckles), the samples were etched with a solution containing 5 parts water, 2 parts hydrofluoric acid, 1 part nitric acid and 2 parts sulfuric acid.

4.5.4. Dendrite Arm Spacing and Mushy Zone Size

A slice of 25 mm thick was taken from the ingot just below the final molten metal pool. Specimens were prepared from edge, mid-radius and center of the ingot. The specimens were etched with waterless Kallings reagent. Dendrite arm spacing measurements were made from several photomicrographs taken from various positions in the specimen.

4.5.5. Laves Phase

For revealing the Laves phase, the specimens were electrolytically etched in 120 ml water, 700 ml ethyl alcohol, 100 ml butylene glycol and 78 ml perchloric acid. The Laves phase appears as white etched particles in the interdendritic region.

4.5.5. Scanning Electron Microscope Studies.

The energy dispersive X-ray analyzer on the SEM was used for the analysis of macro-segregation and micro-segregation. The analysis was done on metallographically prepared samples in unetched condition and the spot size was 2.5 square mm. Hence the analysis was the average of several dendrites. The analysis was done at various distances from edge to center of the ingot. The accelerating voltage used was 25 KV. Elemental analysis of dendrite core, interdendritic region and Laves phase was done.

5. RESULTS AND DISCUSSION

5.1. Melt Rate and Molten Metal Pool Depth

5.1.1. Melt Rate Model

In the present investigation, all the melts were made in a 165 mm diameter crucible. The weight of each Ti-6Al-4V alloy ingot was about 35 kgs and the melt time was in the range of 30 minutes at low currents to about 12 minutes at high currents. The weight of each Inconel 718 ingot was about 70 kgs and the melt time was about 35 minutes. Each ingot was weighed accurately after it was cooled. The chemical analysis of a few ingots and electrodes is shown in Table 5.1. There is no significant change in the chemical composition after melting. There is only a decrease in the gas contents after melting.

The average melt rate was calculated from the ingot weight and the melt time, (the melt time is the time at which, the full melting current was applied, till the completion of the melt). Attempts to obtain instantaneous melt rates with a strain gauge type of load cell were not successful as the strain gauge readings had large fluctuations. During melting, the electrode position data was obtained every 32/15 seconds by the data acquisition computer. Hence, it was possible to calculate the instantaneous melt rate from the electrode position data using the expression given below :

TABLE 5.1

CHEMICAL COMPOSITION OF ELECTRODES AND INGOTS IN WEIGHT PERCENTAGE.

Element	Electrode 21	Ingot	Electrode 23	Ingot	Electrode27	Ingot
Carbon	0.028	0.031	0.02	0.019	0.02	0.021
Aluminium	6.52	6.41	6.07	6.14	6.2	6.17
Vanadium	4.18	4.16	4.06	4.17	4.18	4.2
Titanium	Bal.	Bal.	Bal.	Bal.	Bal.	Bal.
Hydrogen	.0014	.0011	.0009	.0008	.0012	.0009
Oxygen	0.46	0.43	0.21	0.182	0.2	0.187
Nitrogen	.03	.026	.013	.008	.018	.01

$$\text{Instantaneous Melt Rate} = \frac{(\text{Wi}\times\text{We})}{(\text{Wi}-\text{We})}\frac{\Delta x}{\Delta t} \tag{5.1}$$

where,

Wi = mass per unit length of the ingot.

We = mass per unit length of the electrode.

Δx = difference in position of electrode in time interval Δt

Δt = time interval

Figure 5.1. shows a plot of instantaneous melt rate as a function of melt time. The average melt rate is also shown in the plot. It can be seen that there is about 6% variation of the instantaneous melt rate about the average melt rate. For large production ingots, it is the instantaneous melt rate which is important as it influences the ingot structure. Also the melting of large ingots takes several hours and requires hot topping, during which time the melt rate is considerably low. Hence, average melt rate is not a good representative of instantaneous melt rate for large ingots. In the present investigation, however, the maximum melting time was about 30 minutes and no hot topping was done. It is thus assumed that the average melt rate is a good representative of instantaneous melt rate. Hence, the average melt rate is used in all further calculations.

The operating parameters used in developing regression model for melt rate are given in Table 5.2. In these experiments, vacuum was treated as a dependent variable. The reason for treating vacuum as a dependent variable was due to the fact that it was not possible to melt Ti-6Al-4V alloy in an argon atmosphere. The arc was unstable during melting under an argon atmosphere, hence, vacuum was treated as a dependent variable. The experimental ranges of the various operating parameters used in developing the regression model for melt

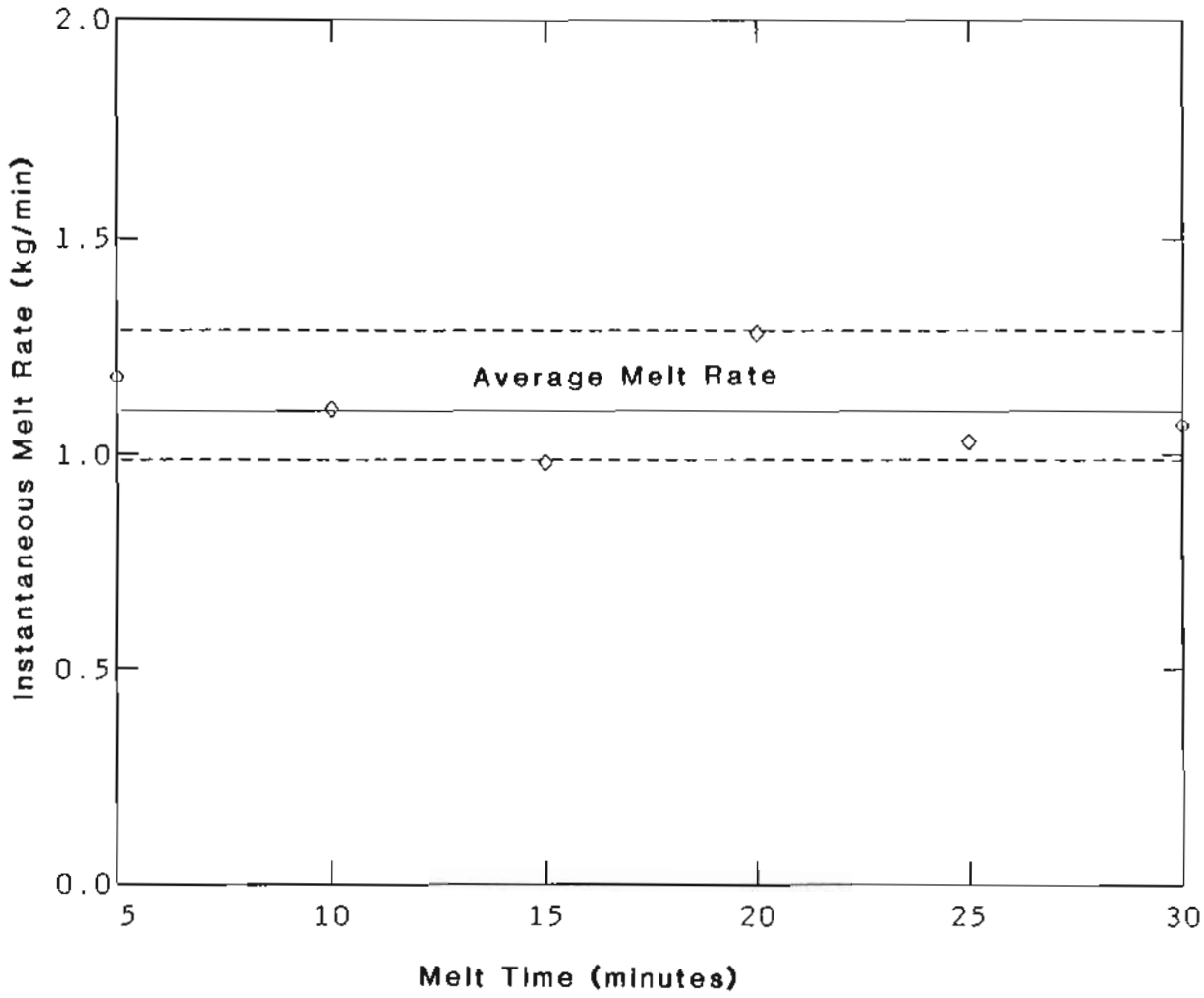

Figure 5.1. Instantaneous melt rate as a function of time.

TABLE 5.2

MELT RATE PARTICULARS - FACTORIAL DESIGN

Melt No.	Power (KW)	Electrode gap (mm)	Vacuum (micron)	Electrode dia (mm)	Melt rate (Kg/hr)
17	66.25	15	70	114	66
18	71.25	40	60	114	54
19	152.5	15	150	114	174
20	160.0	40	100	114	162
21	108.75	22	100	114	120
22	70.0	18	120	89	72
23	75.0	45	60	89	69
24	160.0	18	100	89	162
26	167.5	40	80	89	156
27	120.0	30	70	89	118
39	66.25	15	60	114	61
11	66.25	15	60	114	63

rate are as given below :

Power : 62.5 to 167.5 KW

Current : 2.5 to 5.0 KA

Vacuum Level : 60.0 to 150.0 μ

Electrode Gap : 15.0 to 40.0 mm

Electrode Diameter : 89.0 to 114.0 mm

The data were analyzed using Yates Algorithm (57) and the significant effects were determined. The calculated significant effects are given in Table 5.3. From the estimated effects, it is clear that power is the most important variable. The electrode gap is also found to have an influence on the the melt rate. Two factor interactions, namely, power × electrode diameter and electrode gap × electrode diameter have also been found to influence the melt rate. In all, four regression models were developed for the melt rate using a least square regression technique. The models are discussed in the following sections.

Model I : The model relates Melt Rate to Power, Electrode Gap and Electrode Diameter as given below.

$$\begin{aligned}\text{Melt Rate (kg/hr)} = &- 12.5 + 1.09\,[\text{Power (KW)}] \\ &-0.6\,[\text{Electrode gap (mm)}] \\ &+0.194[\text{Electrode Diameter (mm)}] \qquad (5.2)\end{aligned}$$

The model has a standard error of ± 8.0 based on an overall average melt rate of 115 kg/hr. Student 't' distribution values for the various variables are, for Power, t = 16.9, for Electrode Gap, t = -2.6, for Electrode Diameter, t = 0.92. For six degrees of freedom, values greater than 2.4 indicate a significance greater

TABLE 5.3

ESTIMATED EFFECTS OF 2^3 FACTORIAL EXPERIMENTS.

Interactions	Effect	Estimate
	average	115.3
One-factor	power	98.25
Interactions	electrode gap	-8.25
	electrode dia	0.75
Two-factor	power × electrode gap	0.75
Interactions	electrode dia × power	9.75
	electrode gap × electrode dia	-3.75
Three-factor	power × gap × dia	0.75

than 99.5 % (58). The coefficient of determination was found to be 97%.

Model II : This model relates Melt Rate to Power, Electrode Gap, Electrode Diameter and Vacuum (dependent variable) as given below.

$$\begin{aligned}\text{Melt Rate (kg/hr)} = &- 28.0 + 1.02\,[\text{Power (KW)}] \\ &- 2.80\,[\text{Electrode Gap (mm)}] \\ &+ 0.221\,[\text{Vacuum (micron)}] \\ &+ 0.136\,[\text{Electrode Diameter (mm)}]. \qquad (5.3)\end{aligned}$$

According to this model, the melt rate increases with an increase in pressure. In reality, however, it is the other way, i.e, the pressure increased with the melt rate. This is due to the inadequacy of the vacuum pumps to maintain the low pressure during melting. For example, during melt number 19, the melting current was 5 KA and the melt rate was 174 kg/hr. This higher melt rate resulted in a larger amount of gas being evolved during melting. Hence, the pressure in the melting chamber was 150 micron. The coefficient of determination was 97.8%. Even though this model is statistically significant, it contradicts the observations as discussed.

Model III : Variables considered for this model are Power, Electrode Gap, Power $\times$ Electrode Diameter, Electrode Gap $\times$ Electrode Diameter. The melt rate is related to the above variables as given below.

$$\text{Melt Rate} = 5.94 + 0.26\,[\text{Power (KW)}] + 1.96\,[\text{Electrode Gap (mm)}] + 0.00824\,[\text{Power} \times \text{Electrode Diameter}] - 0.0252\,[\text{Electrode Gap} \times \text{Electrode Diameter}] \quad (5.4)$$

According to this model, the electrode gap has a positive influence on the melt rate. This is again contradictory to actual observations. During melting, the melt rate decreases with increasing electrode gap. But according the model, melt rate increases with the electrode gap which is not in agreement with the observations. Hence, this model also does not agree with the actual observed results, even though it is statistically significant.

Model IV : Variables are Power, Electrode Gap, Electrode Diameter and the three 2-factor interactions, i.e., Power X Electrode Gap, Power X Electrode Diameter and Electrode Diameter X Electrode Gap.

In this case, a stepwise regression technique was used to develop a model for the melt rate. After introducing all the variables, only electrode gap, electrode diameter, power × electrode diameter and electrode gap × electrode diameter finally appeared in the regression equation. Power became insignificant as a main variable, which is unacceptable, since power is the most significant variable.

From the above discussion, it is clear that Model I relating power, electrode gap and electrode diameter to melt rate is the most appropriate model, as it agrees well with the actual physical situation and is statistically significant. Hence, Model I was accepted to be the most realistic model under the present experimental conditions.

The experimental values of the melt rate and power are plotted in Figure 5.2. There is a linear relationship between power and the melt rate, as was expected. The points above the line are for melts with shorter electrode gaps and the points below the line are for melts with the longer electrode gaps.

5.1.2. Predictions Based on Model I

In general, whenever a model is developed based on laboratory scale experiments, a primary issue is the validity of the model in predicting large scale industrial furnace operation and also whether the model is in agreement with the physical situation. Both of the above issues are addressed in the present investigation. Following are a few examples used to illustrate the validity of the model for industrial furnaces:

Example 1: (80)

Ingot diameter = 762 mm

Power = 1092 KW

Electrode gap = 38 mm

Electrode diameter = 660 mm

The predicted melt rate obtained from the regression model is 21.3 kg/min and the observed instantaneous melt rate was 20.9 kg/min.

Example 2: (80)

Ingot diameter = 762 mm

Power = 1192 KW

Electrode gap = 53 mm

Electrode diameter = 660 mm

The predicted melt rate obtained from the regression model is 23 kg/min and the

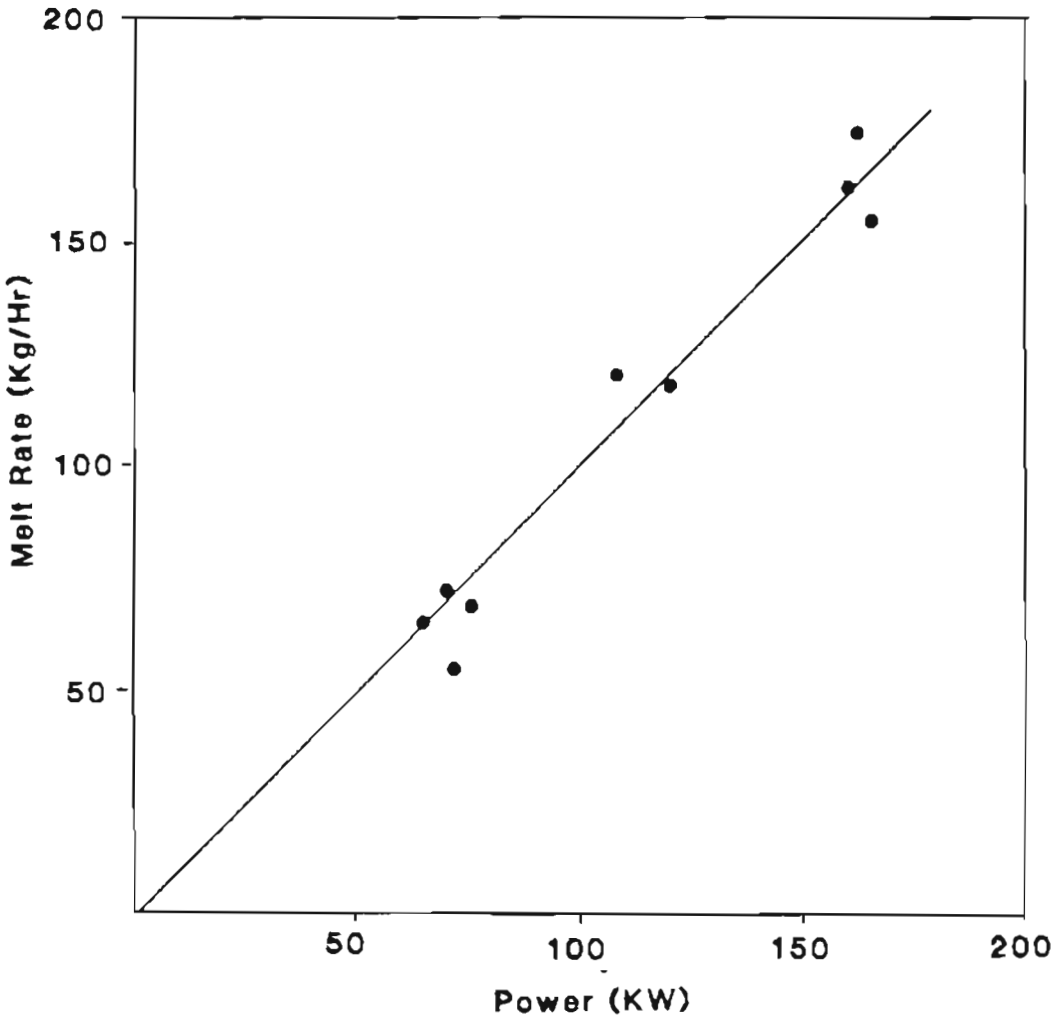

Figure 5.2. Experimental melt rate as a function of power.

observed instantaneous melt rate was 22.7 kg/min.

Example 3: (80)

Ingot diameter = 914 mm

Power = 1092 KW

Electrode gap = 50 mm

Electrode diameter = 812 mm

The predicted melt rate obtained from the regression model is 21.7 kg/min and the observed instantaneous melt rate was 21.8 kg/min.

The predicted melt rate from the model I and the observed melt rate for a industrial VAR furnace are plotted in Figure 5.3. It can be seen that there is a good agreement between the two. Using the present model, melt rates can also be predicted at various electrode gaps and power levels. Recently, a regression model for melt rate as a function of operating variables was developed by Zanner et al (10). The experiments were conducted in a production facility and 500 mm diameter ingots were made. The model developed by them depicts power to be the most statistically significant variable, followed by two factor interactions of power and electrode gap, power and pressure. The model developed in the present investigation is different from that developed by Zanner et al, in many respects. The electrode diameter was used as an independent variable in the present investigation. Zanner et al used pressure as an independent variable. They observed a strong interactions of power with electrode gap, and of power with CO pressure, whereas, in the present investigation, these parameters were not significant.

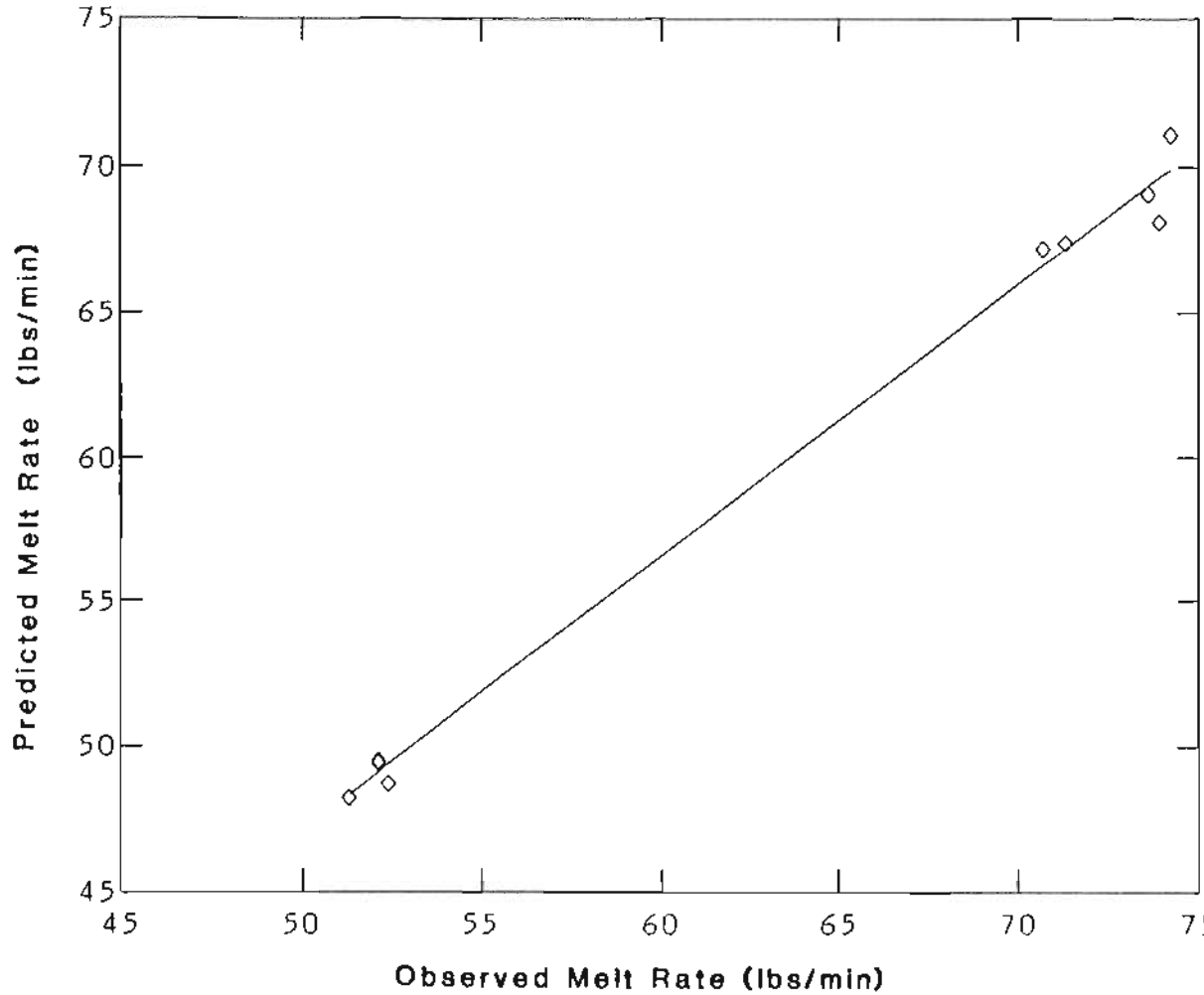

Figure 5.3. Predicted melt rate and observed melt rate.

5.1.3. Specific Energy Consumption and Efficiency

Specific energy consumption is important from the point of view of process economy. Lower specific energy consumption is always preferable. The specific energy consumption was calculated using :

$$\text{Specific Energy Consumption (J/kg)} = \frac{\text{Total energy input}}{\text{Total metal melted}} \tag{5.5}$$

and the efficiency of melting was calculated using :

$$\eta = \frac{\text{Theoretical energy needed for melting}}{\text{Experimental energy input for melting}} \tag{5.6}$$

The theoretical energy required to melt and superheat (by 100°C) 1 kg of the Ti-6Al-4V alloy, from room temperature (25°C), is about 1.75×10^6 Joules (59). Hence,

$$\eta = \frac{(1.75 \times 10^6)}{(\text{Specific Energy Consumption J/kg})} \tag{5.7}$$

The specific energy consumption and efficiency, calculated using the above equations, are given in Table 5.4. It is seen from the table that, for melting conditions with lower currents and longer electrode gaps, the specific energy consumption is higher and the melting efficiency is lower. The melting efficiency is highest, 56% for melting conditions with 5 KA melting current and 15 mm electrode gap. It can also be seen that, vacuum arc remelting is an inefficient melting process where the average melting efficiency is about 50%.

5.1.4. Effect of Melting Current

The effect of melting current on melt rate and specific energy consumption for a 15 mm electrode gap and 114 mm electrode diameter is shown in

TABLE 5.4

SPECIFIC ENERGY CONSUMPTION AND MELTING EFFICIENCY

Melt No.	Current (KA)	Ele. Gap (mm)	Melt Rate (kg/hr)	Sp. Energy (J/kg) 10^6	Melting η (%)
17	2.5	15	66	3.6	48
18	2.5	40	54	4.6	38
19	5.0	15	174	3.1	56
20	5.0	40	162	3.5	50
21	3.75	22	120	3.2	55
22	2.5	18	72	3.5	50
23	2.5	45	69	3.9	45
24	5.0	18	162	3.5	50
26	5.0	40	156	3.9	45
27	3.75	30	118	3.6	48
28	4.0	15	124	3.2	55
29	6.0	15	216	3.1	56
30	2.5	8	69	3.3	53
31	2.5	30	61	4.0	44

Figure 5.4. It is clear that increasing the current results in a proportional increase in the melt rate. Increasing the current also led to a decrease in the specific energy consumption, up to a limit, after which, the specific energy consumption remained the same. The total energy consumed during the process is the sum of the heat required to melt metal and all heat losses. With increasing current, i.e, power level, the losses do not increase proportionately. Hence, the melt rate increases and the proportion of power lost decreases. This results in decrease in the specific energy consumption as seen in figure 5.4. The decrease in energy consumption with the increase in current occurs up to a limit, after which the specific energy consumption remains the same, indicating that there is a maximum current level for each ingot size to maintain the most efficient melting conditions. Soviet investigators have reported (60) that for the vacuum arc remelting of steel, specific energy consumption decreased by about 6.6% when the melt rate increased from 5.4 to 7.15 kg/min. K. O. Yu and H. D. Flanders (34) have made similar observations during the production melting of Inconel 718 in vacuum arc. The melt rate increased and the specific energy consumption decreased with increasing power input. Zanner and Bertram (19) have reported for vacuum arc melting of U-6%Nb, that the specific energy consumption remains the same in the melting current range of 2 - 6 KA.

5.1.5. Effect of Electrode Gap

After power, the second most important parameter is the electrode gap. The electrode gap influences the distribution of heat. In order to understand the effect of electrode gap on specific energy consumption, four melts were made at various electrode gaps ranging from 8 mm to 40 mm. The effect of electrode gap

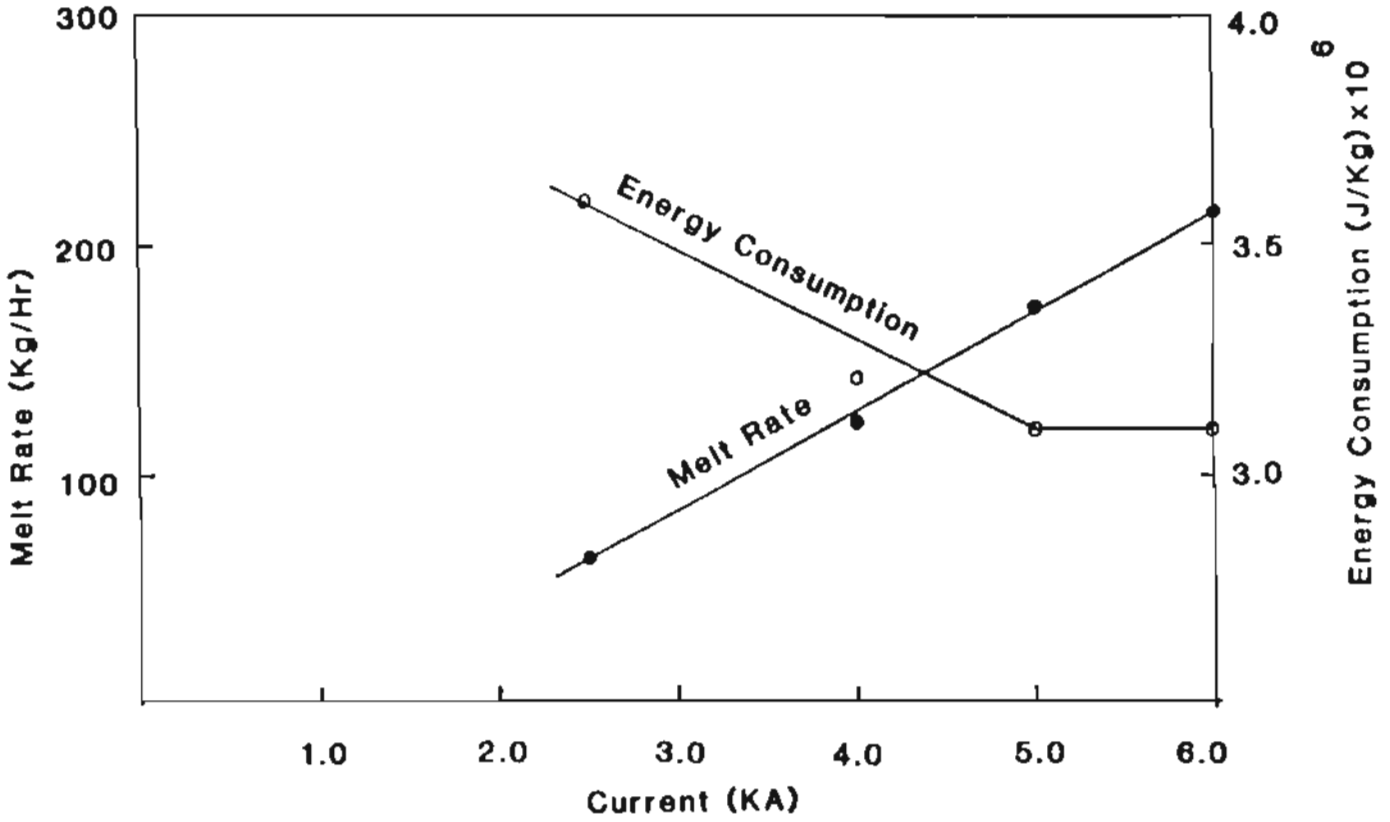

Figure 5.4. Effect of current on melt rate and specific energy consumption.

on melt rate and specific energy consumption is shown in Figure 5.5. Increasing the electrode gap resulted in a decreased melt rate which is in agreement with the melt rate model discussed in the earlier section. At the same time specific energy consumption increased with the increased electrode gap. As the electrode gap increases, the heat loss by radiation increases resulting in increased energy consumption. This is in agreement with the experimental observation at the U. S. Bureau of Mines (7). With higher melting voltage, i.e. longer electrode gap, the heat flux profile on the crucible wall shifted upwards, i.e. more heat was transferred to the crucible above the ingot top. This technique of melting at higher voltages, is normally used during vacuum arc melting of high melting point metals like tungsten.

5.1.6. Efficiency

An expression can be derived for obtaining the melting efficiency under optimum conditions. The regression model I for melt rate, as discussed earlier, is given by :

$$\text{M.R.} = -12.5 + 1.09(\text{Power}) - 0.6(\text{Electrode gap}) + 0.194(\text{Electrode diameter}) \pm 8 \qquad (5.8)$$

Taking an electrode gap of 10 mm as optimum and neglecting the electrode diameter effect, we can write the above expression as,

$$\text{M.R.(optimum)} = -12.5 + 1.09(\text{Power}) - 0.6(10) \pm 8.0$$
$$= -18.5 + 1.09(\text{Power}) \pm 8.0$$

For melting and superheating (100°C) of 1 kg of Ti-6Al-4V alloy, the energy required is 1.75×10^6 Joules. Hence, the energy required for melting Ti-6Al-4V as obtained from optimum melt rate expression is,

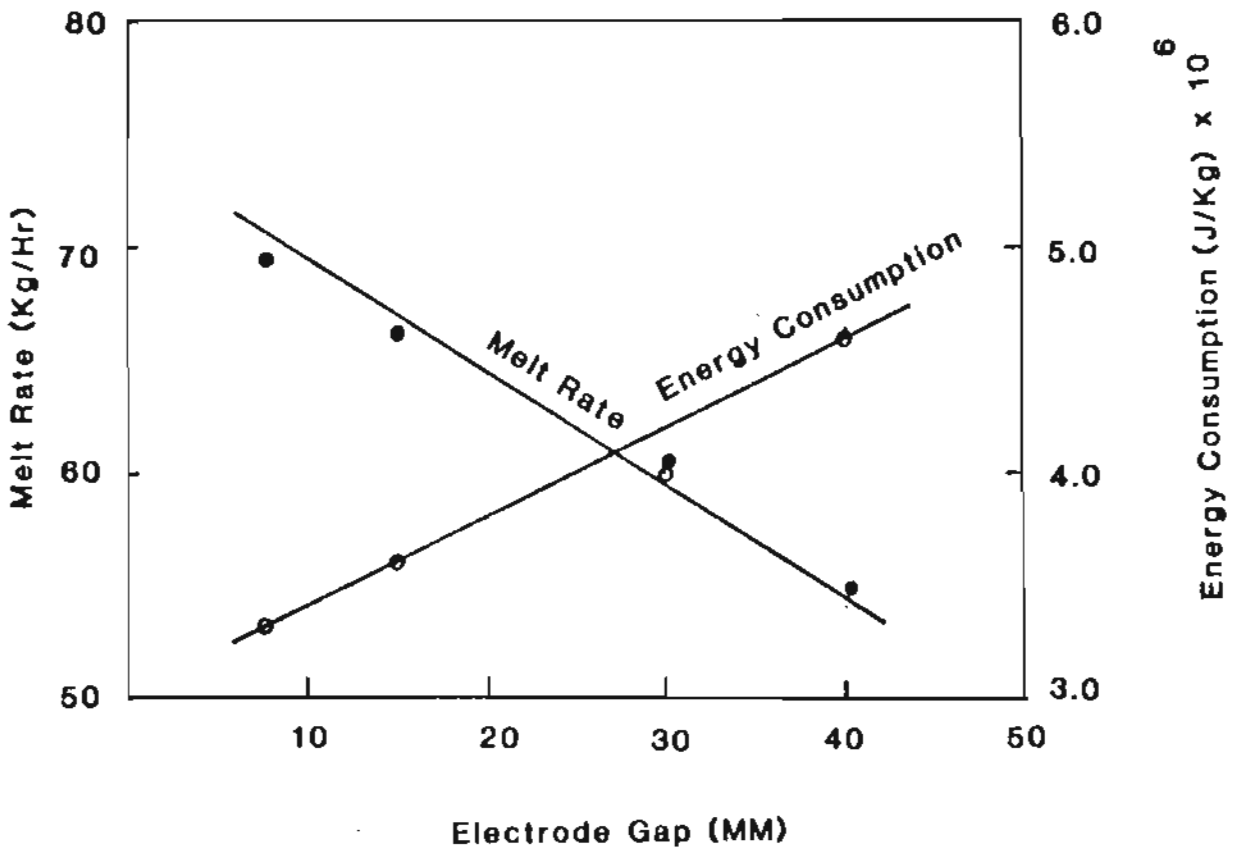

Figure 5.5. Effect of electrode gap on melt rate and specific energy consumption.

$$\text{Energy Required} = \text{M.R.(optimum)} \times 1.75 \times 0.2778$$
$$= [(1.09(\text{Power}) - 18.5) \pm 8.0] \times 0.486$$
$$= 0.53\ (\text{Power}) - 9.0 \pm 3.9$$

Then,

$$\text{Efficiency (optimum)} = \frac{\text{Energy Required}}{\text{Energy input}}$$

i.e.

$$\text{Efficiency (optimum)} = 0.53 - \frac{(9.0 \pm 3.9)}{(\text{power})}$$

Hence, the optimum melting efficiency of VAR process is about 50%.

5.1.7. Effect of Electrode Gap on the Shape of the Electrode Tip

An investigation on the arc behavior and metal transfer mechanism during VAR was carried out at Sandia National Laboratories (14,16,17). It consisted of simultaneous visual observations and arc electrical measurements during melting. In VAR, arc heating of the electrode tip melts a thin film of metal on the tip (about 1 mm) in which metal flows to form hanging protuberances. The formation and evaluation of these protuberances is caused by gravitational forces. Actual metal transfer occurs when the molten metal columns hanging from the cathode tip are separated from the cathode by magnetic forces and subsequently drop in to the molten metal pool in the form of 3 - 10 gms droplets. The metal transfer events make up less than 3% of the total melt time. They have classified (14) the arc in to two types. One is the diffused arc and the other is the concentrated arc. A Diffused arc is observed at short electrode gaps (20 mm or below)

and at low pressures. A concentrated arc is observed at longer electrode gaps (above 20 mm) and higher pressures. Figure 5.6 shows the tip of electrode observed in the present investigation with short electrode gap and long electrode gap. The electrode tips were observed after the sudden interruption of the melting power. With the short electrode gap the electrode tip is almost flat with a small depression in the center. The depression may be due to the metal droplets solidified at about 2/3 radius of the electrode. With long electrode gaps, the electrode tip is conical as shown in Figure 5.6b. In line with the above discussion, with short electrode gap, the arc mode was diffuse and uniform heating of the electrode took place and the efficiency of melting was maximum, about 56%. At long electrode gaps the arc mode was concentrated. Zanner et al reported, that in the concentrated arc mode , the arc is constricted to about 1.5% of the total area intermittantly. This results in a non uniform heating of the electrode. The melting efficiency under this condition was only 38% as shown in Table 5.4. Hence, optimum melting conditions are short electrode gaps and higher currents.

5.1.8. Surface Quality of the Ingot

The surface quality of the ingot is important, in that it influences the economy of the process. An ingot with a rough surface needs surface conditioning treatment before further processing. Figure 5.7. shows the photographs of the ingot surfaces obtained for cases with long electrode gap and short electrode gap. The ingot surface was smoothest with high current (5 KA) and short electrode gaps (15 mm) and the ingot surface was rough with long electrode gap (40 mm) and low current (2.5 KA).

a) With short electrode gap.

b) With long electrode gap.

Figure 5.6. Typical tips of electrode.

a) 5.0 KA Melting current and 15 mm gap.

b) 2.5 KA Melting current and 40 mm gap.

Figure 5.7. Ingot surface under various melting conditions.

As the electrode gap increased, the crown height also increased. With the long electrode gap, as discussed in the previous section, the arc is concentrated and most of the arc heat is closer to the center of the electrode. This possibly results in an increased crown height. At 40 mm electrode gap and 2.5 KA melting current, the crown height was 7". In case of melting with higher current, longer electrode gap, splatter was probably partially remelted, resulting in a slightly rough surface. However, as the electrode gap increased and with lower current, the splatter was not remelted resulting a rougher surface, as shown in Figure 5.7b.

In the present investigation, an attempt was made to develop a surface finish factor index to indicate the surface roughness of the ingot. A surface finish factor index varied from 1, for a rough surface to 8 for a smooth surface, as shown in Table 5.5. The numbers in the surface finish factor index were obtained from the experimentally measured crown height.

$$\text{Surface Finish Factor} = \frac{10}{(\text{Crown height in inches})}$$

It is clear from the table and the above defined relation that, as the crown height increases, the surface finish factor decreases and the surface of the ingot tends to be rougher. With the longer electrode gap, more splatter was deposited on the crucible wall leading to rough surface of the ingot. This situation was observed experimentally also. In the present investigation, only the effect of current and electrode gap on the surface finish factor were studied.

5.1.9. Effect of Melting Parameters on the Molten Pool

TABLE 5.5

SURFACE FINISH FACTOR

Melt No.	Crown Height (inches)	Surface Finish Factor	Remarks
17	1-1/2	6	
18	7	1	Rough Surface
19	1-1/4	8	Smooth surface
20	2-1/2	4	
21	1-1/2	6	
22	1-3/4	5	
23	4-1/4	2	
24	1-3/4	5	
26	2-3/4	3	
27	2-1/2	4	

The major discussion so far has been in determining the factors effecting melt rate. This section is concerned with studying the effects of melt rate on the metal pool depth. A deeper metal pool results in a deeper mushy zone leading to increased segregation. Hence, in the present investigation the factors influencing the metal pool depth were studied. The most important aspect in measuring the depth of the molten metal pool is that the measurement should be made when the pool achieves a quasi-steady state. In the present investigation, one melt was made to determine at what height of the ingot, the molten metal pool achieves a quasi-steady state. Radial holes were drilled on the electrode at predetermined electrode length corresponding to various heights of the ingot, and the holes were filled with Ni to reveal the pool profile. Experiments were carried out to reveal the molten metal pool with various elements like W and Cr. Only the experiments with Ni were successful as Ni widens the liquidus and solidus.

A photograph of the molten metal pool profile at different heights of the ingot is shown in Figure 5.8. The measured depth of the molten metal pool is shown in Figure 5.9. At an ingot height equal to the diameter of the ingot, the molten metal pool bottom part was almost flat indicating that the extraction of heat from the bottom stool was still significant at this level and after about two times the ingot diameter, the pool depth remains the same.

Paton et al (61) have carried out an investigation on the electroslag remelting process for quasi-steady state. They have modeled the variation in the centerline pool depth as a function of the ingot height. In the present investigation, an attempt was made to use the dimensionless relationship for pool depth given by Paton. In order to use the dimensionless relationship, two dimensionless

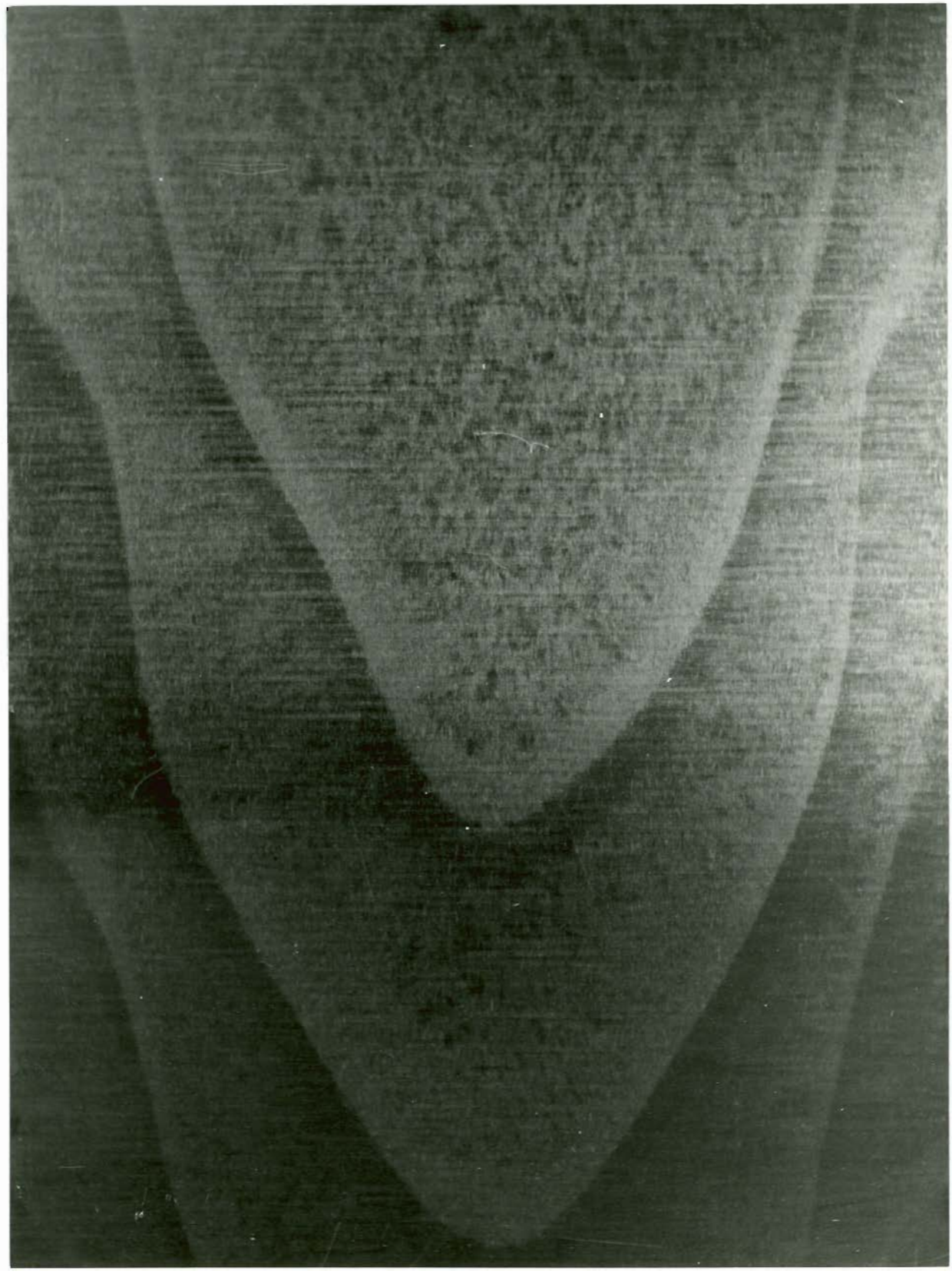

Figure 5.8. Molten metal pool profile at different ingot heights. (Scale 1:1)

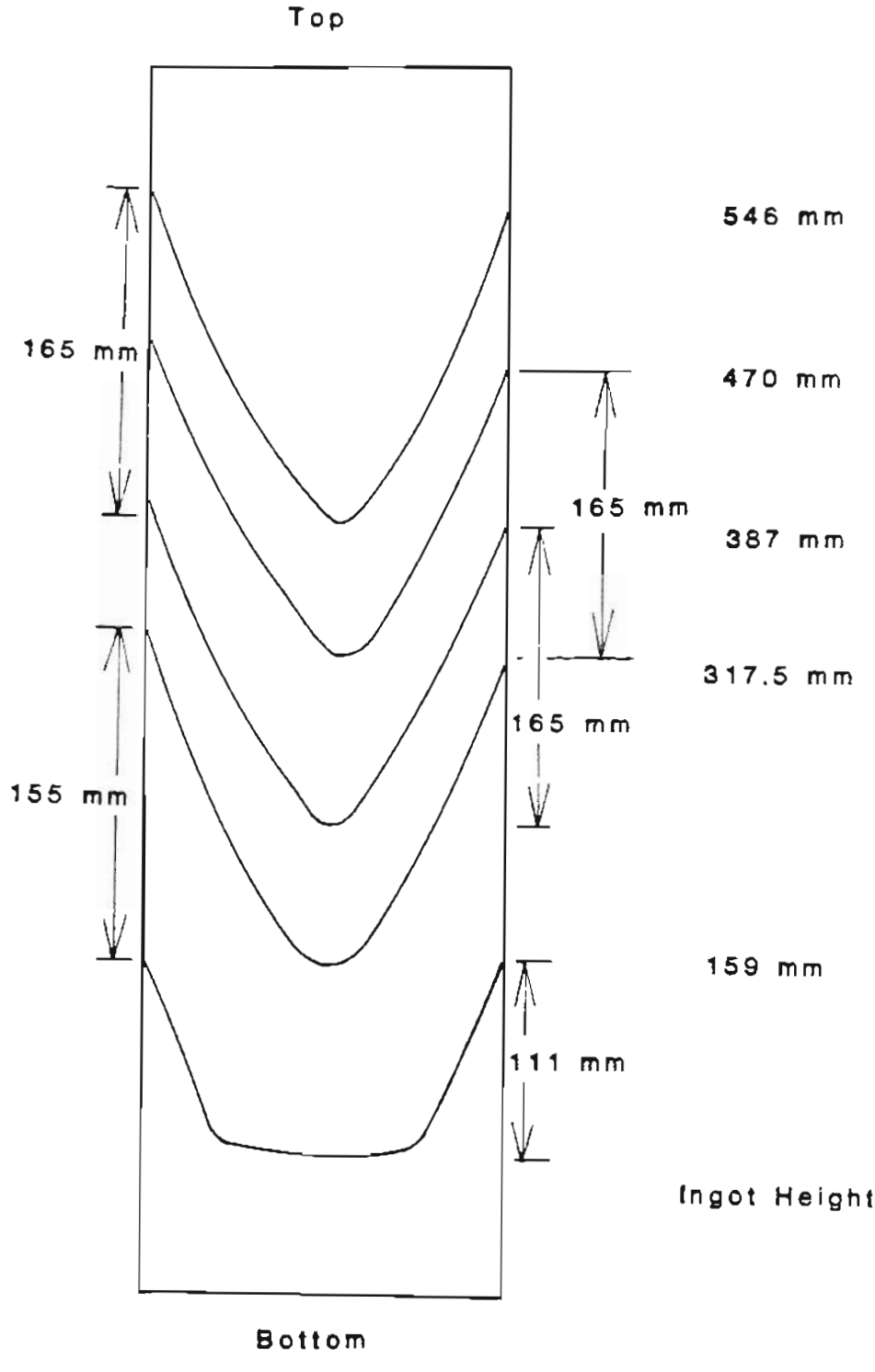

Figure 5.9. Measured molten metal pool depth at different ingot heights.

numbers i.e., Peclet number and Fourier number need to be evaluated. The Peclet number is give by,

$$Pe = \frac{VR}{\alpha} \tag{5.9}$$

and the Fourier number is given by,

$$Fo = \frac{\alpha \times t}{R^2} \tag{5.10}$$

Where,

V = rate of ingot build up in cm

α = thermal diffusivity = $\frac{k}{\rho \times c_p}$

k = thermal conductivity of Ti-6Al-4V = 0.04175 cal/cm-sec C

c_p = specific heat for Ti-6Al-4V = 0.22 cal/gm C

ρ = density of Ti-6Al-4V = 4.42 gm/cm^3

R = radius of the ingot in cm

t = time in seconds

The Peclet number for Ti-6Al-4V was found to be 5.1. A plot of the dimensionless pool depth versus the Fourier number for this work is superimposed upon a similar plot given by Paton is shown in Figure 5.10. According to the plot, lower the Peclet number, the molten metal pool reaches steady state faster. The plot of the present investigation should lie above the curve 1 as the Peclet number is 5.1. The plot indicates some discrepancy between the present calculations and those of Paton. A similar discrepancy was reported by Ballantyne(48). Ballantyne's pool depth data were computer simulated for 1100 mm diameter ESR ingot. They attributed the discrepancy to the thermophysical properties of

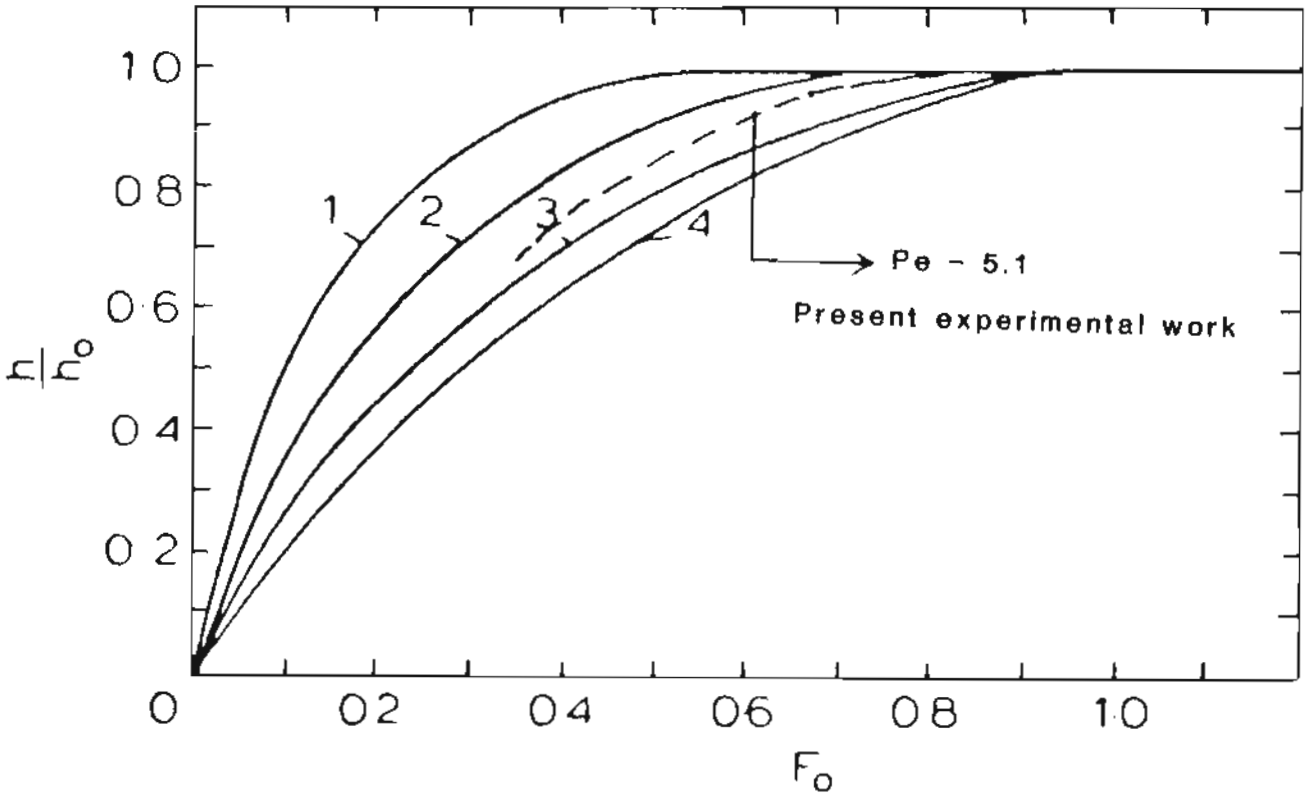

1 *Pe* = 5·8 ; 2 *Pe* = 7·9 ; 3 *Pe* = 11·9 ; 4 *Pe* = 13·7 (experimental)

Figure 5.10. Dimensionless molten metal pool depth as a function of melt time.

the material. According to Ballantyne (48), the metal pool during ESR, as predicted by computer simulation, achieved quasi-steady state once the ingot length was equal to one to two diameters. The values obtained in the present investigation are experimental and are for the VAR system. However, the basic characteristics of the VAR are the same as those of the ESR. In the present investigation, the molten metal pool depth achieved a quasi-steady state after the ingot length reached twice the ingot diameter.

The molten metal pool profile was revealed for all the melts of the factorial design experiments. Figures 5.11 and 5.12. show the molten metal pool profile at low and high currents respectively. At low melting currents, the metal pool profile is like a cup as in Figure 5.11. At high currents, the pool profile is conical and deeper.

Regression Model for Pool Depth :

Regression Models developed for melt rate as a function of operating variables have been discussed in earlier sections. A model for molten metal pool depth as a function of melt rate was developed and is given below :

$$\text{Pool Depth (mm)} = 21.3 + 1.09\ |\text{Melt Rate (kg/hr)}| \pm 12.9 \quad (5.11)$$

The model has a standard error of $\pm$ 12.9. The coefficient of determination is 98%. The student 't' distribution value is 13.9. For seven degrees of freedom values greater than 2.36 indicate a significance greater than 99.5%. A plot of the molten metal pool depth versus the melt rate is shown in Figure 5.13. There is a linear relationship between the molten metal pool depth and the melt rate. It was not possible to check the validity of the model for pool depth as the pool

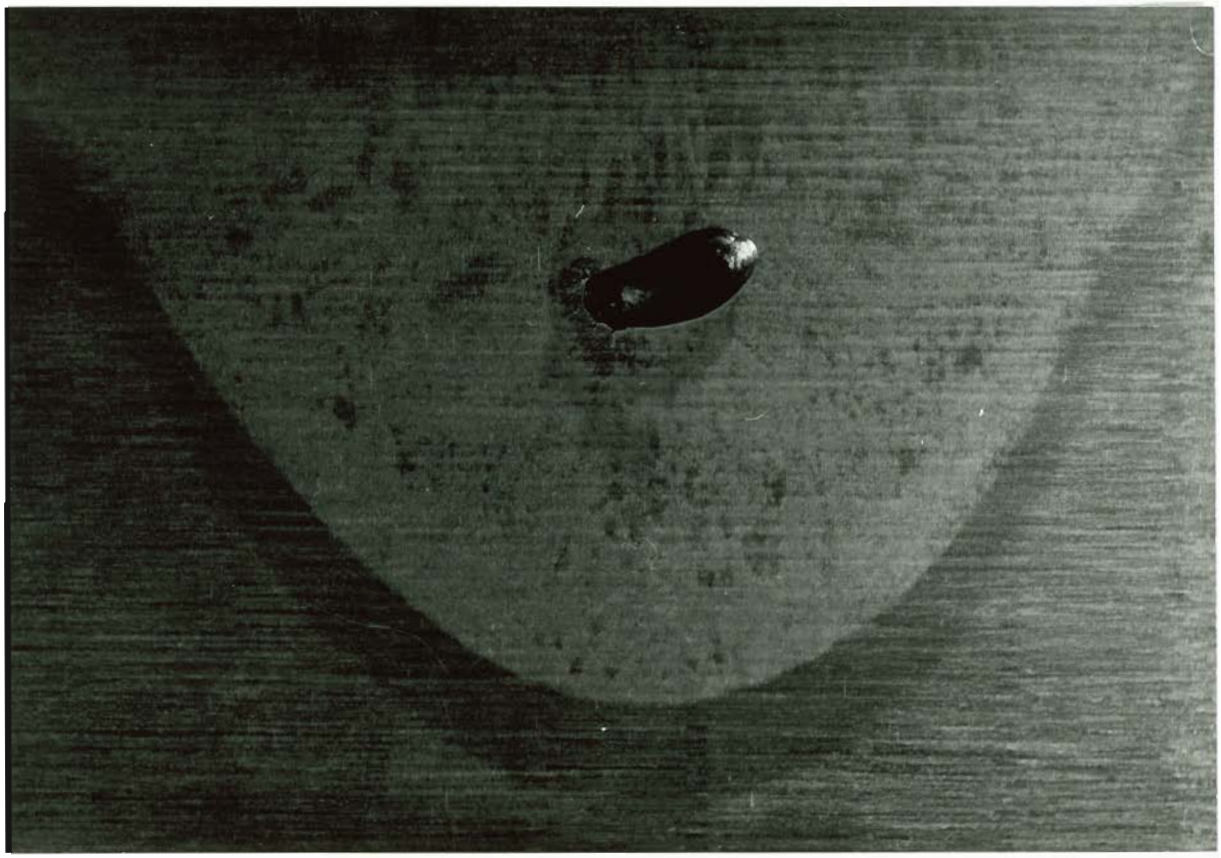

Figure 5.11. Molten metal pool profile at low melting current. (Scale 1:1)

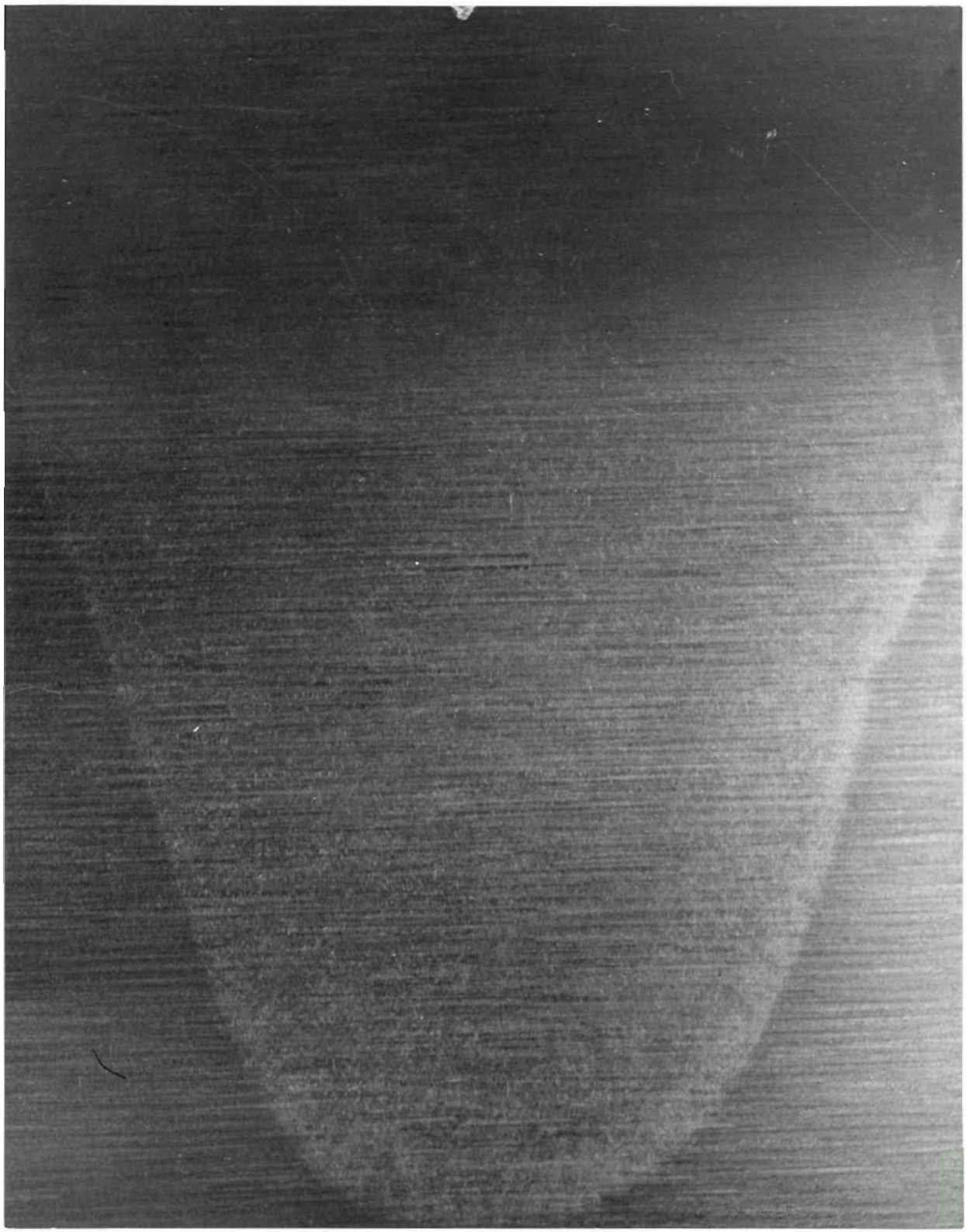

Figure 5.12. Molten metal pool profile at high melting current. (Scale 1:1)

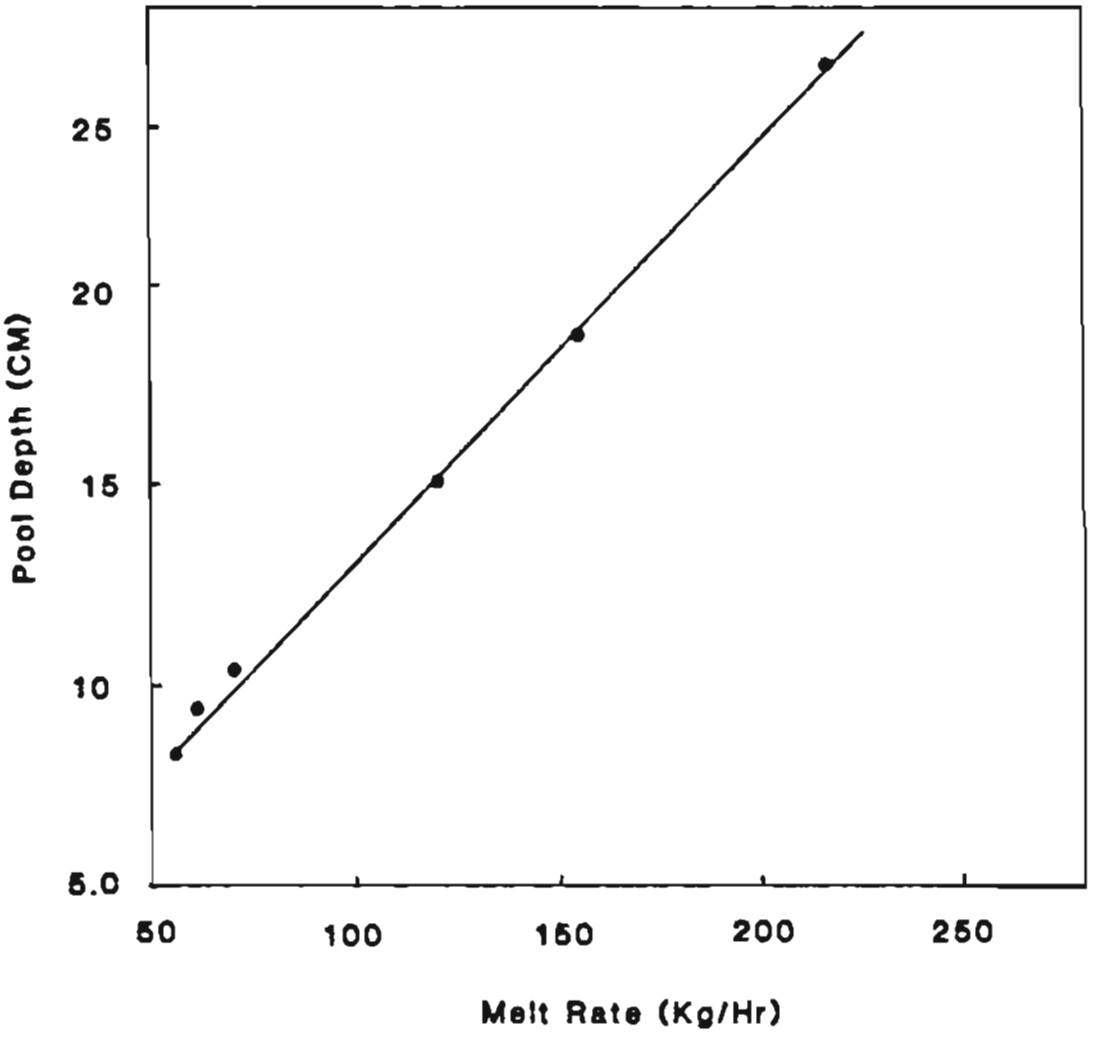

Figure 5.13. Molten metal pool depth as a function of melt rate.

depth values for industrial ingots were not available.

5.1.10. Effect of Magnetic Stirring

Six melts were carried out to understand the effect of magnetic stirring on the melt rate, molten metal pool depth and surface quality of the ingot. Three melts were made with 2500 Amps and the other three were made with 4000 Amps. The magnetic stirring conditions that were used, were, zero field strength, 10 gauss and 45 gauss (maximum field strength that is possible in the system). Table 5.6 gives the experimental details of these melts and the corresponding melt rates. It can be seen that the melt rate decreased with stirring, and, the higher the strength of the magnetic field, the greater the decrease in the melt rate. A similar phenomena was observed at higher melting currents. This could be due to the fact that the applied magnetic field leads to a deconcentration of the arc, thus leading to a change in the heat distribution between the electrode and the ingot. With deconcentration of the arc, more energy is transferred to the annular region between the electrode and the ingot and less energy is available just below the electrode area as compared to no stirring conditions. Hence, this could lead to a decrease in the melt rate with stirring. A similar behavior was observed in an investigation (62) carried out to study the effect of magnetic stirring during vacuum arc melting of steel.

The effect of magnetic stirring was even more significant on the molten metal pool depth as compared to the melt rate. The effect of magnetic stirring on molten metal pool depth at a melting current of 2500 Amps is shown in Figure 5.14 to 5.16. A deep molten metal pool was obtained when no stirring was used, and as the stirring increased, the pool became shallower. The explanation

TABLE 5.6

EFFECT OF MAGNETIC STIRRING

Melt No.	Current (KA)	Magnetic Field (Gauss)	Melt Rate (kg/min)	Ingot Surface
34	2.5	0	1.17	Poor
17	2.5	10	1.1	Good
35	2.5	45	0.98	Poor
37	4.0	0	2.11	Good
28	4.0	10	2.06	Good
38	4.0	45	1.91	Good

Figure 5.14. Molten metal pool depth with no magnetic stirring (melting current 2.5 KA).

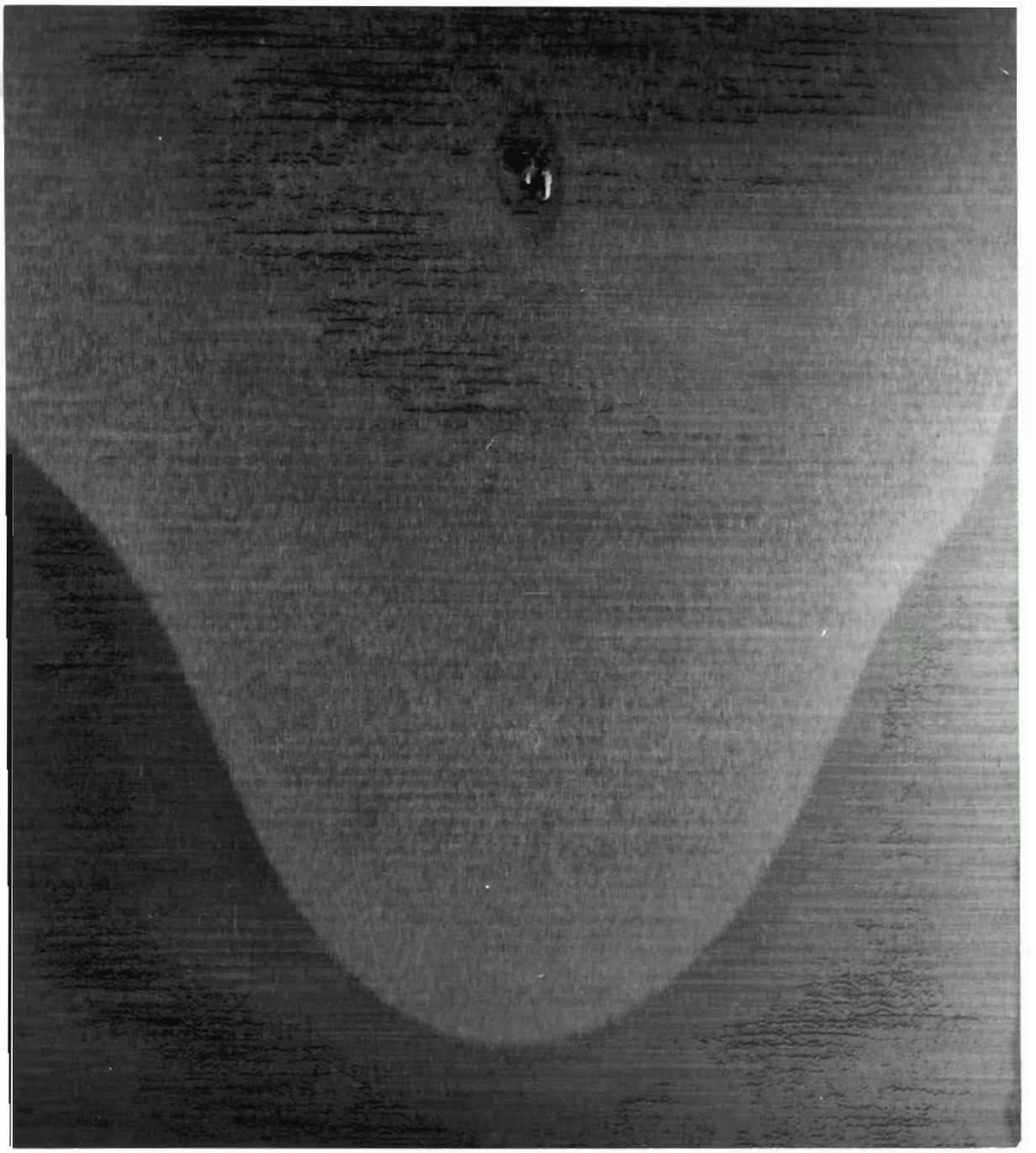

Figure 5.15. Molten metal pool depth with 45 gauss magnetic stirring (melting current 2.5 KA).

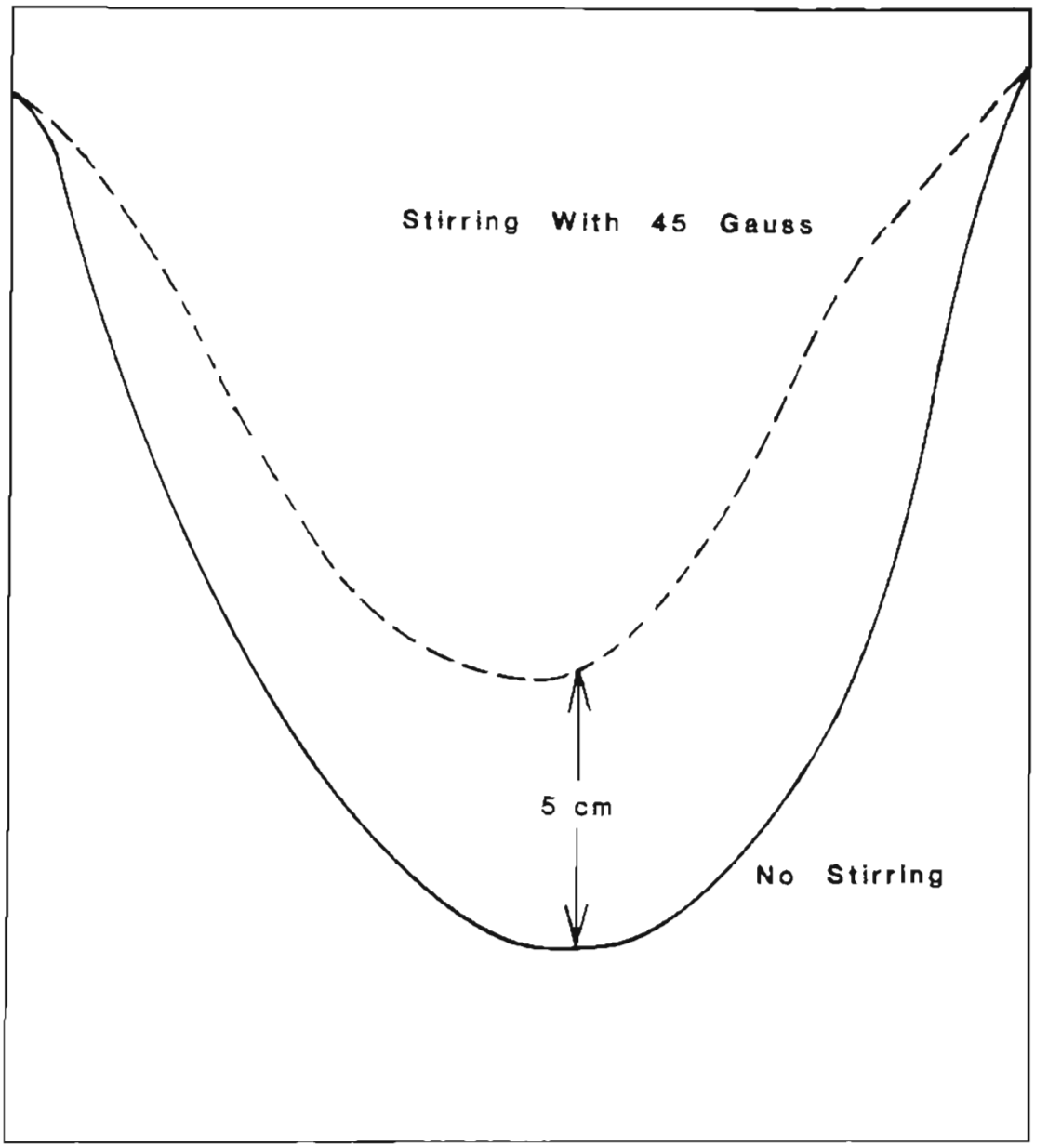

Figure 5.16. Effect of magnetic stirring on molten metal pool depth (melting current 2.5 KA).

for a deep pool with no stirring may be due to a combination of two effects. The first factor may be due to concentrating the arc in the central position below the electrode, leading to a deep pool. The second factor may be associated with the severe splatter deposition on the crucible wall, that results in a rough porous surface on the ingot, which, reduces the heat transfer from the ingot. This results in a deep pool. The effect of second factor was also confirmed by the surface quality of the ingot. The surface of the ingot was rough and porous with no stirring. With moderate stirring, that is with a 10 Gauss field, the surface quality of the ingot was the best. When 45 Gauss stirring was used, the surface of the ingot deteriorated, but, in this case, it was better than the one obtained without stirring.

With magnetic stirring, a more uniform distribution of heat takes place on the pool surface and also, stirring washes the crucible wall and establishes a better contact between the ingot and the crucible thus enhancing the heat extraction. The effect of magnetic stirring on the molten metal pool depth at higher melting current, viz, 4000 Amps, is shown in Figure 5.17. It can be seen that, the pool depth decreased with magnetic stirring. However, the decrease in pool depth was not as significant as it was in the case of low melting current. The pool depth decreased by almost 30% with 45 Gauss stirring at 2500 Amps melting current as against a decrease of 17% with the same stirring field strength at 4000 Amps of melting current. So, the magnetic stirring has less effect on the molten metal pool depth at higher melting current. This could be explained in terms of the applied magnetic stirring and the stirring created by the natural field which is due to the melting current. The applied and natural fields may be

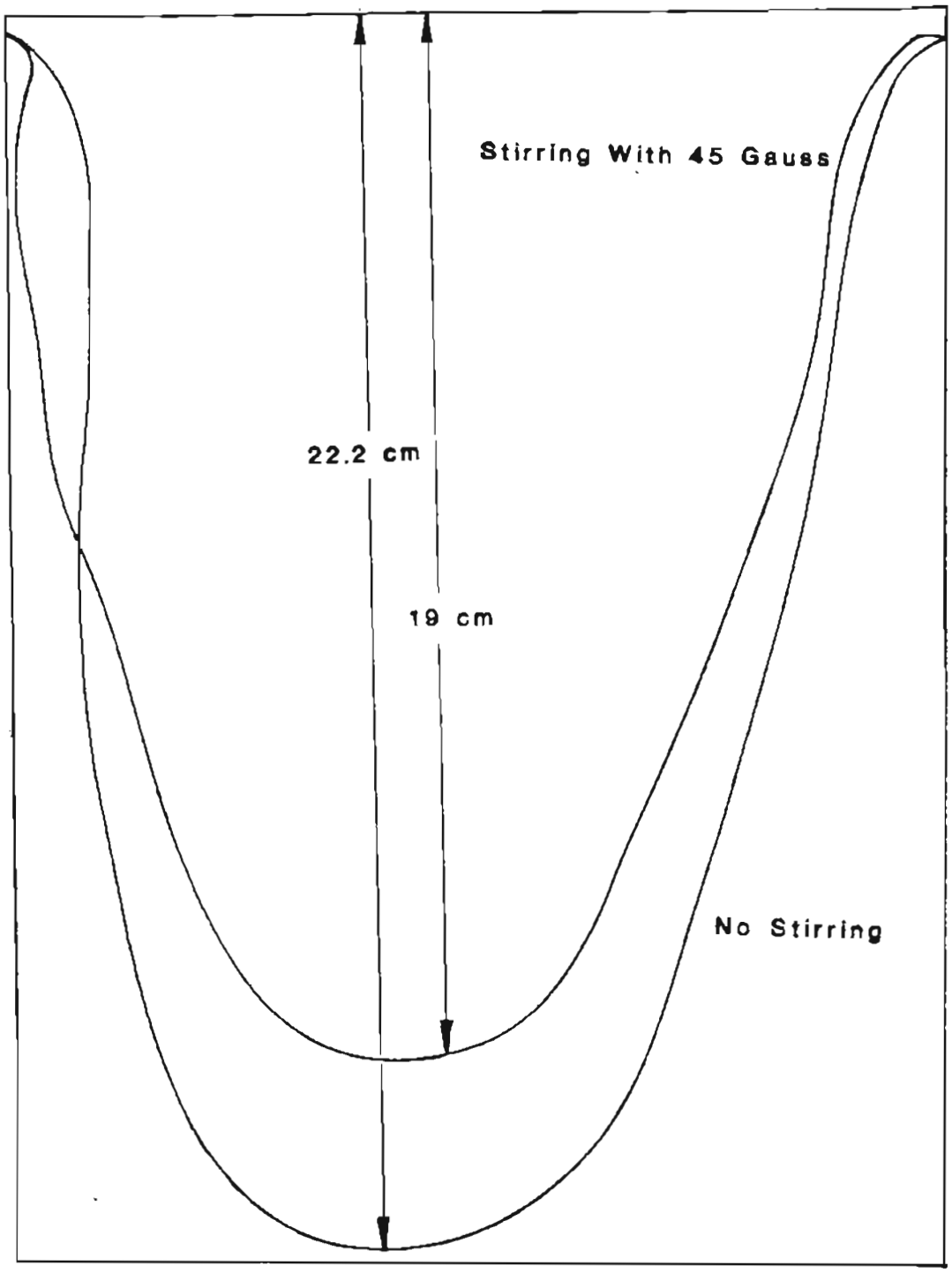

Figure 5.17. Effect of magnetic stirring on molten metal pool depth (melting current 4.0 KA).

interacting. The strength of the natural magnetic field increases with the current, and this field may be counteracting the applied magnetic field, hence, decreasing the effectiveness of the applied magnetic field at higher melting current.

5.1.11. Regression Model For Voltage

During the experimental investigation, it was found that the voltage is sensitive to current, electrode diameter and electrode gap. Hence, it was decided to develop a model for voltage as a function of the current, electrode diameter and the electrode gap. Table 5.7 shows the particulars of the dependent and independent variables. The regression model for voltage, developed using the data, is as given,

$$\begin{aligned} \text{Voltage (V)} = \; & 28.7 + 1.54\,|\text{Current (KA)}| \\ & + 0.0704\,[\text{Electrode gap (mm)}] \\ & - 0.0613\,[(\text{Electrode diameter (mm)}] \pm 0.4 \end{aligned}$$

The coefficient of determination is 97.4 %. The student 't' distribution value for current is 12.50, for the electrode gap t = 5.76 and for the electrode diameter, t = -5.51. For six degrees of freedom, values greater than 2.4 indicate a significance greater than 99.5 %. It can be seen that, current is the most significant factor and not the electrode gap. The above model is useful in predicting the voltage to maintain a particular electrode gap.

TABLE 5.7

PARTICULARS OF VOLTAGE MODEL

Melt No.	Current (KA)	Electrode Gap (mm)	Electrode Dia. (mm)	Voltage (volts)
17	2.5	15	114	26.5
18	2.5	40	114	28.5
19	5.0	15	114	30.5
20	5.0	40	114	32.0
21	3.75	22	114	29.0
22	2.5	18	89	28.0
23	2.5	45	89	30.0
24	5.0	18	89	30.0
26	5.0	40	89	33.5
27	3.75	30	89	32.0

5.2. HEAT TRANSFER WITH GAS COOLING

5.2.1 Theoretical Heat Transfer

5.2.1.1. General Background

The melt rate of the electrode and the cooling conditions of the ingot are the two most important factors influencing the ingot structure and the severity of segregation in VAR ingots. The operating parameters affecting the melt rate and its effect on molten pool depth, economy of the process and surface quality of the ingot have been evaluated and discussed in the previous sections. In this section, we will evaluate theoretically and experimentally the other factor viz. the cooling condition of the ingot.

Figure 5.18. shows a schematic of VAR process. The shrinkage gap between the ingot and crucible is also shown in the figure. In VAR there are three zones of heat transfer. The zone above the ingot top, the zone of contact with the crucible and the zone below the molten metal pool where the shrinkage is formed. The zone above the ingot top has little effect on the heat transfer in VAR. The important zone is the shrinkage gap region. In this zone, heat from the ingot surface is transferred to the cooling water by a sequence of steps in series. As shown in Figure 5.19, there are three sequences : (1) radiation across the gap separating the crucible and the ingot; (2) conduction through the crucible wall itself; (3) convection at the crucible/cooling water interface.

One can write the overall heat transfer coefficient from the ingot to the cooling water (neglecting the resistance due to scale deposit on the crucible) as,

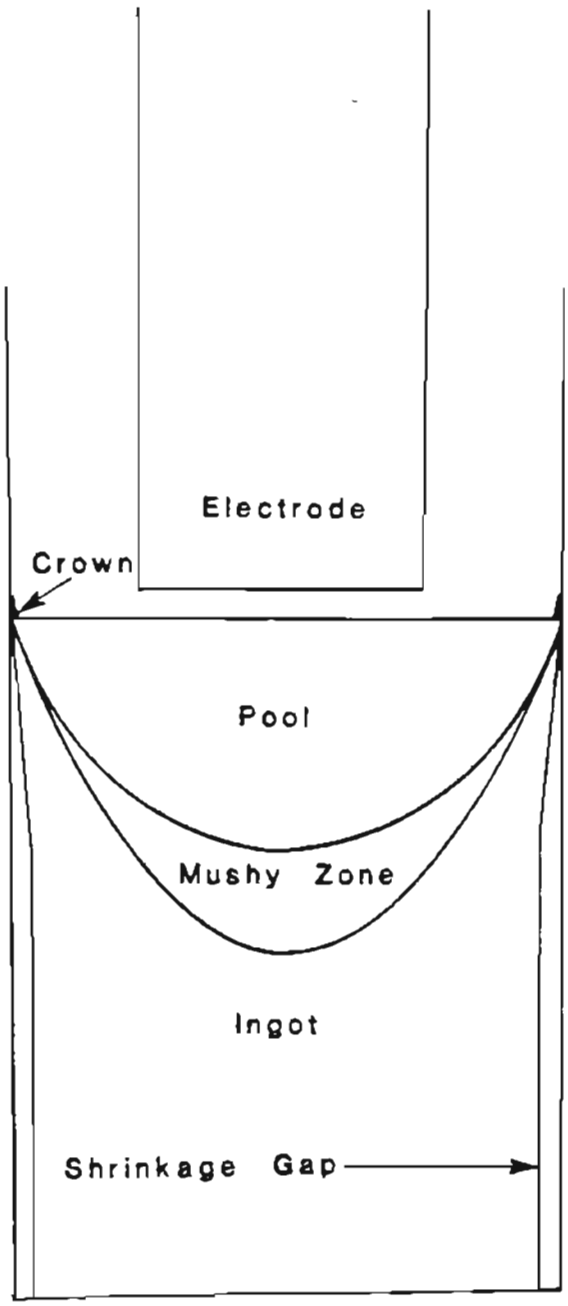

Figure 5.18. Schematics of VAR showing the shrinkage gap between the ingot and crucible.

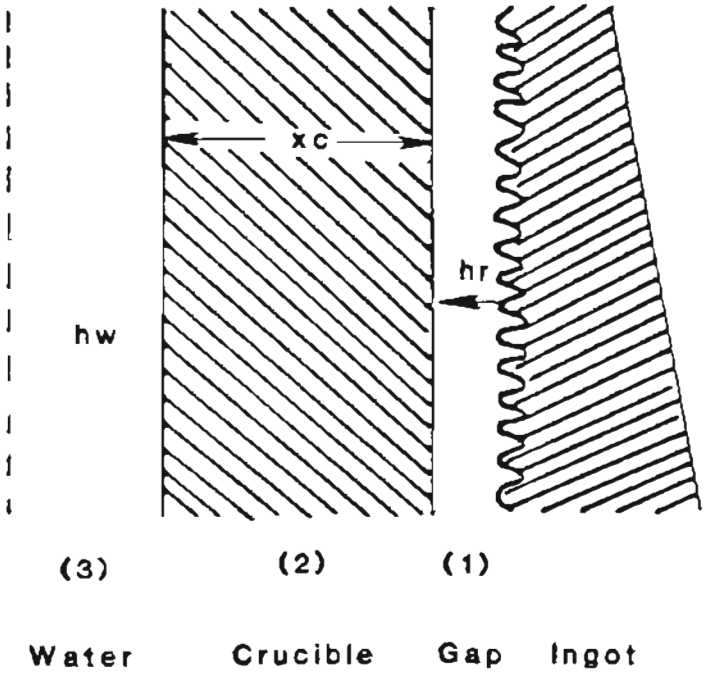

Figure 5.19. Mechanism of heat transfer in the gap region.

$$h_{ov} = \frac{1}{\frac{1}{h_r} + \frac{\Delta x_c}{k_c} + \frac{1}{h_w}} \tag{5.12}$$

where,

h_{ov} = overall heat transfer coefficient.

h_r = radiation heat transfer coefficient.

Δx_c = thickness of the crucible.

k_c = thermal conductivity of the crucible material.

h_w = heat transfer coefficient due to water cooling at the crucible/water interface.

For a typical continuous casting machine, the importance of each of the above resistances to heat flow has been calculated (11). The resistance due to the air gap is about 84 % of the total, the resistance due to crucible conduction is about 2 % and the resistance at the crucible/cooling water interface is 14 %. The mechanism of heat transfer in VAR is similar to that of a continuous casting machine, except for the presence of vacuum instead of air gap. The relative importance of each of these resistances in VAR is discussed below.

Taking an inside crucible wall temperature of about 200°C(15) , one can plot the typical temperature gradients in the VAR process as shown in Figure 5.20. It can be seen that at the ingot/crucible interface, the temperature drop is about 1000°C. This temperature drop exceeds that in the crucible wall by a factor of 20. It has been reported (60), that by increasing the water flow rate from 0.025 to 1.5 m/sec, the heat removal rate was increased by only about 5 %. This indicates that the main thermal resistance for heat extraction from the ingot to the

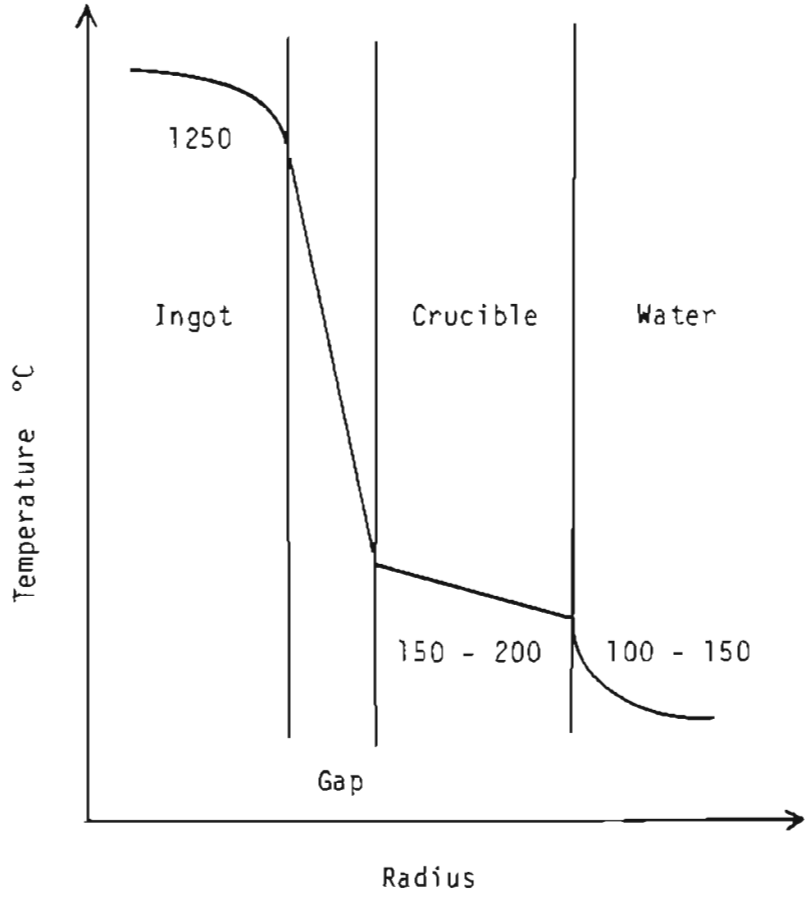

Figure 5.20. Typical temperature gradients in the VAR process.

cooling water is the ingot/crucible interface. The rate controlling factor in the overall heat transfer rate in VAR is, therefore, the ingot/crucible interface.

Hence, it is necessary to examine the ingot/crucible interface carefully. Since the melting is done under vacuum, the heat transfer at the ingot/crucible interface is only by radiation (assuming heat transfer by solid conduction is negligible). If a gas of good thermal conductivity is introduced into the gap between the ingot and the crucible, then the heat extraction rate could be increased, as the heat transfer is now due to both gas conduction and radiation. Thus the total heat flux at the ingot/crucible interface is given by,

$$q_{total} = \dot{q}_r + \dot{q}_{gas} \tag{5.13}$$

where,

$\dot{q}_r$ = heat flux due to radiation

$\dot{q}_{gas}$ = heat flux due to gas conduction

The technique of introducing a gas in the gap between the ingot and the crucible was patented by J. M. Wentzell (12) and was assigned to Special Metals Corporation of New York. Even though this technique is being used by superalloy manufacturers, no systematic investigation has been reported that quantifies the effect of gas cooling on heat extraction rate, molten metal pool depth, mushy zone size and segregation.

5.2.1.2. Thermal Conductivity of Gasses

Effect of Pressure.

The thermal conductivity of various gasses is shown in Figure 5.21. Hydrogen has the highest thermal conductivity of all the gasses. Its use is, however,

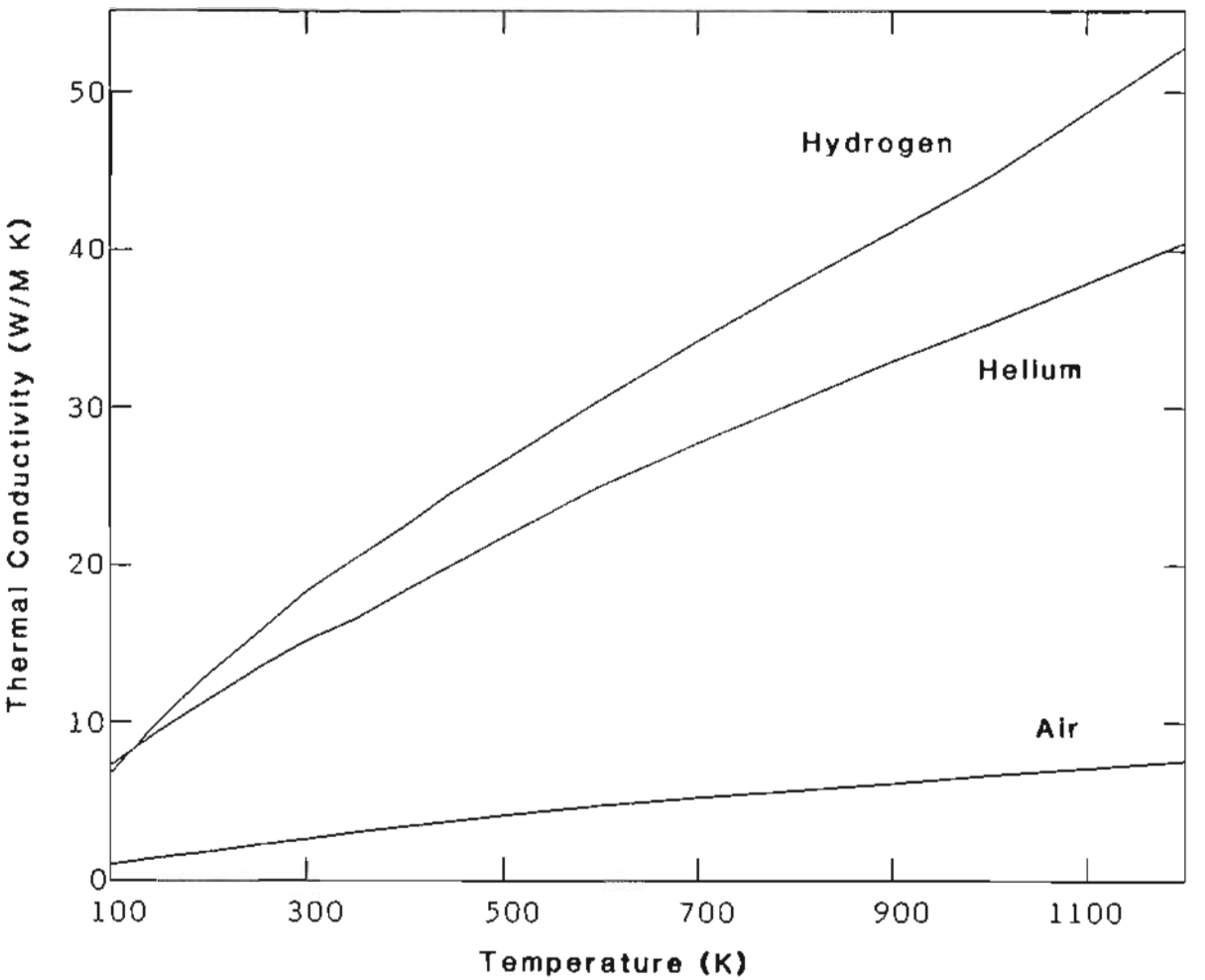

Figure 5.21. Thermal Conductivity of various gases as a function of temperature.

limited due to its explosive nature. Hence, it is better to use helium gas, which has the second highest thermal conductivity and is inert. >From the kinetic theory of gasses, an expression for the thermal conductivity of a monoatomic gas can be derived as (63,64),

$$k = \epsilon \eta c_v \tag{5.14}$$

where,

η = viscosity.

c_v = specific heat at constant volume.

$$\epsilon = \frac{9\gamma - 5}{4}$$

where, γ is the ratio of specific heat at constant pressure to that at constant volume. It is clear from the above expression, that the thermal conductivity of a gas is independent of pressure, which is valid as long as the pressure is higher than the range in which molecular flow occurs. The thermal conductivity of a gas remains practically constant over a large range of pressures (64,65) as shown in Figure 5.22. However at very low pressures, the thermal conductivity decreases linearly with the pressure. At moderate pressures (1 to 1000 mm Hg), the thermal conductivity increases by approximately 1/2 to 2% per atmospheric pressure (66).

Effect of Temperature

Temperature has a significant effect on the thermal conductivity of a gas. The thermal conductivity of a gas varies with temperature according to the expression (67),

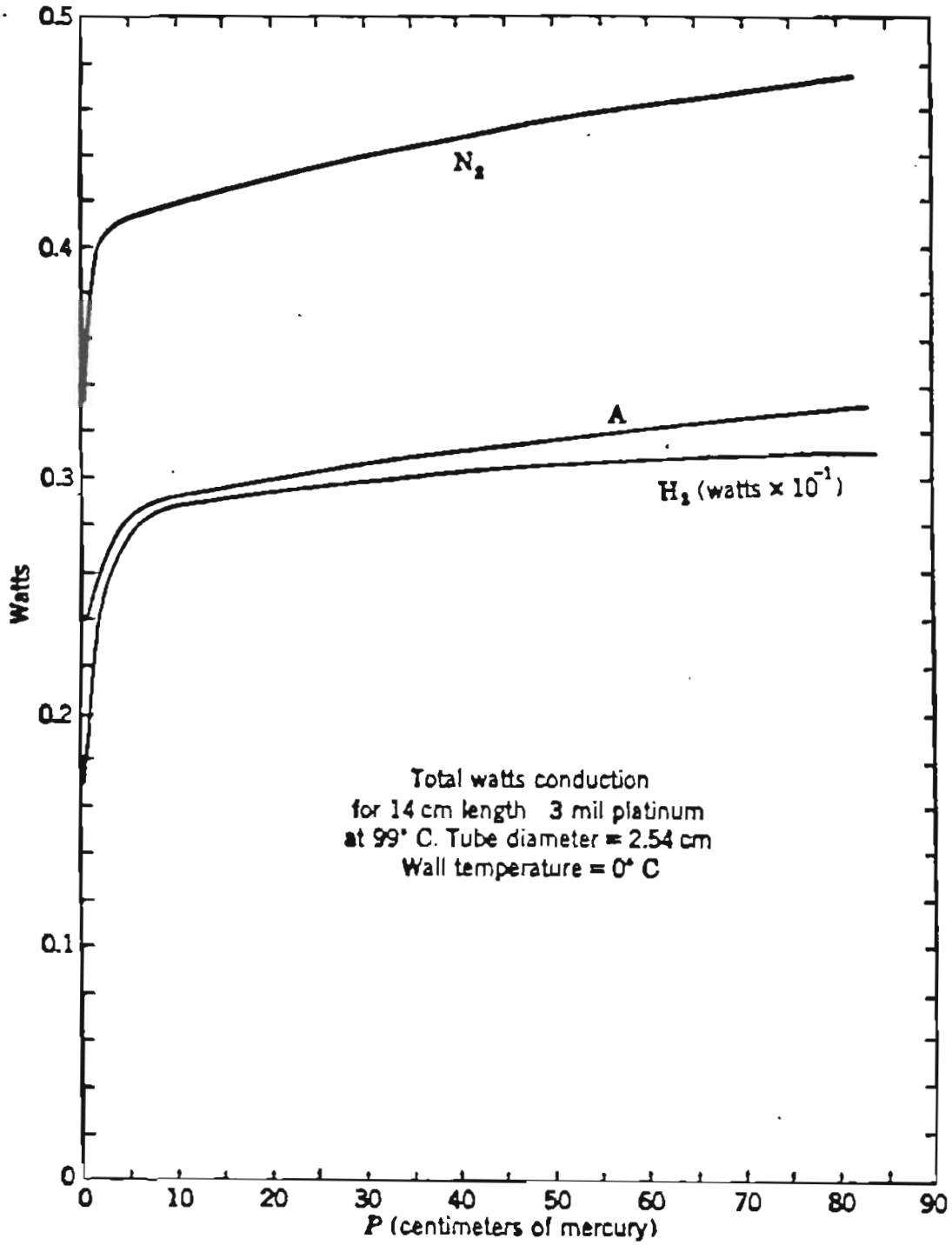

Figure 5.22. Thermal conductivity of gases as a function of pressure (65).

$$k(T) = \frac{1.989\times10^{-4}\sqrt{T}}{\sigma^2\Omega_k\sqrt{M}} \tag{5.15}$$

where,

T = temperature

M = molecular weight

σ = collision diameter

Ω_k = collision factor

The variation of the thermal conductivity of various gasses as a function of temperature is shown in Figure 5.21.

5.2.1.3. Heat Conduction by Gas

In the conventional treatment of exchange processes (momentum, energy etc), the structure of the gas is considered to be continuous, that is to say, no consideration need be given to the molecular structure of the gas. Flow and heat transfer phenomena under these continuum conditions can be described adequately in terms of the Reynold, Nusselt, Mach and Prandtl numbers. However, at very small absolute pressures, a gas partly looses its continuum characteristics and the mean free path λ of the gas molecules may become large compared to a characteristic dimension L, across which heat is transferred. In such cases , an additional dimensionless ratio, the Knudsen number, $Kn=\frac{\lambda}{L}$ (68,69) or its equivalent in terms of other ratios must be included in the analysis. The condition of the gas under these circumstances is called rarefied and Kn is a measure of the degree of rarefaction. It is usually convenient to subdivide the field of rarefied gas heat transfer into several different regimes, as shown in Figure 5.23

(69). The figure shows the temperature field T as it exists in a stagnant gas contained between two parallel walls of infinite length and with locally uniform temperatures, T_{w_1} and T_{w_2}.

For small values of Knudsen number, ($\frac{\lambda}{L} << 1$), the temperature drops linearly in the the gas from the value T_{w_1} to the value T_{w_2} as shown in Figure 5.23a. In the free molecule regime ($\frac{\lambda}{L} >> 1$), on the other hand, the temperature is uniform within the gas and a sudden jump in temperature occurs at both the walls. In the transition regime, the temperature changes as indicated in Figure 5.23c, with a jump and an adjoining large gradient near both the walls and with the gradient decreasing in magnitude as one moves away from either wall toward the center plane of the gas layer. Yet another regime which is between the continuum and transition, is characterized by the fact that, temperature drops almost linearly over the a major part of the gas layer with a steeper drop and a temperature jump confined to the thin regions adjacent to both the walls, as shown in Figure 5.23b. In this case, the mechanism of heat transfer in the central part of the layer is still the same as in the continuum regime and the molecular structure influences conditions only near the walls. It has been found that (69) an extrapolation of the straight line representing the temperature in the central part of the gas layer reaches the wall temperatures at a distance 'g' away from the wall surface and 'g' is called the temperature jump distance.

The ingot and the crucible in VAR can be considered as two coaxial cylinders with a shrinkage gap separating the two. In order to calculate the heat transfer by gas conduction, one need to determine which one of the above four

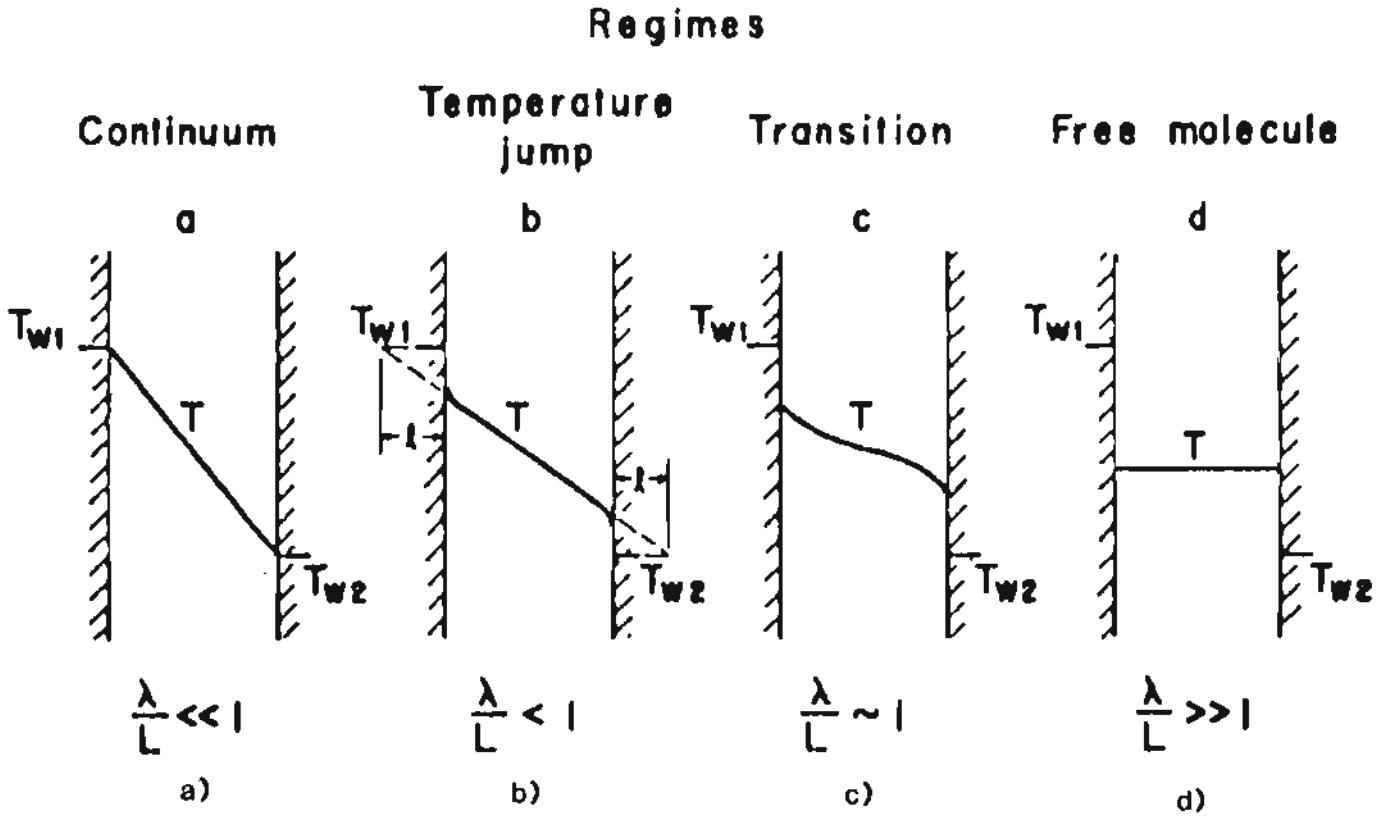

Figure 5.23. Heat conduction regimes in a rarefied gas (69).

regimes is appropriate in VAR under the operating gas pressures. From the Figure 5.23, it is clear that the regime can be determined by the Knudsen number, $\frac{\lambda}{L}$, where, λ is the mean free path of the helium gas molecules and L is the characteristic distance across which heat is transferred. In the case of VAR, L is the shrinkage gap between the ingot and the crucible. Samarasekera and Brimacombe (70) have estimated steady state gap width at different distances below the meniscus of molten metal pool during continuous casting of steel. They have reported (70) a gap width of 0.085 mm. In the present investigation a gap width of 0.1 mm is assumed to be present in VAR.

The mean free path of the gas molecules (λ) was calculated using the equation given below,

$$\lambda = \frac{kT}{\sqrt{2}\pi p \sigma^2} \tag{5.16}$$

where,

k = Boltzmann constant = 1.38×10^{-16} dyne -cm / K

σ = diameter of the gas molecule = 2.57 A (for helium)

p = pressure of the gas in dyne/cm^2

T = average temperature of the gas in K.

The average temperature T of the helium gas was calculated in terms of the temperature of the ingot and crucible by the equation (63),

$$\frac{1}{\sqrt{T}} = \frac{1}{2}\left(\frac{1}{\sqrt{T'_i}} + \frac{1}{\sqrt{T'_c}}\right) \tag{5.17}$$

and

$$T'_i = \frac{\left[\frac{r_i}{r_c}(1-a_c)+a_c\right]a_i T_i + a_c(1-a_i)T_i}{\left[\frac{r_i}{r_c}(1-a_c)+a_c\right]a_i + a_c - a_c a_i} \tag{5.18}$$

and,

$$T'_c = \frac{a_c T_c + a_i\left(\frac{r_i}{r_c}\right)(1-a_c)T_i}{\left[\frac{r_i}{r_c}(1-a_c)+a_c\right]a_i + a_c - a_c a_i} \tag{5.19}$$

where,

T_i = temperature of the ingot surface. Assuming this is just below the solidus temperature of Inconel 718 = 1600°K.

T_c = temperature of the inside surface of crucible = 450°K.

r_i = radius of the ingot in meters. = 0.0815 m.

r_c = radius of the crucible in meters.= 0.0825 m.

a_i = accommodation coefficient for the ingot. = 0.9 (46)

a_c = accommodation coefficient for the crucible. = 0.5 (46)

Substituting all the values, the average helium gas temperature was found to be 1200°K. The mean free path of the helium gas was then calculated at various pressures and is shown in Table 5.8. From the calculated mean free path values and the shrinkage gap, Knudsen numbers were calculated and are shown in Table 5.8. The Knudsen number varies from 2 with low gas pressures to 0.1 at 40 mm of gas pressure. In the present series of experiments, the pressure of the helium gas used was in the range of 20 mm to 60 mm. Hence for these pressure

TABLE 5.8

MEAN FREE PATH AND KNUDSEN NUMBERS AT VARIOUS HELIUM GAS PRESSURES

Pressure of He (mm of Hg)	Mean Free Path (mm)	Knudsen Number $(\frac{\lambda}{L})$
2	0.20	2.0
5	0.08	0.8
10	0.04	0.4
20	0.02	0.2
30	0.013	0.13
40	0.01	0.1
50	0.008	0.08
60	0.006	0.06

ranges, the calculated Knudsen numbers are less than 1. Hence, the dominant mechanism for heat transfer by helium gas, is the temperature jump regime from the Figure 5.23.

An equation for heat transfer by gas conduction between the ingot and crucible was derived from first principles. The following assumptions were made in deriving the equation.

(1) Heat transfer by solid conduction in the gap region is neglected. When melting under vacuum, heat transfer across the gap is mainly by radiation.

(2) The ingot and crucible lengths are assumed sufficiently long, hence, heat flow is in the radial direction only, and axial heat flow is negligible.

(3) When gas is introduced in the gap between the ingot and crucible, heat transfer is by gas conduction and radiation only. Heat transfer by convection is neglected since the gas pressures involved are low.

Let r_i and r_c be the radius of the ingot and crucible respectively and let g_i and g_c be the temperature jump distances for ingot and crucible as shown in Figure 5.24. and k_g be thermal conductivity of the gas. Then from the figure, it can be written that,

$$R_i = r_i - g_i \tag{5.20}$$

and

$$R_c = r_c + g_c \tag{5.21}$$

One can consider the ingot and crucible system as two coaxial cylinders separated by a small gap containing a gas. One can write for the rate of heat conduction between the ingot and crucible as,

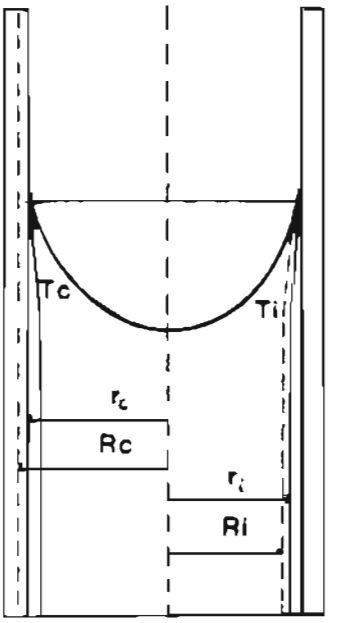

r_i = Radius of ingot

r_c = Radius of crucible

g_i = Temperature jumpdistance for ingot

g_c = Temperature jumpdistance for crucible

$$R_i = r_i - g_i$$

$$R_c = r_c + g_c$$

Figure 5.24. VAR schematic with various terms defined for gas cooling.

$$q = - k_g A \frac{dT}{dr} \tag{5.22}$$

where,

k_g = thermal conductivity of the gas

A = area = $2\pi rl$

$\frac{dT}{dt}$ = temperature gradient in the radial direction

Substituting for area,

$$q = - k_g (2\pi rl) \frac{dT}{dr} \tag{5.23}$$

Separating the variables and integrating between the limits T_c at R_c and T_i at R_i, One can get,

$$q \int_{R_i}^{R_c} \frac{dr}{r} = - k_g 2\pi l \int_{T_i}^{T_c} dT \tag{5.24}$$

i.e.

$$q \ln \left(\frac{R_c}{R_i} \right) = - k_g 2\pi l \, (T_c - T_i) \tag{5.25}$$

Since, $T_i >> T_c$, One gets,

$$q \ln \left(\frac{R_c}{R_i} \right) = k_g 2\pi l \, \Delta T \tag{5.26}$$

Then heat conduction per unit area is,

$$\frac{q}{A} \ln \left(\frac{R_c}{R_i} \right) = k_g \left(\frac{2\pi l}{2\pi rl} \right) \Delta T \tag{5.27}$$

Simplifying,

$$\frac{q}{A} \ln \left(\frac{R_c}{R_i} \right) = \frac{k_g}{r} \Delta T \tag{5.28}$$

Now Consider the term, $\ln\left(\frac{R_c}{R_i}\right)$

Substituting for R_c and R_i ,

$$\ln\left(\frac{R_c}{R_i}\right) = \ln\left[\frac{(r_c + g_c)}{(r_i - g_i)}\right] \tag{5.29}$$

$$= \ln(r_c + g_c) - \ln(r_i - g_i) \tag{5.30}$$

Rearranging the terms,

$$= \ln\left\{r_c\left(1 + \frac{g_c}{r_c}\right)\right\} - \ln\left\{r_i\left(1 - \frac{g_i}{r_i}\right)\right\} \tag{5.31}$$

Simplifying,

$$= \ln r_c + \ln\left\{1 + \frac{g_c}{r_c}\right\} - \ln r_i - \ln\left\{1 - \frac{g_i}{r_i}\right\} \tag{5.32}$$

Since, $r_i >> g_i$ and $r_c >> g_c$,

One can use the logarithmic expression,

$$\ln(1 + x) = x - \frac{1}{2}x^2 + \text{.....(for small 'x')} \tag{5.33}$$

Using the above logarithmic expression

$$\ln\left(1 + \frac{g_c}{r_c}\right) = \frac{g_c}{r_c} \tag{5.34}$$

$$\ln\left(1 - \frac{g_i}{r_i}\right) = -\frac{g_i}{r_i} \tag{5.35}$$

Substituting the above into 5.29,

$$\ln\left(\frac{R_c}{R_i}\right) = \ln\frac{r_c}{r_i} + \frac{g_c}{r_c} + \frac{g_i}{r_i} \tag{5.36}$$

Hence, substituting in the equation,

$$\frac{q}{A} \ln \left(\frac{R_c}{R_i} \right) = \frac{k_g}{r} \Delta T \tag{5.37}$$

i.e. ,

$$\frac{q}{A} = \frac{k_g \ \Delta T}{r \left(\ln \left(\frac{r_c}{r_i} \right) + \frac{g_c}{r_c} + \frac{g_i}{r_j} \right)} \tag{5.38}$$

Also, $\frac{q}{A}$ per degree difference is h_g , where h_g is the heat transfer coefficient, and $\Delta T = 1^{\circ}C$ One can get,

$$h_g = \frac{k_g}{r \left(\ln \left(\frac{r_c}{r_i} \right) + \frac{g_c}{r_c} + \frac{g_i}{r_j} \right)} \tag{5.39}$$

Hence using the above equation, it is possible to calculate the heat transfer coefficient by gas conduction.

Now the temperature jump distances are related to pressure of the gas by (63),

$$g = \frac{2 - a}{a} (2\pi RT)^{\frac{1}{2}} \frac{k_g}{(\gamma+1) c_v p} \tag{5.40}$$

where,

p = gas pressure.

a = accommodation coefficient

Hence, it can be seen that, temperature jump distance is inversely proportional to gas pressure, one can write $g \approx \frac{\beta}{p}$, where β is a constant. Then,

$$g_c = \frac{\beta_c}{p} \text{ and } g_i = \frac{\beta_i}{p} \tag{5.41}$$

Substituting,

$$h_g = \frac{k_g}{r_i \left(\ln\left(\frac{r_c}{r_i}\right) + \frac{\beta_i}{p\, r_i} + \frac{\beta_c}{p\, r_c} \right)} \tag{5.42}$$

It can be seen that, heat transfer coefficient by gas conduction increases with the gas pressure.

5.2.1.4 Calculation of Temperature Jump Distances

In order to calculate the heat transfer coefficient due to gas conduction, one needs to determine the temperature jump distances. The temperature jump distance represents a length. According to Poisson (63), at a wall bounding an unequally heated gas, there might be a discontinuity of temperature. He derived an expression for the discontinuity as,

$$T_k - T_w = g \frac{\partial T}{\partial n} \tag{5.43}$$

where,

T_w = wall temperature

T_k = temperature of the gas.

This temperature of the gas is that which would be if the temperature gradient along the outward normal to the wall, $\frac{\partial T}{\partial n}$, continued without change right up to the wall itself. The constant 'g' represents a length and may be called the temperature jump distance. Smoluchowski (63) performed experiments and found that the temperature jump distance is inversely proportional to the pressure and

directly proportional to the mean free path. From the kinetic theory of gasses, (63) an equation has been derived for the temperature jump distance :

$$g = \frac{2-a}{a}\sqrt{(2\pi RT)}\frac{k}{(\gamma+1)c_v p} \qquad (5.44)$$

where,

R = gas constant = 2078 J/kg K for helium.

c_v = Specific heat = 3135 J/kg K for helium.

γ = 1.66 for helium.

k = thermal conductivity of helium at 1200°K = 0.364 W/m K.

p = pressure of the gas in N/ m^2.

a = Accommodation coefficient , For the crucible, a = 0.5 For ingot, a = 0.9 (46).

The values of temperature jump distances have been calculated for helium, argon and air at various pressures are given in Table 5.9. It can be seen that, as the pressure of the gas increases, the temperature distance decreases. The temperature jump distances for air are much lower than those for helium gas. The higher the molecular weight, the smaller is the temperature jump distance. Ross and Stout (71) graphically evaluated the values of temperature jump distances for various gasses from the measured values of heat transfer coefficients. The temperature jump distances for helium gas were higher than those of argon gas which were higher than those for krypton gas. At 760 mm of helium gas pressure, they (71) reported that the sum of temperature jump distances was 10×10^{-4}cm. In the present calculation, the sum of the temperature jump distances at 760 mm helium gas pressure was found to be 7×10^{-4}cm. Hence, the calculated values of temperature jump distances are fairly in agreement with the

TABLE 5.9

CALCULATED TEMPERATURE JUMP DISTANCES FOR HELIUM, ARGON AND AIR AT VARIOUS GAS PRESSURES

Gas Pressure (mm of Hg)	'g' of Crucible (mm)	'g' of Ingot (mm)
	FOR HELIUM GAS	
2	1.9	0.776
10	0.38	0.156
20	0.19	0.077
40	0.095	0.038
50	0.076	0.0312
60	0.063	0.026
760	0.005	0.002
	FOR ARGON GAS	
60	0.0193	0.00787
760	0.0015	0.00062
	FOR AIR	
760	0.0016	0.00065

estimated values of temperature jump distances from the experimentally measured heat transfer coefficients.

5.2.1.5. Theoretical Heat Transfer Coefficient Between The Ingot And Crucible.

Radiative Heat Transfer Coefficient :

When there is no gas between the ingot and the crucible, the heat transfer is by radiation only. Hence, one needs to calculate the radiative heat transfer coefficient between the ingot and the crucible. The heat transfer coefficient due to radiation, is given by (72) :

$$h_r = \sigma T_m \frac{[4T_m^2 + (\Delta T)^2]}{\frac{1}{\epsilon_1} + \frac{1}{\epsilon_2} - 1} \tag{5.45}$$

where,

$$T_m = \frac{(T_1 + T_2)}{2} \tag{5.46}$$

and

$$\Delta T = T_1 - T_2 \tag{5.47}$$

where,

σ = Stefan - Boltzmann Constant = 1.335×10^{-12} cal/sec $cm^2 - {}^{\circ}K^4$

T_1 = inside surface temperature of copper crucible = $450^{\circ}K$

T_2 = ingot surface temperature, taken to be just below the solidus temperature of Inconel-718

ϵ_1 = emissivity of the copper crucible

ϵ_2 = emissivity of the ingot surface.

During melting, as the inside surface of the crucible is coated, one can take ϵ_1=1. Jacobi (41) has determined the emissivity of iron during vacuum casting as 0.45. Hence, taking ϵ_2=0.45, one can calculate the heat transfer coefficient due to radiation as :

$$h_r = \frac{1.335\times10^{-12}\times1025[4\times(1025)^2+(1150)^2]}{\frac{1}{0.45}} \tag{5.48}$$

i.e.

$$h_r = 0.34\times10^{-2}\,\text{cal/cm}^2\text{secK} \tag{5.49}$$

i.e.

$$h_r = 142\ \text{W/m}^2\text{K} \tag{5.50}$$

Note that this value represents the maximum radiative heat transfer coefficient as it was calculated for the case when the ingot just pulls away from the crucible.

Heat Transfer Coefficient Between The Ingot And Crucible Due To Gas Conduction

In the previous section, the heat transfer coefficient due to radiation was calculated. If a gas (at low pressures) is introduced into the gap between the crucible and ingot, then, the heat transfer is due to gas conduction in addition to radiation. In this section, the heat transfer coefficient due to gas conduction was calculated for the crucible and ingot sizes involved in the present investigation. K. O. Yu (46) has calculated the heat transfer coefficient due to helium gas conduction in VAR at various gap widths and at different gas pressures. The

calculations were for a 508 mm diameter crucible. In the present investigation, the heat transfer coefficients were recalculated for the smaller crucible size involved. A sample calculation is shown below and following are the particulars used in the calculation.

Gas = Helium.

Gap width = 0.1 mm = 0.0001 m

Crucible radius (r_c) = 0.0825 m

Ingot radius (r_i) = 0.0824 m

Gas pressure = 40 mm

Temperature Jump distance for crucible (g_c)=0.000095m.

Temperature jump distance for ingot (g_i)=0.000038m.

Thermal conductivity of helium gas at 1200°K=0.364W/m^{2}K .

Using the equation 5.34 as given below, one can calculate the heat transfer coefficient due to gas conduction.

$$h_{gas}=\frac{k_{gas}}{r_i \ln(\frac{r_c}{r_i}+\frac{g_c}{r_c}+\frac{g_i}{r_i})} \tag{5.51}$$

Substituting the above values,

$$h_{gas}=\frac{0.364}{0.0824(\ln\frac{0.0825}{0.0824}+\frac{0.000095}{0.0825}+\frac{0.000038}{0.0824})} \tag{5.52}$$

i.e.

$$h_{gas}=1561.3 \text{ W/m}^2\text{K} \tag{5.53}$$

It can be seen that, the heat transfer coefficient due to helium gas conduction (40 mm Hg) is about 10 times as compared to heat transfer coefficient due to

radiation. Figure 5.25 shows a plot of the calculated heat transfer coefficients by helium gas conduction between the ingot and the crucible at various gas pressures and gap widths. From the figure, it is clear that, the heat transfer coefficient increases with an increase in the gas pressure. The heat transfer coefficient decreases with increased gap width, which is in agreement with the Fourier law of heat conduction. The effect of gap width is more significant above 0.1 mm and with higher helium gas pressures as shown in figure 5.25. For example, with 760 mm helium pressure at 1 mm gap, the heat transfer coefficient is 363 W/m^2K and with the same helium gas pressure, at a 0.001 mm gap, the heat transfer coefficient is 45787 W/m^2K. With 2 mm of helium gas pressure at 1mm gap width, the heat transfer coefficient is 100 W/m^2K and at the same gas pressure, but at 0.001 mm gap, the heat transfer coefficient is $136W/m^2K$. This indicates that, the gap width has a more significant effect at higher gas pressures as compared to lower gas pressures. This could be explained in terms of the previously calculated temperature jump distances. At 760 mm of helium gas pressure, the calculated temperature jump distances for crucible and ingot are 0.005 mm and 0.002 mm respectively. With 1 mm of gap width, these temperature jump distances become insignificant and hence gap width is the dominant factor. At 2 mm of helium gas pressure, the calculated temperature jump distances for the crucible and the ingot are 1.9 mm and 0.776 mm respectively. These temperature jump distances become significant both, at 1mm and 0.001 mm gap width. Hence the heat transfer coefficient is not affected significantly at 0.001 mm gap width as compared to 1 mm gap width and temperature jump distance is the dominant factor.

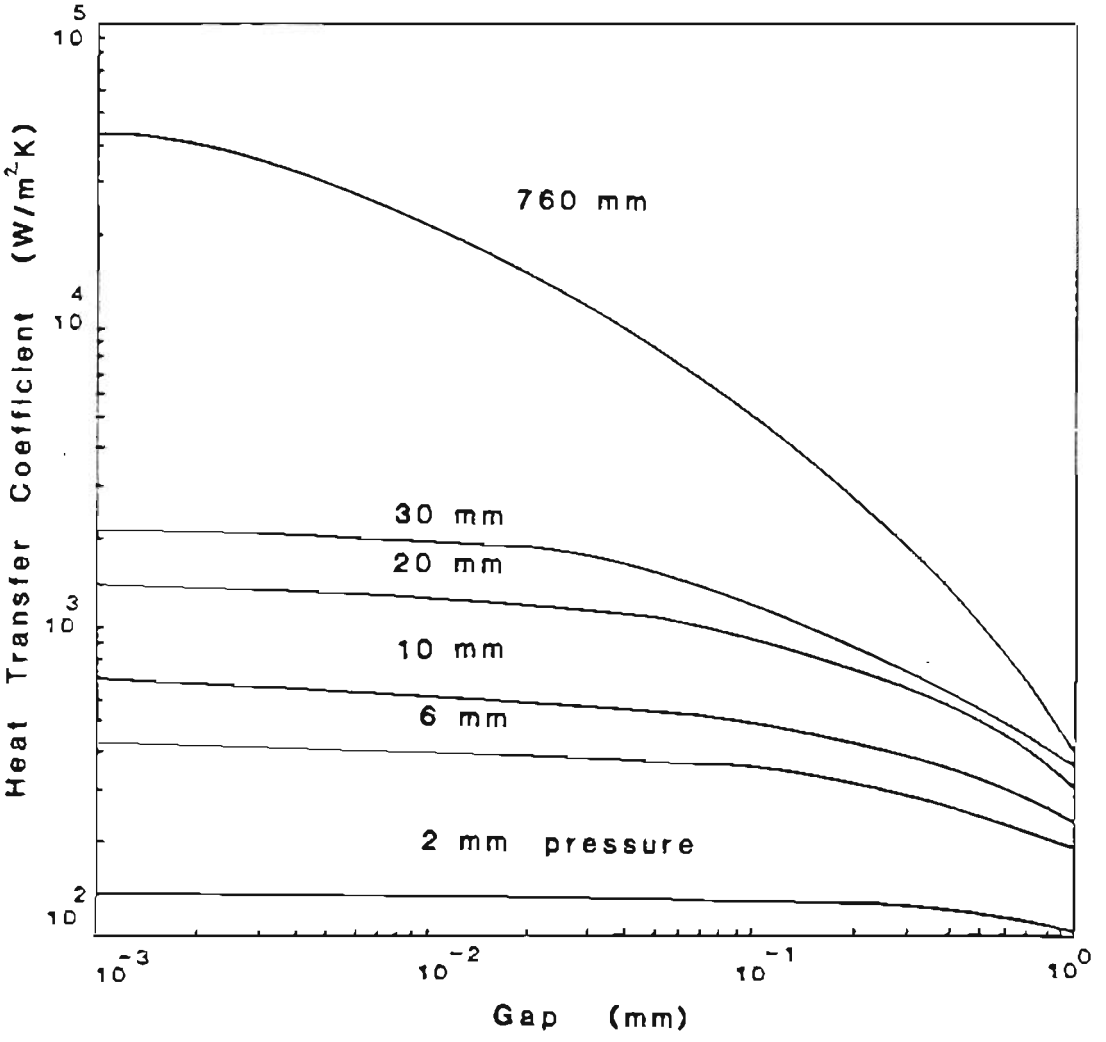

Figure 5.25. Calculated heat transfer coefficient as a function of gas pressure at various gap widths.

Figure 5.26 shows a plot of the comparison of heat transfer coefficients at 760 mm gas pressure for helium and argon. The heat transfer coefficients due to helium gas are much higher than those due argon as the thermal conductivity of helium gas about 8 times that of argon gas at 1200°K. Note that, the heat transfer coefficient due to helium gas is however, not 8 times greater than that due to argon gas conduction. This can be explained in terms of the molecular weights of the gasses, as discussed below.

The energy exchange between a gas and a surface is much higher for heavier gasses as compared to lighter gasses. Hence, the heat transfer with argon gas is much better as argon gas is heavier than helium. This effect is clearly seen in the calculated temperature jump distances. At 40 mm helium gas pressure, the calculated temperature jump distances for the crucible and the ingot are 0.095 mm and 0.038 mm respectively, whereas, for argon at the same pressure, the temperature jump distances for the crucible and the ingot are 0.0193 mm and 0.00787 mm respectively. The temperature jump distances for argon gas are much smaller than those for helium gas and hence, argon gas has a lower resistance for heat conduction than helium gas.

5.2.1.6. Comparison of Theoretical Heat Flux due to Radiation and Gas Conduction

This section compares the theoretical heat fluxes due to radiation and gas conduction. The heat flux due to radiation is given by :

$$\dot{q}_r = \frac{\sigma}{\frac{1}{\epsilon_1} + \frac{1}{\epsilon_2} - 1} (T_2^4 - T_1^4) \tag{5.54}$$

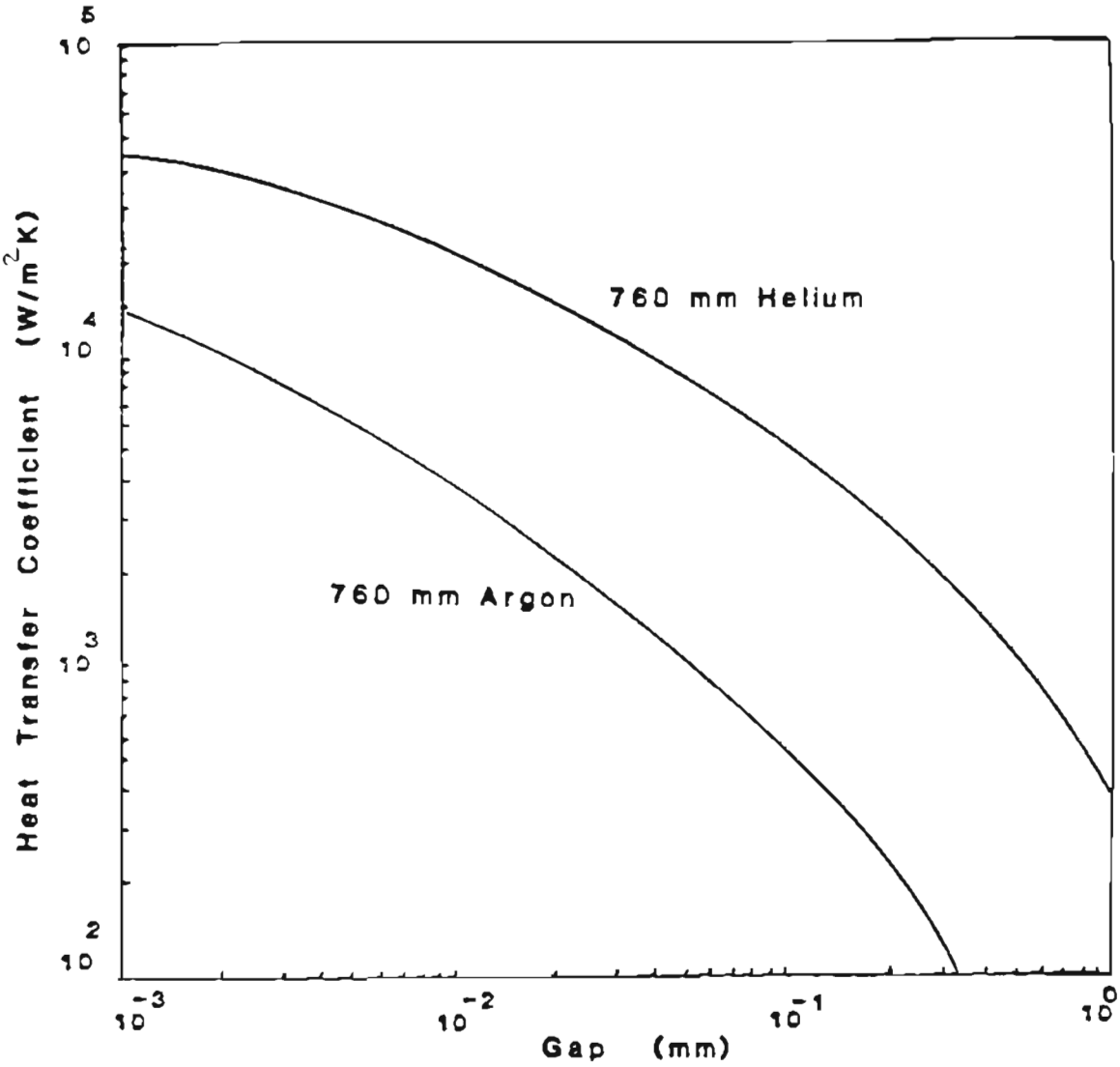

Figure 5.26. Comparison of calculated heat transfer coefficient due to helium and argon gas conduction.

where,

$\dot{q}_r$ = radiation heat flux.

σ = Stefan - Boltzmann Constant = 1.335×10^{-12}cal/sec$-$cm$^{2^\circ}$K^4.

T_1 = inside surface temperature of copper crucible = 450°K.

T_2 = ingot surface temperature; taken to be just below the solidus temperature of Inconel 718. = 1600°K

ϵ_1 = emissivity of the copper crucible = 1

ϵ_2 = emissivity of the ingot surface = 0.45

Substituting the above values into the equation 5.54, we get :

$$\dot{q}_r = \frac{1.335\times10^{-12}}{\frac{1}{0.45}}((1600)^4-(450)^4) \tag{5.55}$$

$$\dot{q}_r = 3.165\text{cal/cm}^2\text{sec} \tag{5.56}$$

i.e.

$$\dot{q}_r = 13.229\text{W/cm}^2 \tag{5.57}$$

or

$$\dot{q}_r = 132290\text{W/m}^2 \tag{5.58}$$

Hence, the heat flux due to radiation is 132290 W/ m^2

Heat Flux due to helium gas conduction

Now the heat flux due to helium gas conduction can be calculated by :

$$\dot{q}_{gas} = h_{gas}\times(T_2-T_1) \tag{5.59}$$

where,

$\dot{q}_{gas}$ = heat flux due to gas conduction

h_{gas} = heat transfer coefficient due to gas conduction

T_1 = inside surface temperature of copper crucible = 450°K

T_2 = ingot surface temperature; taken to be just

below the solidus temperature of Inconel-718 = 1600°K

For example, heat flux due to helium gas conduction at 2 mm pressure can be calculated. With 2mm helium gas pressure the calculated heat transfer coefficient, h_{gas} is 130.7 w/m^2 K and $T_2 - T_1$ = 1150°K, then,

$$\dot{q}_{gas} = 130.7 \times 1150 \tag{5.60}$$

i.e.

$$\dot{q}_{gas} = 150305 W/m^2$$

The above heat flux due to helium gas is higher than the heat flux due to radiation which is about $132290 W/m^2$, indicating that, the heat removed by 2 mm of helium gas pressure in the gap between the ingot and the crucible is more than the heat removed by radiation. This also shows that 2 mm of helium gas in the gap between the ingot and crucible can more than double the heat extraction rate. Figure 5.27 shows the plot of the calculated heat flux due to helium gas conduction and radiation at two different gas pressures. The radiative heat flux is independent of the gap width as expected. But, the heat flux due to helium gas conduction with 2 mm pressure is slightly more than the radiative heat flux up to a gap width of 0.1 mm and for gap widths greater than 0.1 mm, the heat flux due to helium gas conduction falls below the radiative heat flux.

Jacobi (41) studied the effect of various gas atmospheres on the heat transfer between the ingot and the crucible, during conventional ingot casting of iron. The expression Jacobi used for calculating the heat flux due to gas conduction is

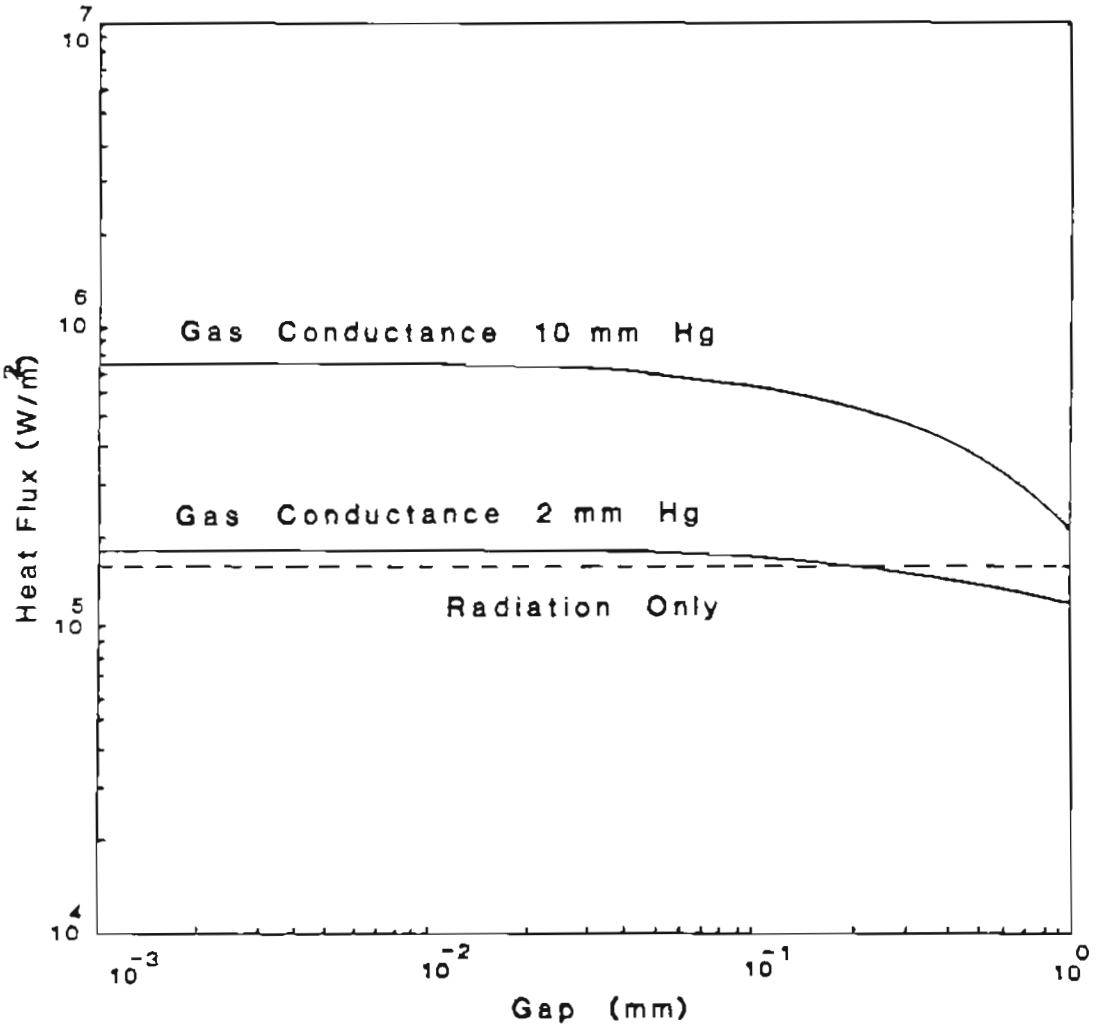

Figure 5.27. Calculated heat flux due to helium gas conduction and radiation.

given as,

$$\dot{q}_{gas} = \frac{1.989 \times 10^{-4}}{\delta \sigma^2 \Omega_K \sqrt{M}} \times \frac{2}{3} [T_2^{\frac{3}{2}} - T_1^{\frac{3}{2}}] \qquad (5.61)$$

where,

$\dot{q}_{gas}$ = heat flux due to gas conduction.

δ = gap width.

σ = collision diameter in A.

M = molecular weight of the gas

Ω_K = collision factor

T_2 = temperature of the ingot

T_1 = temperature of the inside surface of mould

It can be seen that, the above expression has no pressure or pressure related terms. Probably the expression could be used for calculating heat flux in the continuum region.

5.2.1.7. Free - Molecule Heat Conduction

In the previous sections the heat conduction in the temperature jump regime and the continuum regime was discussed. The opposite extreme condition in which gas conduction occurs between surfaces so very close together or at very low pressures is the free-molecular. In this condition collisions between molecules are rare as compared to collisions of molecules with the walls and, this is free molecule heat conduction. For free molecule heat conduction, the Knudsen number, Kn $>>$ 1. The heat transfer coefficient in the free molecule region is given (63) by,

$$h_g = \frac{a_i a_c}{a_c - a_i a_c + a_i\left[\frac{r_i}{r_c}(1-a_c)+a_c\right]} A_g \tag{5.62}$$

Where,

$$A_g = \frac{1}{2}(1+\gamma)\frac{c_v p}{(2\pi RT)^{\frac{1}{2}}} \tag{5.63}$$

where,

h_g = free molecule heat transfer coefficient

a_i = accommodation coefficient for the ingot

a_c = accommodation coefficient for the crucible

γ = ratio of specific heats

r_i = radius of the ingot

r_c = radius of the crucible

p = gas pressure

The calculated heat transfer coefficients are plotted in Figure 5.28. It can be seen that the heat transfer coefficient is independent of the gap width and depends only on the gas pressure. Within the present experimental conditions, this type of heat transfer is unlikely to occur. It has been discussed for completion of the different regimes of gas conduction.

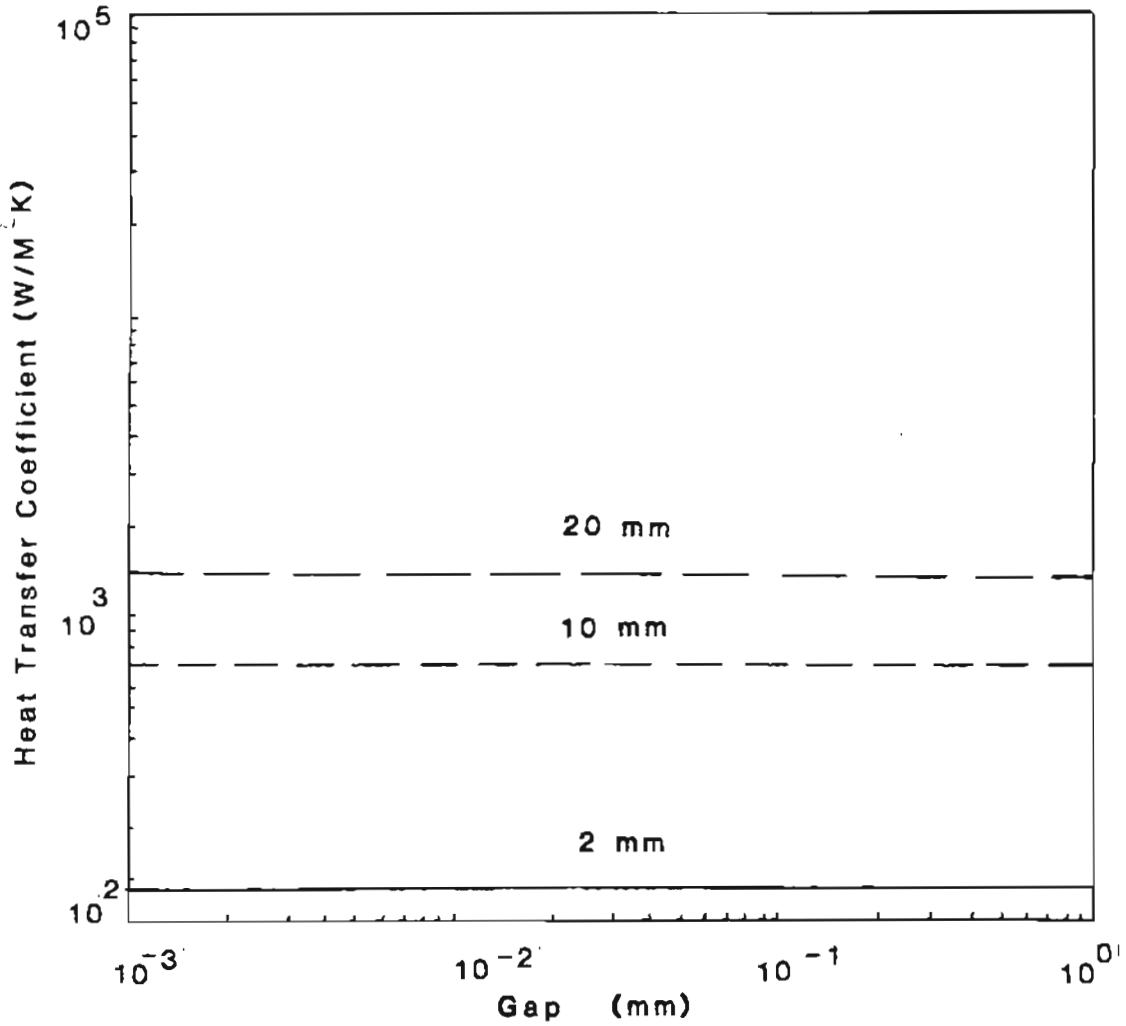

Figure 5.28. Calculated heat transfer coefficient due to free molecular heat conduction.

5.2.2. Experimental Heat Transfer

5.2.2.1. Temperature Profile On Crucible Wall

A limited number of experimental studies (7,15) have been carried out on the heat transfer in VAR. Only Soviet investigators (44,45) have reported heat transfer studies with helium gas between the ingot and the crucible. They have not, however, quantified the heat removal rate at various gas pressures. In the present investigation, this objective was achieved. The heat removal rate with different gasses (argon vs. helium) was also compared.

The material used in the present investigation was Inconel 718, a widely used superalloy in gas turbine applications. The experimental details of the melts are given in Table 5.10. In all the melts, the same melting parameters were used. The melting current used was 3000 Amps and the electrode gap was 15 mm. One melt was made with no gas cooling for the purpose of comparison. The vacuum level in the chamber for the melt with no gas cooling was about 8 microns. As the gas pressure in the gap between the ingot and the crucible was increased, the pressure in the melting chamber increased slightly. With 40 mm of helium gas pressure in the gap the vacuum level in the melting chamber was about 12 micron and with 60 mm helium gas pressure the vacuum level was about 17 microns. This was possibly due to leakage of some gas through the crown.

As discussed earlier (in the experimental section) the first attempt on heat transfer studies with exposed junction, general purpose chromel/alumel thermocouples was not successful. These thermocouples were subsequently replaced by electrically isolated, stainless steel sheathed chromel/alumel thermocouples.

TABLE 5.10

PARTICULARS OF INCONEL 718 MELTS

Parameter	Melt No. 47	Melt No. 49	Melt No. 50	Melt No. 53
Current(KA)	3.0	3.0	3.0	3.0
Voltage(V)	25	25	25	25
Gas Pressure(mm)	0.0	40	60	60(Argon)
Flow Rate(LPM)	0.0	0.5	0.7	0.6
Vacuum(u)	8	12	17	20
Power(KW)	75	75	75	75
Ingot Wt.(kg)	62.25	72.70	70.0	69.0
Melt Time(min)	33	38	35	36.5
Melt Rate(kg/min)	1.89	1.9	1.94	1.89

Since the interest was only in the quasi-steady state condition, the thermocouples on the bottom of the crucible were removed, as the heat extraction from the bottom of the crucible is negligible in the quasi-steady state condition. The temperature of each thermocouple was sampled at every 15 seconds. Figure 5.29 shows a plot of the measured temperature of five thermocouples as a function of melting time for melt number 47. Melt number 47 was done with no gas cooling. The zero time corresponds to the time when the full melting current of 3000 Amps was applied, which was about 1 minute, after the power supply was initiated. The plot shows the variation of temperature of the five thermocouples when the molten metal pool moves through them. The positions of the five thermocouples with respect to the bottom stool are given below :

Thermocouple Number	Distance from the Bottom stool in cm
1	0.00
4	15.20
8	31.75
9	33.00
10	38.10

It can be seen that the peak temperature reached by thermocouple number 1 is about 68°C as compared to that of thermocouple number 8 which read 99°C. This is due to the fact that, thermocouple 1 did not achieve the quasi-steady state, hence a significant amount of heat was extracted through the bottom stool, ie axial heat conduction was considerable. Thermocouple number 4, which is placed at about 15 cm from the bottom, is about midway between thermocouples

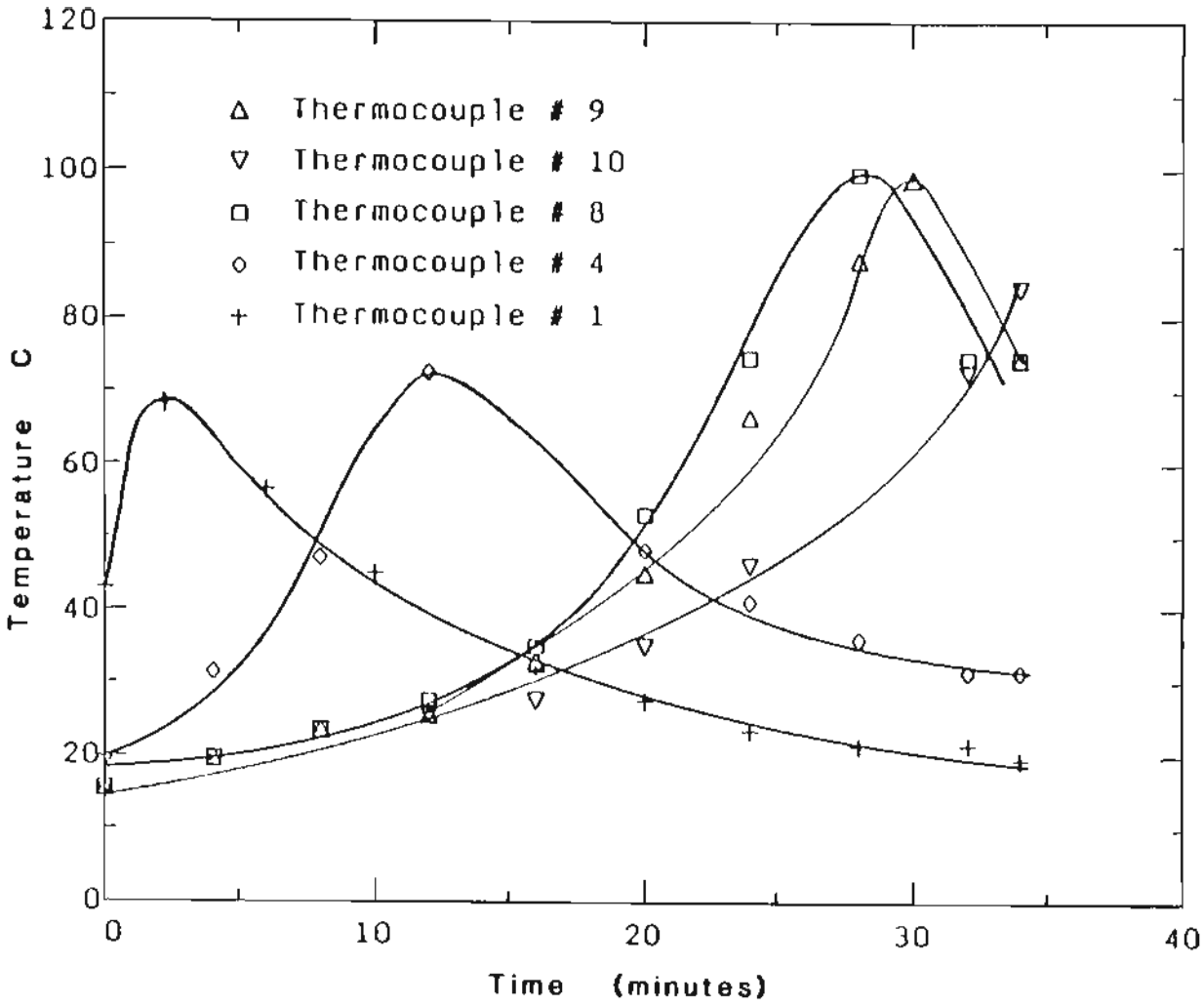

Figure 5.29. Temperature reading of five thermocouples as a function of melt time for melt number 47.

number 1 and 8. The peak temperature achieved by it is above that of thermocouple number 1, as the heat extracted through the bottom stool was reduced. Thermocouple number 10 is at about 38 cm from the bottom and the molten metal pool did not cross it, as the ingot height was only about 36.5 cm. Hence thermocouple number 10 did not achieve the peak temperature. The peak temperature reached by thermocouple number 9 is the same as that reached by thermocouple number 8. It can also be seen that the temperature profile of thermocoupe number 9 is the same as that of thermocouple number 8, but only shifted on the time scale.

The shift of the peak temperature of thermocouple number 9 from that of thermocouple number 8 should be in agreement with the ingot growth rate. The ingot growth rate for melt 47 was 1.12 cm/min, and thermocouples number 8 and number 9 are separated by 1.25 cm. Thus the time shift in the peak temperature of these thermocouples should be about one minute. Figure 5.29 indicates that thermocouple number 8 reaches its peak temperature in the 28^{th} minute from the time of full power on while thermocouple number 9 reaches its peak temperature in the 29^{th} minute. Thus there is a difference of 1 minute and the distance between them is 1.25 cm. This data is in agreement with the ingot growth rate. These results imply that when the molten metal pool is above thermocouple number 8, the system reaches its quasi-steady state. This was also confirmed by an experimental investigation on molten metal pool profile. The molten metal pool was found to reach quasi-steady state at an ingot height of twice the ingot diameter, which approximately corresponds to the position of thermocouple number 8. Hence, both the measurements are in good agreement.

Figure 5.30 shows the quasi-steady state temperature distribution on the crucible wall for melt no. 47 (with no gas cooling). The temperature distribution is plotted for the case when the molten metal passes through thermocouple number 9. The negative ('- ') distance shown indicates a distance below the pool, while a positive ('+') distance represents a distance above the pool. For melt 47, the velocity of the molten metal pool was 1.12 cm/min. Figure 5.30 is the plot of temperature distribution on the crucible wall at the 29^{th} minute after the start of full power. At this instant, the pool position was 32.2 cm. This is calculated from the velocity of the metal pool. But thermocoupe number 9 is at 33 cm from the bottom. Hence, there is an uncertainity of about 0.8 cm in knowing the exact pool position.

Figure 5.31 shows the plot of comparison of temperature distribution on the crucible wall for the case of no gas cooling as compared to that of gas cooling using 60 mm pressure of helium. The plot shows the temperature distribution on the crucible wall when the molten metal pool position was at 33 cm from the bottom of the crucible. For melt number 47, the plot shows the temperature distribution at the 29^{th} minute from the time of full current and the electrode feed at the time was 38 cm. These data were obtained accurately with the help of a data acquisition computer. For melt number 50 (with gas cooling), the plot shows the temperature distribution on the crucible wall at $28\frac{1}{2}$ minutes from the time of full current and the electrode feed at this time was 37.25 cms. Considering that the present electrode feed system is manual, the agreement between the electrode position for the two melts is good. The figure 5.31 shows that there is no difference in the peak temperature of the two melts. Also the temperature of

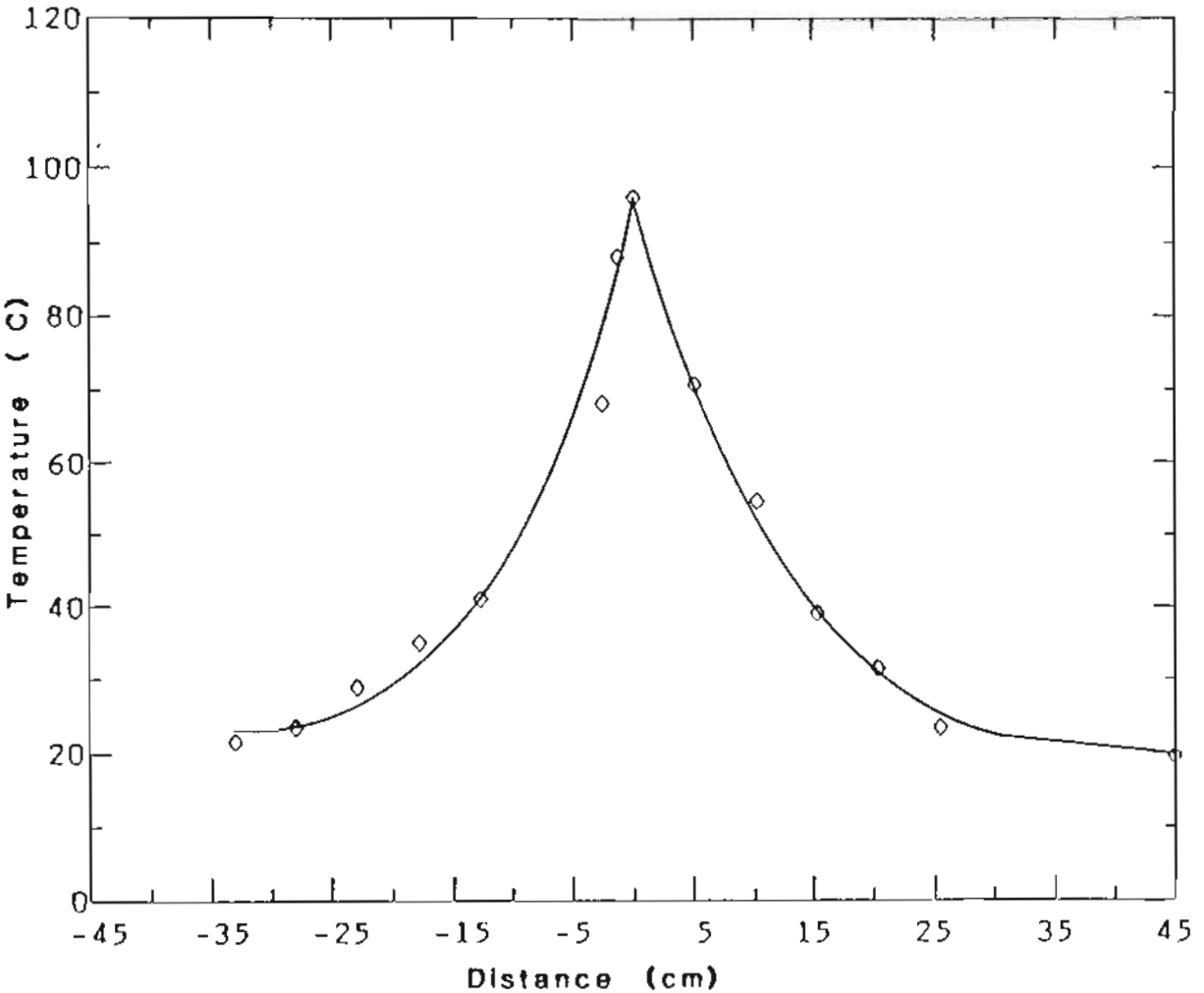

Figure 5.30. Quasi-steady temperature distribution on crucible wall for melt number 47.

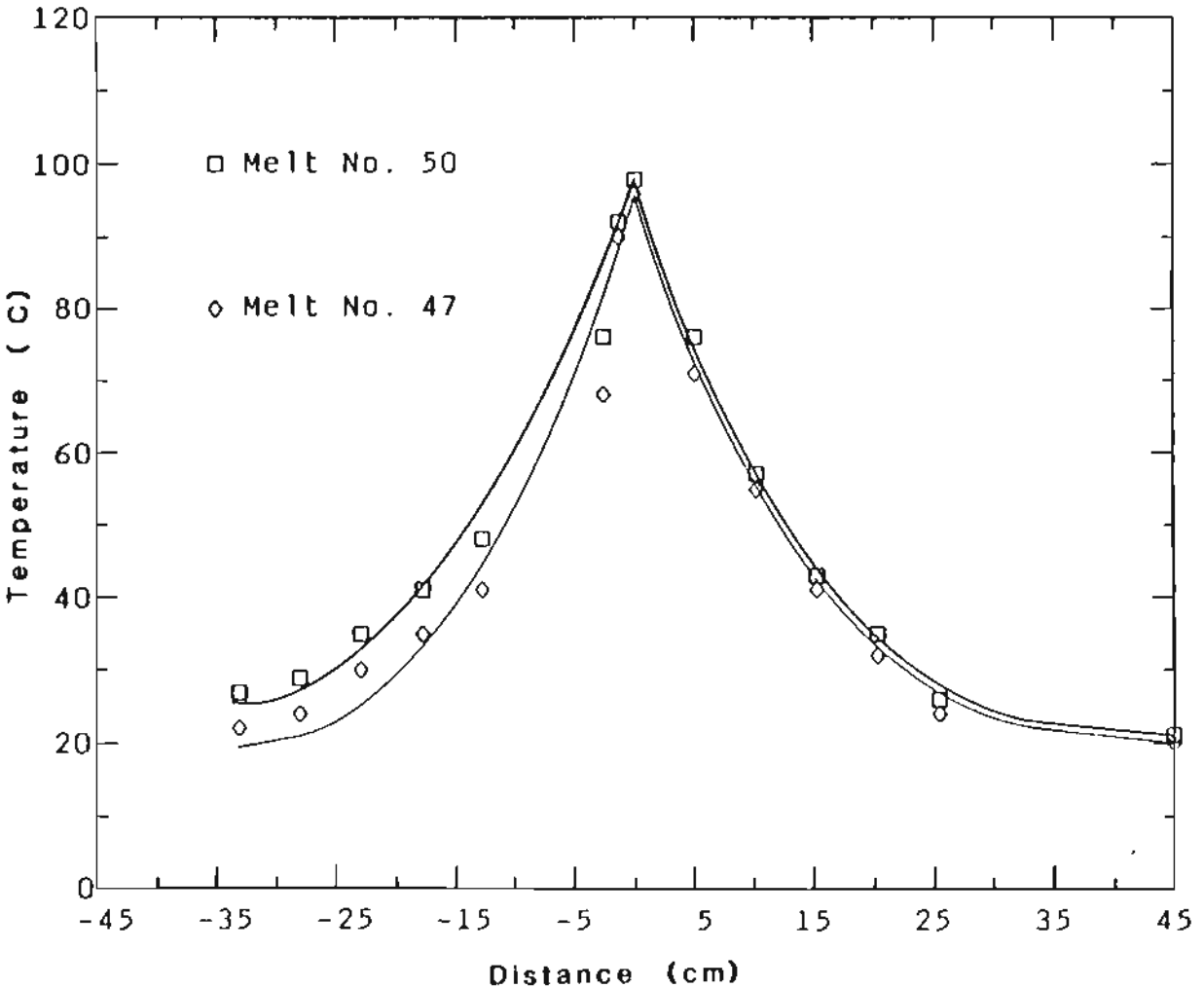

Figure 5.31. Quasi-steady temperature distribution on the crucible wall for melts with no gas cooling and with gas cooling.

the first thermocouple just below the pool (1.25 cm from thermocouple number 9) is close to the peak temperature, indicating that the solidified layer of the ingot is in contact with the crucible. The temperature of the second thermocouple below the pool, which is at 2.5 cm below the pool position (thermocouple number 9), is considerably lower for melt 47, indicating that the solidified ingot has pulled away from the crucible, forming a shrinkage gap between the crucible and the ingot. Heat transfer in this case is only by radiation. For melt number 50, the temperature of the same thermocouple is higher indicating that the helium gas cooling has improved the heat transfer from the ingot to the crucible. The temperature of all the thermocouples below this location are higher with helium gas cooling as compared to no gas cooling. This further confirms the observation of the effect of gas cooling. With a gas between the ingot and the crucible, the heat transfer is by radiation and gas conduction. The total heat flux is the sum of heat flux due to radiation and heat flux due to gas conduction leading to increased heat transfer between the ingot and crucible.

Cliff and Dain (43) have used computer modeling to predict the effect of various operating parameters on the heat transfer coefficients and crucible inside temperature during continuous casting. One of the parameters studied was the effect of injection of hydrogen gas in the gap between the ingot and crucible. The rate of heat extraction was found to improve substantially with hydrogen gas injection. The inside crucible temperature at the molten metal pool meniscus was also very high. They reported a crucible temperature of 886°C at the meniscus of the pool with hydrogen gas as compared to 261°C without hydrogen gas cooling. There is, unfortunately no mention of the hydrogen gas pressure used in

the computer calculation, and it is quite probable, they have used 760 mm pressure. There are also no experimental results to verify the computer calculated data. As discussed earlier, in the present investigation, no significant differences in the peak temperature of the thermocouples were observed for the case with no gas cooling and gas cooling. This directly contradicts the findings of Cliff and Dain. Further conclusions could not be drawn as there are no other details are given in the published literature (43). Soviet investigators have reported (45) a slight decrease in the peak heat flux on the crucible wall with helium gas cooling in VAR.

Figure 5.32 shows the variation of temperature of a single thermocouple as a function of time for the melts with helium gas cooling and without helium gas cooling. The particular thermocouple selected was thermocouple number 2, which is at 5 cm from the bottom of the crucible. It can be seen from the plot that, the temperature of the thermocouple is the same for both the melts (with and without gas cooling), till the molten metal pool passes the position of thermocouple number 2. After that, the temperatures of the thermocouple are consistently higher for the melt made with helium gas cooling. Again, there is no difference in the peak temperature with gas cooling and without gas cooling. After about 30 minutes, the temperature difference of thermocouple number 2, with gas cooling and without gas cooling decreases. This indicates the decrease in heat transfer coefficient between the ingot and crucible.

One melt (melt number 53) was made with argon gas between the ingot and the crucible. This melt was made to compare the effectiveness of argon cooling versus helium cooling. The gas pressure used for comparison was 60 mm

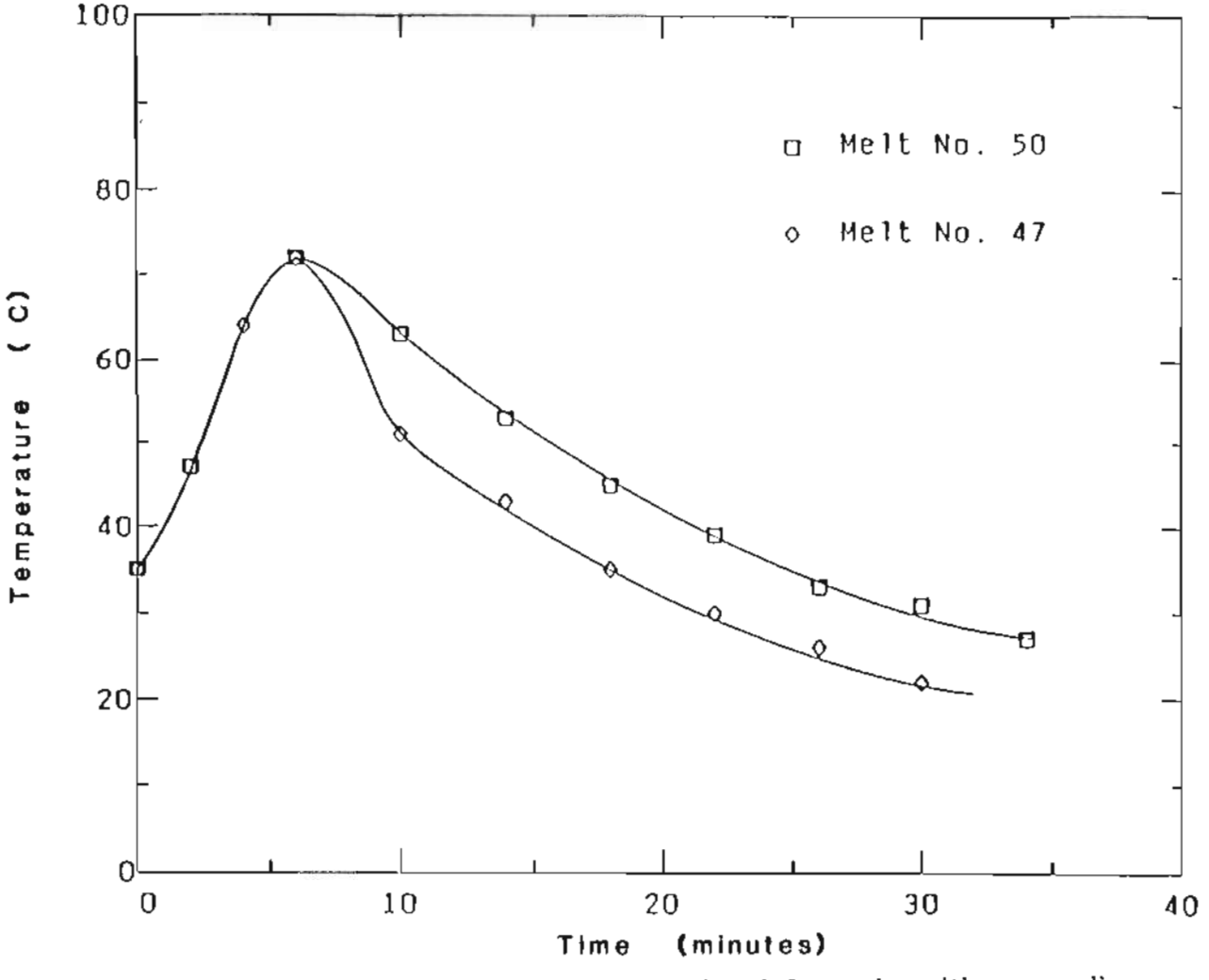

Figure 5.32. Temperature of thermocouple number 2 for melts with gas cooling and no gas cooling.

Hg. Figure 5.33 shows the temperature distribution on the crucible wall for melt number 50 with 60 mm of helium gas pressure and for melt number 53 with 60 mm of argon gas pressure. It can be seen that the temperature of the thermocouples below the pool are higher for the case of helium gas cooling as compared to argon gas cooling, as expected due to the higher thermal conductivity of helium gas. Again, for the two melts, there is no difference in the peak temperature distribution on the crucible wall above the pool.

The inlet and outlet cooling water temperatures of the copper crucible were recorded during the melting process. The increase in water temperature with helium gas cooling and without helium gas cooling is plotted as a function of the melting time in Figure 5.34. Helium gas was introduced after about 5 minutes from the start of the melt for melt number 50. It can be seen that after helium gas was introduced the increase in water temperature was higher for the case with helium gas cooling as expected.

5.2.2.2. Heat Flux On Crucible Wall

In order to compute the distribution of the heat flux on the crucible wall, a combination of experimentally measured temperatures on the crucible wall and empirically determined heat transfer coefficients was used. Also, the total heat flux extracted by the cooling water is known as the water flow rate and rise in the water temperature were measured throughout the melting period. The technique used by Bertram and Zanner (15) is utilized in the heat flux analysis. The total heat flux removed by the cooling water is given by,

$$H.F_{H_2O} = \dot{m}_{H_2O} c_p (T_{out} - T_{in}) \tag{5.64}$$

where,

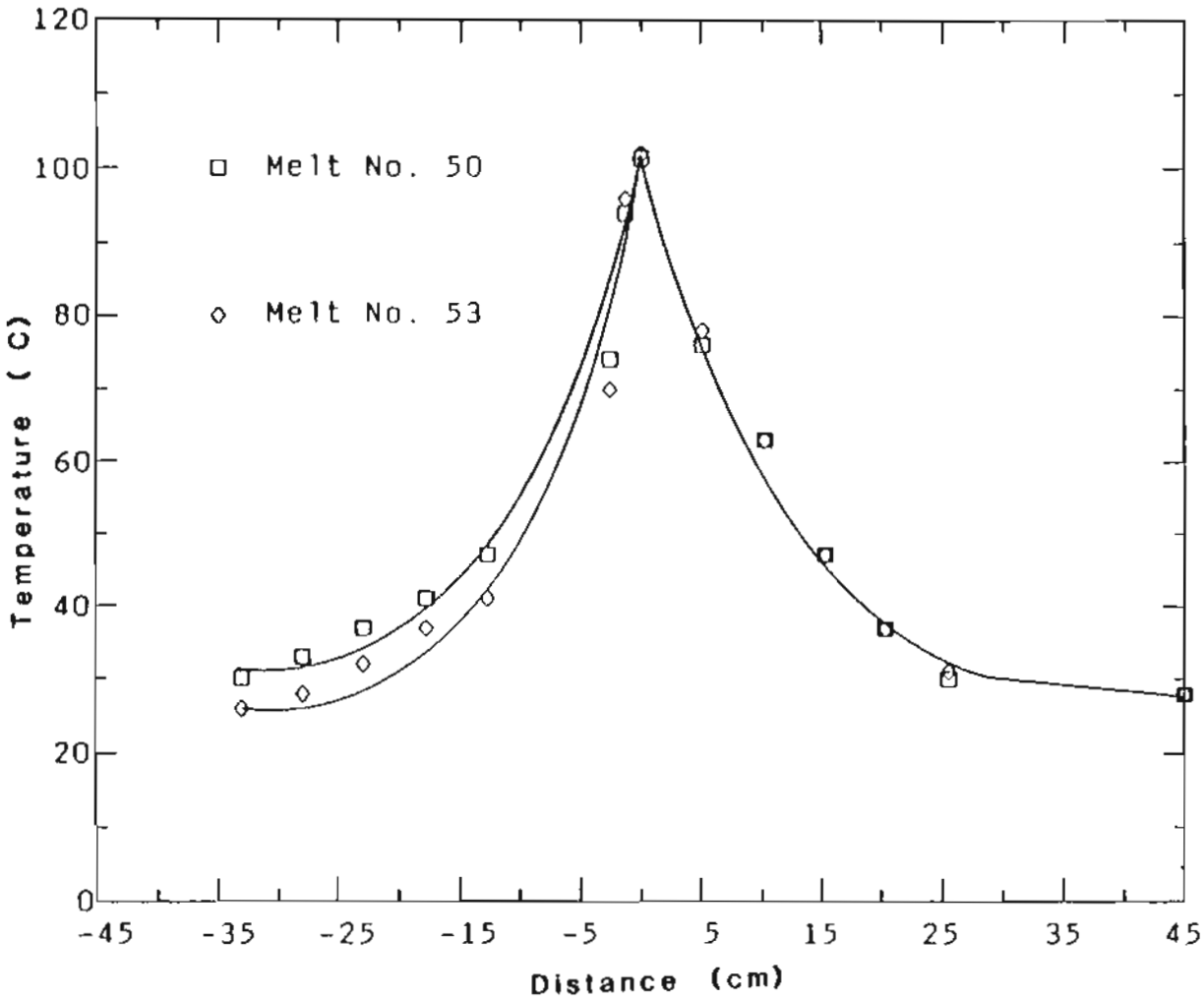

Figure 5.33. Quasi-steady temperature distribution on the crucible wall for melt 50 (helium 60 mm Hg) and for melt 53 (argon 60 mm Hg).

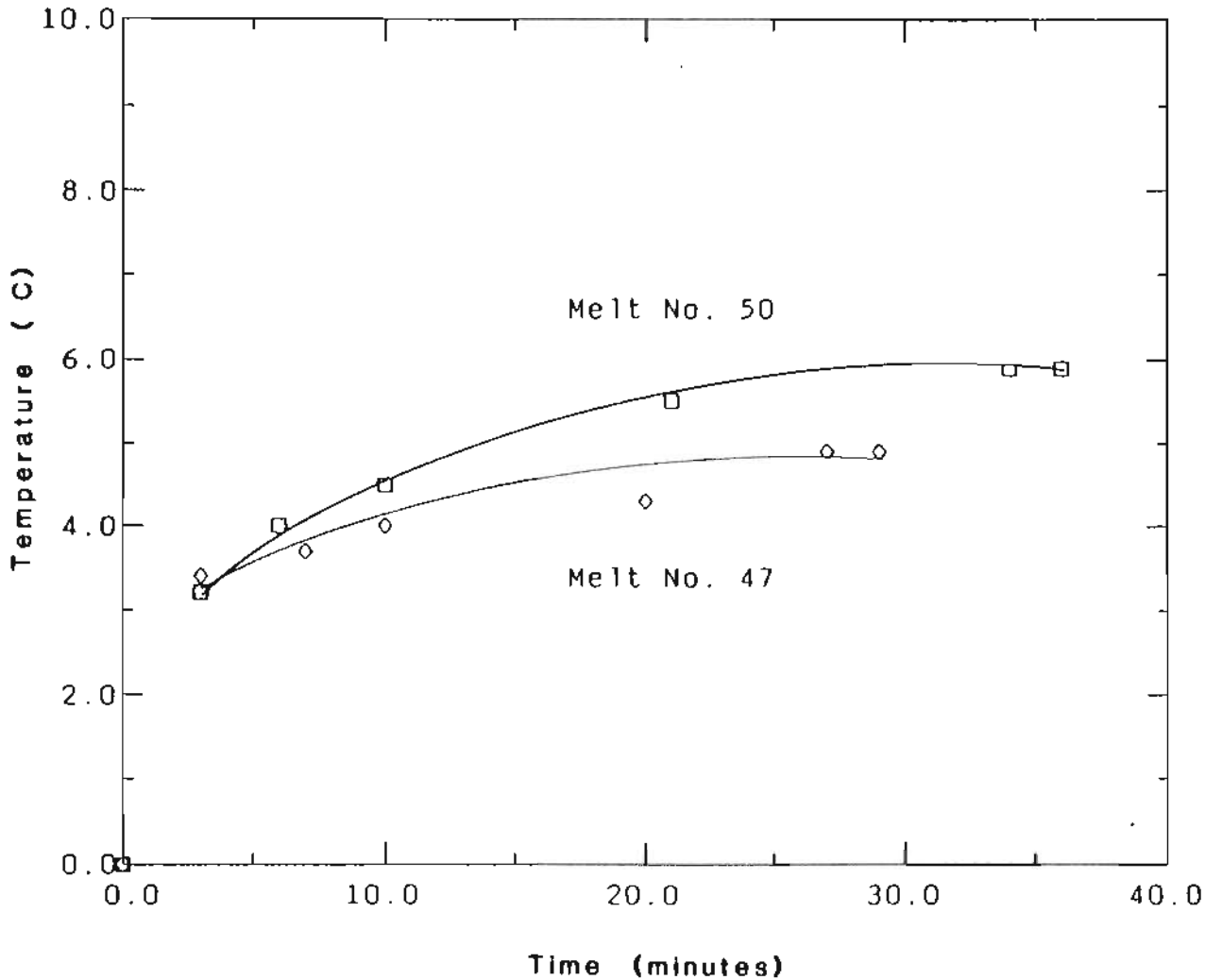

Figure 5.34. Crucible cooling water raise as a function of melt time for melt 47 (no gas) and melt 50 (60 mm helium).

$H.F_{H_2O}$ = heat flux extracted by water

$\dot{m}_{H_2O}$ = average water flow rate

c_p = specific heat at constant pressure

T_{out} = outlet temperature of crucible water

T_{in} = inlet temperature of the crucible water

The heat flux distribution on the crucible wall is given by,

$$H.F(x)=h_c\,(T(x)-T_{bulkH_2O}) \tag{5.65}$$

where,

H.F(x) = heat flux on the crucible wall

h_c = convective heat transfer coefficient on crucible wall

T (x) = measured crucible wall temperature

T_{bulkH_2O} = average bulk water temperature.

It should be noted that measured temperature of the crucible varied in the range of 20 to 100°C . It is necessary to take into account the variation of heat transfer coefficient with temperature. Thus the expression 5.59 is modified as,

$$H.F(x)=h_c(T)\,(T(x)-T_{bulkH_2O}) \tag{5.66}$$

The total heat flux on the crucible wall can now be determined by integrating the above expression over the length of the crucible. Thus,

$$H.F_{wall} = 2\pi r\int_{x_1}^{x_2} h_c(T)(T(x)-T_{bulkH_2O})dx \tag{5.67}$$

where,

$x_2 - x_1$ = length of the crucible

r = outer radius of the crucible

Since the heat transfer coefficient is empirically calculated, to take into account the hydrodynamic conditions, one can write,

$$h_c(T) = \beta h_c(T) \tag{5.68}$$

Substituting this into the above equation, one can get,

$$H.F_{wall} = 2\pi r \int_{x_1}^{x_2} \beta h_c(T)(T(x) - T_{bulkH_2O})dx \tag{5.69}$$

During quasi-steady state, the heat flux in the crucible wall must be equal to the heat flux removed by the cooling water. Thus equating expressions 5.64 and 5.69,

$$\beta 2\pi r \int_{x_1}^{x_2} h_c(T)(T(x) - T_{bulkH_2O})dx = \dot{m}_{H_2O} C_p (T_{out} - T_{in}) \tag{5.70}$$

From the above expression, it is now possible to calculate the actual heat transfer coefficient or the heat flux along the length of the crucible which could be used as a boundary condition for computer simulation of VAR process.

Calculation of Heat Transfer Coefficient

On examining the temperature distribution of the crucible wall, it is clear that the temperature on the outside of crucible does not exceed the boiling point of water. Hence the non-boiling heat transfer conditions are considered in the present analysis. In order to calculate the heat transfer coefficient, one need to determine the water flow regime. This is dependent on Reynolds Number, given by,

$$\text{Reynolds Number} = \frac{GD_H}{\mu} \tag{5.71}$$

where,

G = mass velocity of the fluid flowing through the annulus in $kg/sec/m^2$

$= \rho V$

D_H = hydraulic diameter

μ = coefficient of viscosity

ρ = density of water = 1000 kg/m^3

V = velocity of water in m^3 /second

Following are the experimental data used in the calculation.

Water flow rate = 50 GPM = $3.154\times10^{-3} m^3/sec$

D_2 = Diameter of the water guide tube (inner) = 0.229 m

D_1 = Diameter of the crucible (outer) = 0.190 m

Thus, area of annulus $= \frac{\pi}{4}(D_2^2 - D_1^2) = 0.0128\ m^2$

and,

$$\text{Velocity} = V = \frac{3.154\times10^{-3}}{0.0128} = 0.246\ m/sec$$

Mass Velocity = $G = 1000\times0.246 = 246 kg/m^2 sec$

$$D_H = \text{Hydraulic Diameter in meters} = 4\frac{\text{Annulus Area}}{\text{Wetted Perimeter}} = D_2 - D_1$$

$= 0.039$ m

μ = coefficient of viscosity for water = $658\times10^{-6} kg/m/sec$ at $40^\circ C$

Substituting in 5.71,

$$Re = \frac{246\times0.039}{658\times10^{-6}} = 13458$$

The flow is laminar when the Reynolds number is below 2100 (73). In the range of Reynolds number between 2100 and 10000, we have a transition from laminar to turbulent flow. The flow in this regime is called 'Transitional'. At a Reynolds number greater than 10000, the flow becomes fully turbulent. Thus, the experimental water flow rate is in the 'turbulent ' region.

Colburn (73) has developed an equation for heat transfer coefficient for turbulent flow in an annular tube, which is given by,

$$St.(Pr)^{\frac{2}{3}} = 0.023(Re)^{-0.2} \tag{5.72}$$

where,

$$St = \text{Stanton Number} = \frac{h_c}{c_p G}$$

$$Re = \text{Reynolds Number} = \frac{GD_H}{\mu}$$

$$Pr = \text{Prandtl Number} = \frac{\mu c_p}{k}$$

k = thermal conductivity of the fluid

h_c = heat transfer coefficient

The meaning of all the other terms has been explained earlier.

In order to account for the variation in physical properties due to temperature gradients, McAdams (73) recommended that all the physical properties should be evaluated at the average film temperature of the fluid. This average temperature is defined as :

$$T_f = 0.5(T_s - T_b) \tag{5.73}$$

where,

T_s = surface temperature of the crucible in°C

T_b = bulk water temperature = $\frac{1}{2}(T_{inlet}+T_{outlet})$

T_{inlet} = inlet water temperature

T_{outlet} = outlet water temperature

In the present case both T_s and T_b are variables, hence, a computer program was written to calculate the heat transfer coefficient along the length of the crucible. A sample calculation for heat transfer coefficient at 40°C is shown below. Note that following physical properties of water were used.

c_p = 4182 J/kg K

k = 0.633 W/m K

$\mu = 658\times10^{-6}$ kg/m/sec

The values of G and D_H have been calculated earlier to be 246 kg/m^2 sec and 0.039 m respectively. Using Colburn's equation (73),

$$St = \frac{h}{C_p G} = 0.023 Re^{-0.2} Pr^{-\frac{2}{3}} \qquad (5.74)$$

Substituting all the above values in the above equation and simplifying, one can get :

$$h = 1329.5 \text{ W/m}^2\text{K}$$

Figure 5.35 shows the variation of heat transfer coefficient with temperature. There is a linear relationship between the two parameters.

After calculating the heat transfer coefficient, the heat flux on the crucible wall was calculated from the expression 5.67 using the experimentally measured

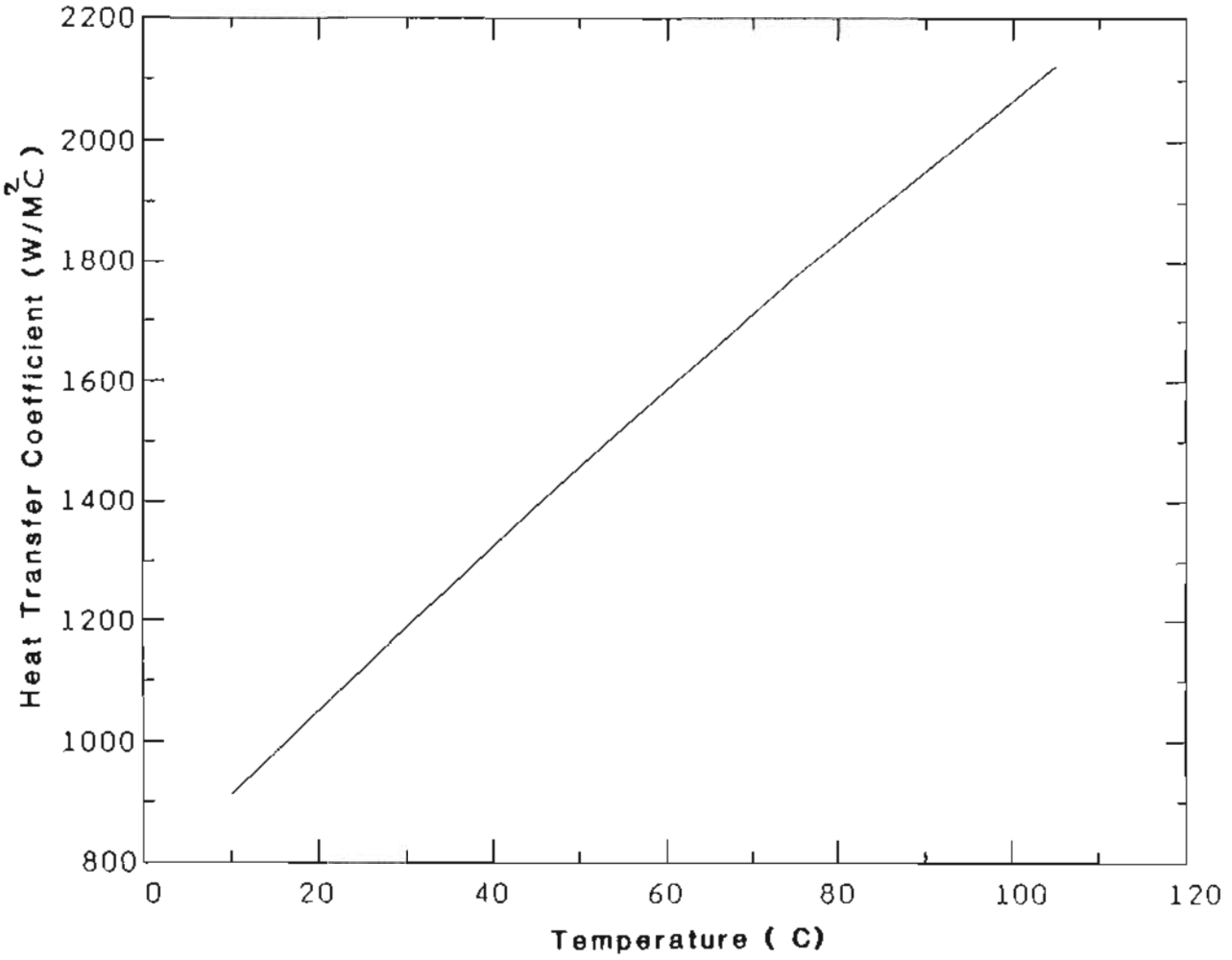

Figure 5.35. Convective heat transfer coefficient as a function of temperature.

temperature distribution on the crucible wall and bulk water temperature. The expression is given below.

$$H.F_{wall} = 2\pi r \int_{x_1}^{x_2} h_c(T)(T(x) - T_{bulkH_2O})dx \qquad (5.75)$$

A computer program was written to compute the heat flux on the crucible. The algorithm of the computer program for computing the heat flux on the crucible is given in Figure 5.36. First the heat transfer coefficient is calculated along the length of the crucible, using the measured temperature profile on the crucible wall and the bulk water temperature. Then the heat flux is computed using QUANC8 Subroutine available in the department's Computer Library. QUANC-8 is a subroutine for integrating a function using the Newton-Cotes method.

A typical calculation for melt number 47 is provided below. The experimentally obtained temperature profile on the crucible for melt number 47 is given in Figure 5.30. The experimental details and the calculations are as follows.

Power = 75 KW

Water Flow Rate = $3.15 \times 10^{-3} m^3/sec$

Water Inlet Temperature = $14.1^{\circ}C$

Water Outlet Temperature = $19.0^{\circ}C$

$\Delta T_{water} = 4.9^{\circ}C$

Heat removed by cooling water = $\dot{m} c_p \Delta T$

$= 3.15 \times 10^{-3} \times 999.2 \times 4.187 \times 4.9 = 64.6$ KW

$$\text{Percentage heat removed by water} = \frac{\text{total heat removed by water}}{\text{total heat input}}$$

$$= \frac{64.6}{75} \times 100 = 86\ \%$$

Thus from above, 86 % of the heat input is removed by the cooling water while 14 % remains as sensible heat in the ingot.

The computer calculated heat flux on the crucible wall (using the experimentally measured temperatures profile) is given in Table 5.11. The heat flux removed by water and the percentage heat removed are given in Table 5.12.

The % heat removed by cooling water with no gas between the ingot and crucible was about 86%, and with 60 mm of helium gas pressure, the % heat removed was 103%. With 60 mm of argon gas pressure, the % heat removed was about 96.6%.

The distribution of heat flux on the crucible wall for melt number 47 (with no gas cooling) is shown in Figure 5.37. The maximum heat flux on the crucible surface was about 36.5 W/cm^2. Figure 5.38 shows the heat flux on the crucible wall for melt with helium gas cooling and no gas cooling. Again, here '-' indicates below the pool and '+' indicates above the pool. It can be seen that there is a significant difference in the heat flux below the pool for these two melts. For the melt with helium gas cooling, the heat flux values below the pool are higher than those without gas cooling. There is no difference in the peak heat flux for the two melts. Also, there seems to be some difference in the heat flux above the pool. For melts made with gas cooling between the ingot and crucible, the crown height was higher as compared to the melt with no gas cooling. In all the melts, the electrode gap and the other melting parameters were kept constant except gas cooling. The longer crown height might be the cause for a

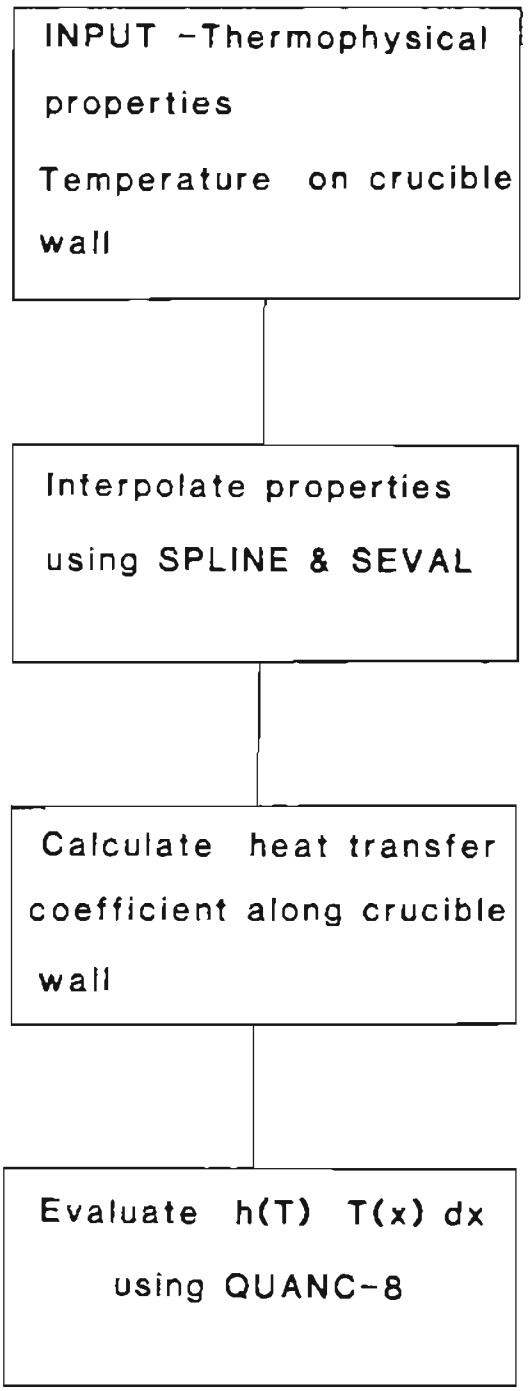

Figure 5.36. Algoritham for computing heat flux on the crucible wall.

TABLE 5.11

COMPUTER CALCULATED HEAT FLUX ON CRUCIBLE WALL FOR MELT NO. 47

Distance from bottom (M)	Measured Temperature (O C)	Heat Transfer Coeff. (W/ m^2 C)	Heat flux W/ m^2
0.00	22.0	1043.0	5217
0.051	24.0	1057.4	7401
0.102	32.0	1113.0	16696
0.152	35.0	1133.0	20409
0.203	41.0	1175.0	28200
0.254	58.0	1290.0	52913
0.317	90.0	1502.0	109678
0.330	96.0	1541.	121755
0.381	71.0	1377.0	74393
0.432	55.0	1270.0	48271
0.482	39.0	1161.0	25548
0.533	32.0	1113.0	16696
0.584	24.0	1057.0	7401
0.635	24.0	1057.0	7401
1.020	20.0	1029.0	3088

TABLE 5.12

HEAT TRANSFER PARTICULARS OF INCONEL 718 MELTS

Melt No.	Gas Pressure (mm)	ΔT water (o C)	H.F. Flux removed (KW)	Heat removed %
47	0	4.9	64.6	86
49	40	5.7	75.11	100
50	60	5.9	77.75	103.6
53	60(Ar)	5.5	72.5	96.6

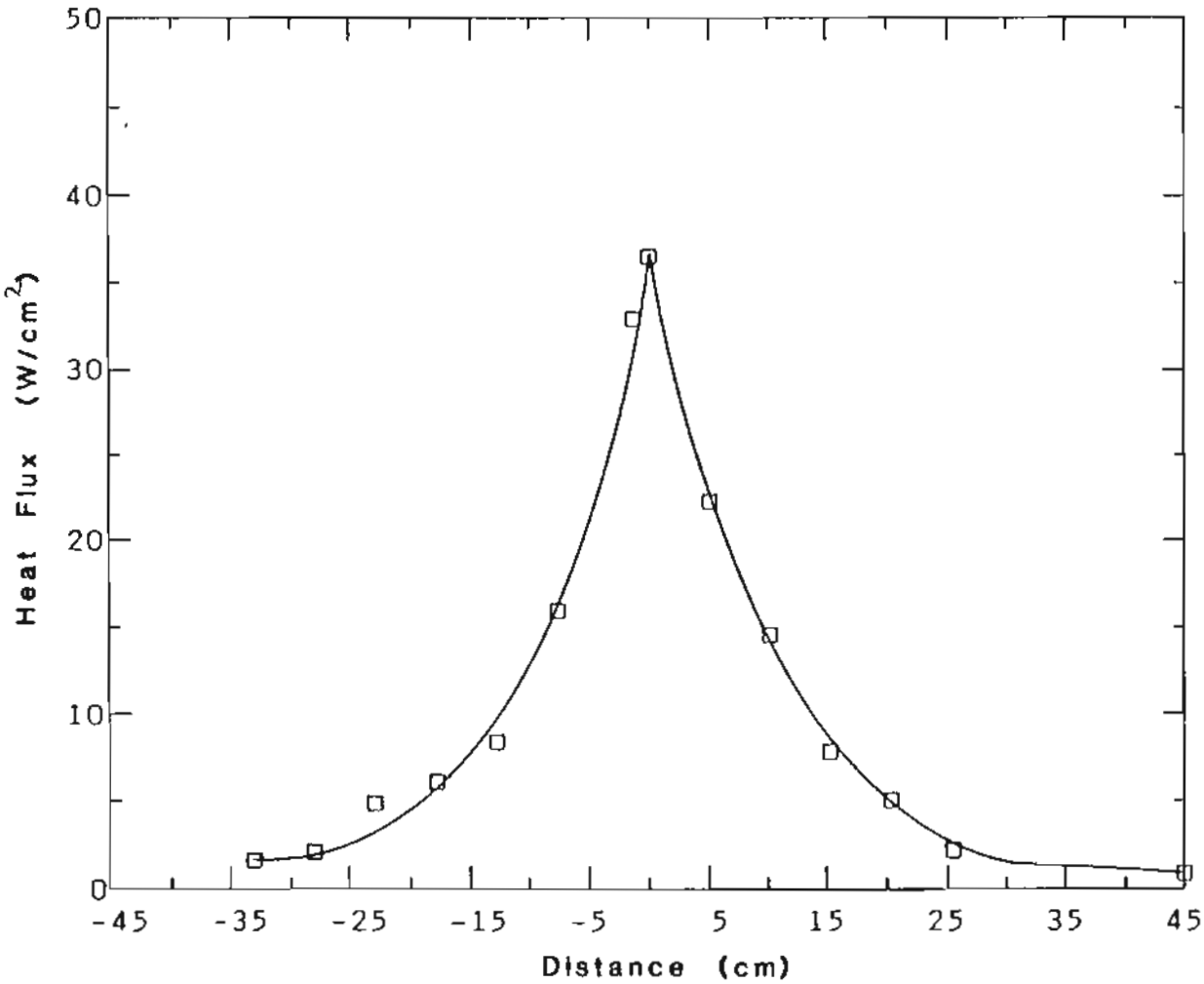

Figure 5.37. Distribution of heat flux on crucible wall for melt number 47 (no gas).

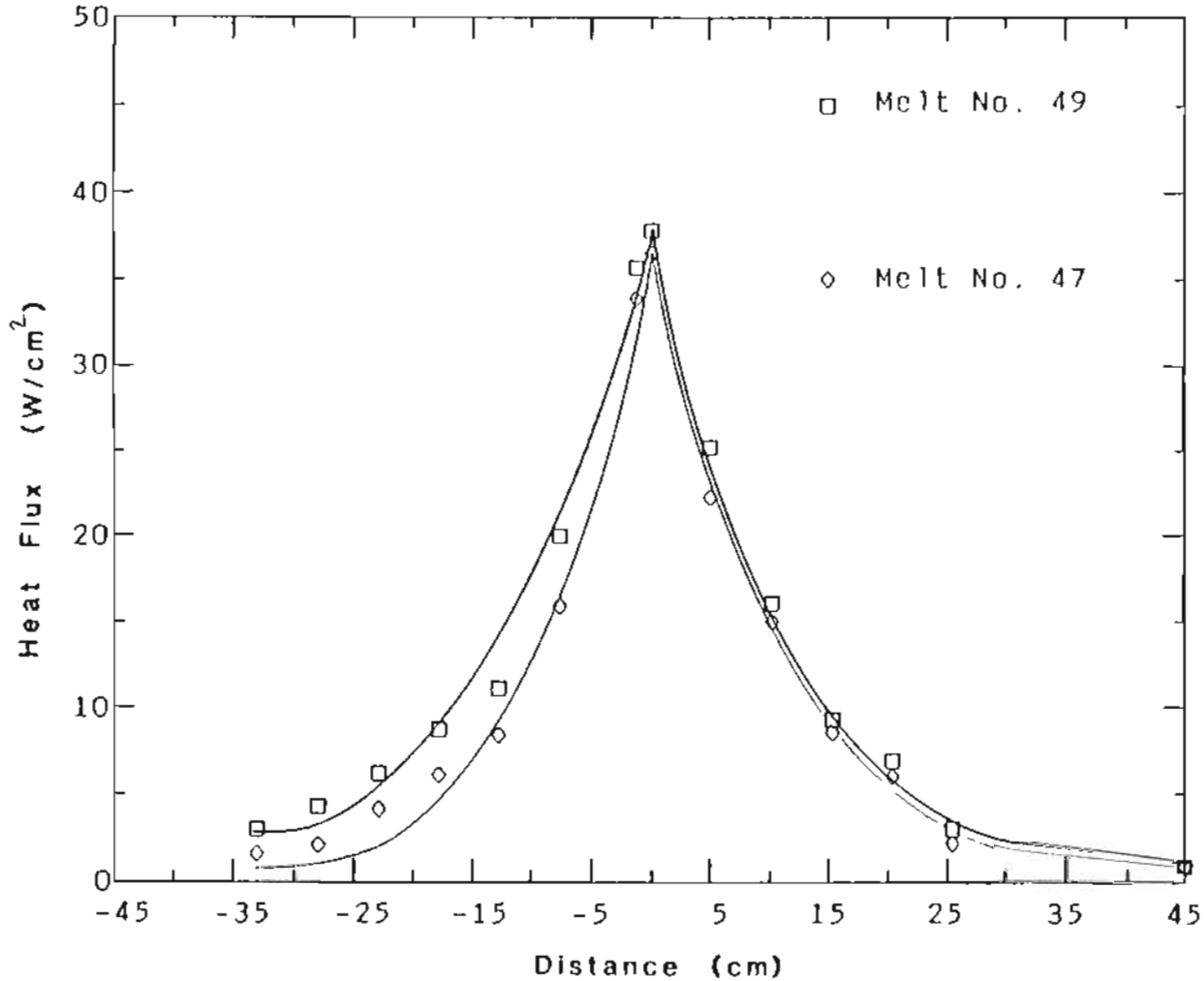

Figure 5.38. Distribution of heat flux on crucible wall for melt number 47 (no gas) and 49 (40 mm helium).

slight higher heat flux on the crucible wall.

5.2.2.3. Molten Metal Pool Depth

The discussion on heat extraction rate in the previous sections, has shown that 17% more heat could be extracted by cooling water with 60 mm helium gas between the ingot and crucible. This increased heat extraction rate should result in a corresponding decrease in molten metal pool depth, mushy zone size and segregation. Figure 5.39 - 5.41 show the photographs of the molten metal pool for the case of no gas cooling and helium gas cooling at various pressures. Figure 5.42 shows a comparison of metal pool depths under various cooling conditions. The molten metal pool depth for the case of no gas cooling was found to be 20 cm and with 60 mm helium gas cooling , it was 12.7 cm, i.e. about 36% decrease in metal pool depth which is very significant. It can also be seen that with gas cooling the metal pool profile became cup shaped rather than conical shaped. As discussed earlier, the size and shape of the molten metal pool is the result of the rate of heat input in to the metal pool, the rate of heat extraction from the ingot and various losses. With the helium gas cooling between the ingot and crucible, more heat was extracted from the ingot resulting in a shallower metal pool.

5.2.2.4. Surface Quality of the Ingot

Figure 5.43 shows the surface condition of the ingot number 50. This ingot was made under helium gas cooling conditions (60 mm Hg). It can be seen that the surface quality of the lower most part of the ingot is much smoother as compared to rest of the ingot. This is because helium gas was introduced after a few centimeters of the ingot was solidified and smoother surface at the bottom of the

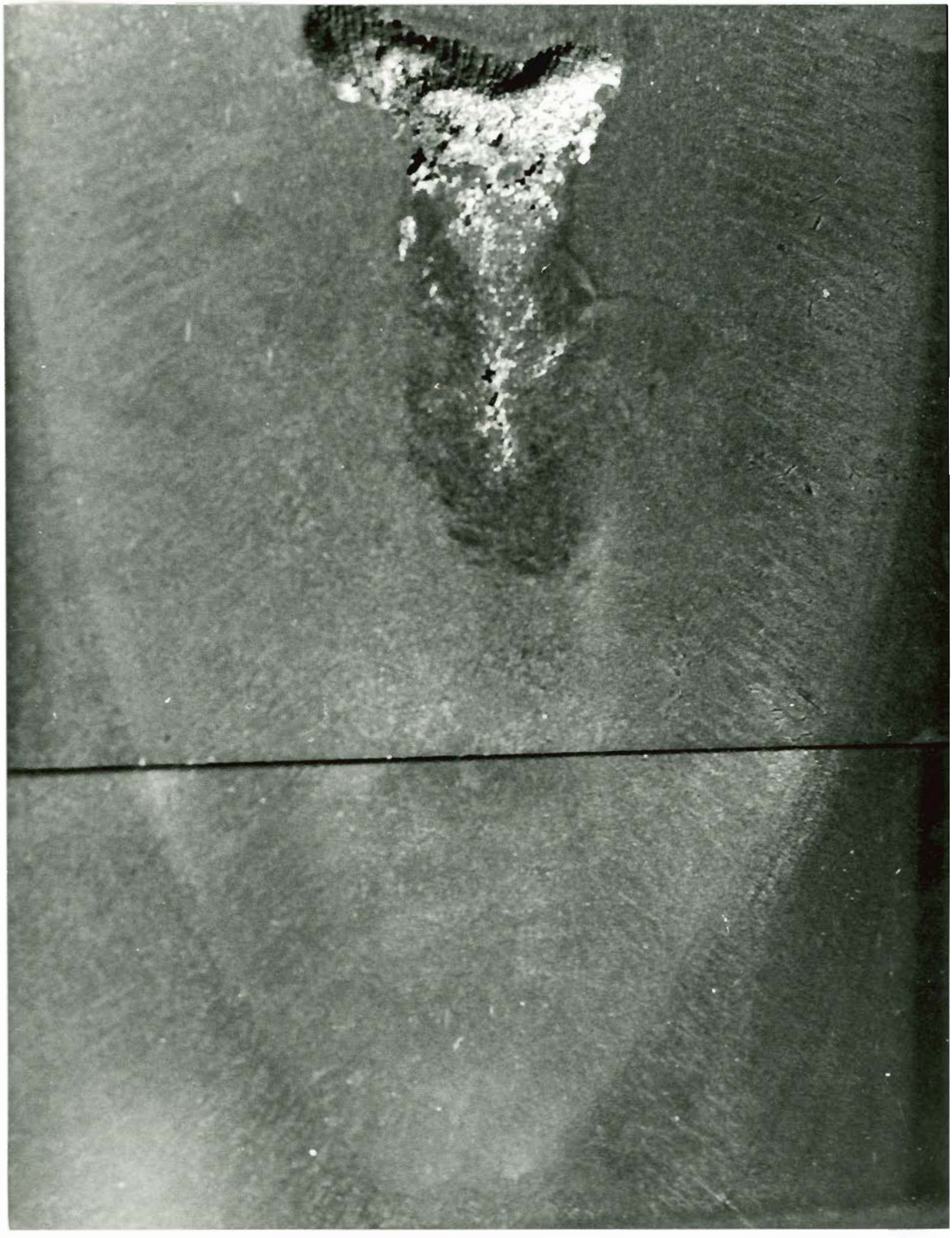

Figure 5.39. Molten metal pool profile for melt number 47 (no gas cooling). Scale 1:1.

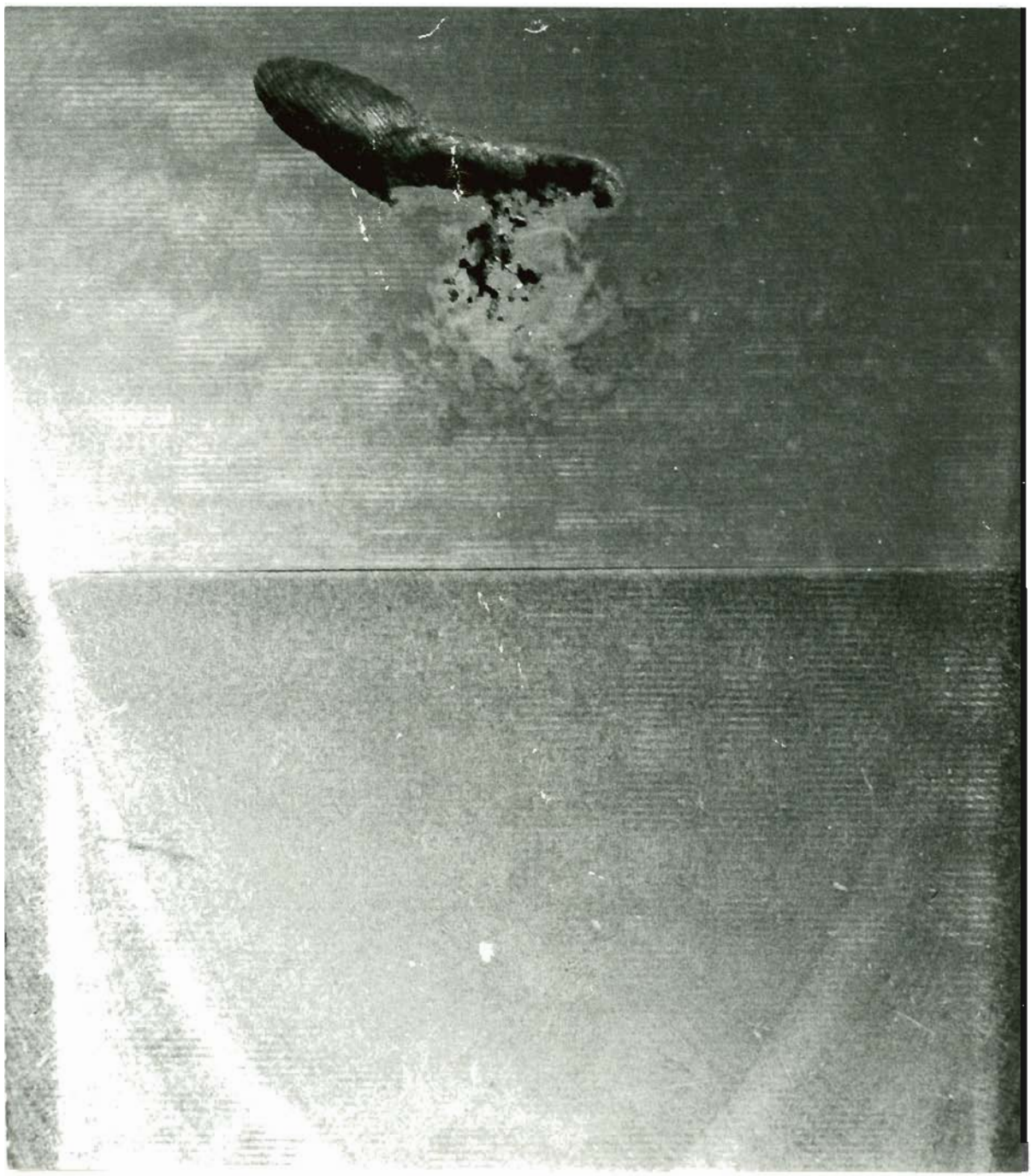

Figure 5.40. Molten metal pool profile for melt number 49 (40 mm Hg helium gas). Scale 1:1.

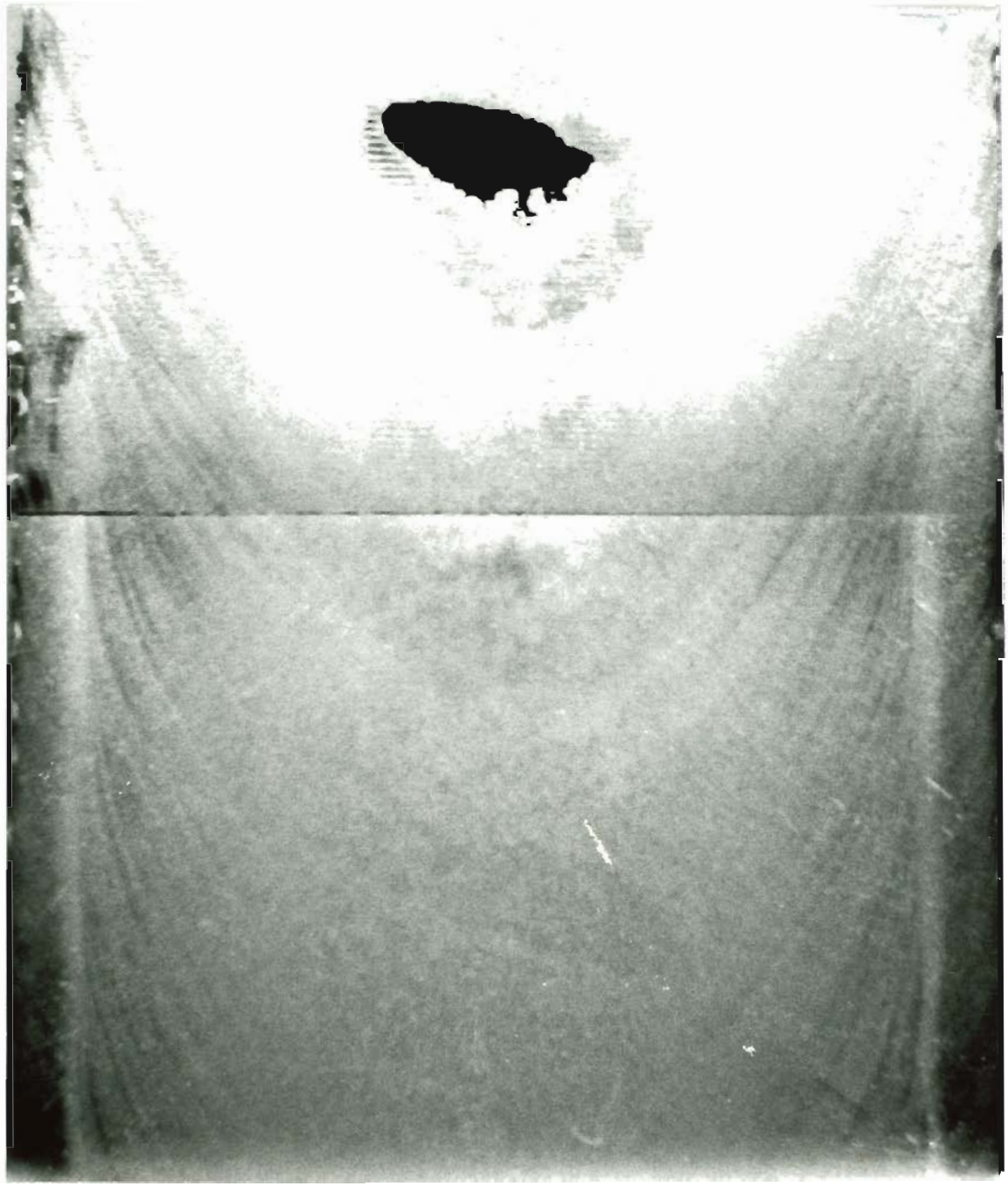

Figure 5.41. Molten metal pool profile for melt number 50 (60 mm Hg helium gas). Scale 1:1.

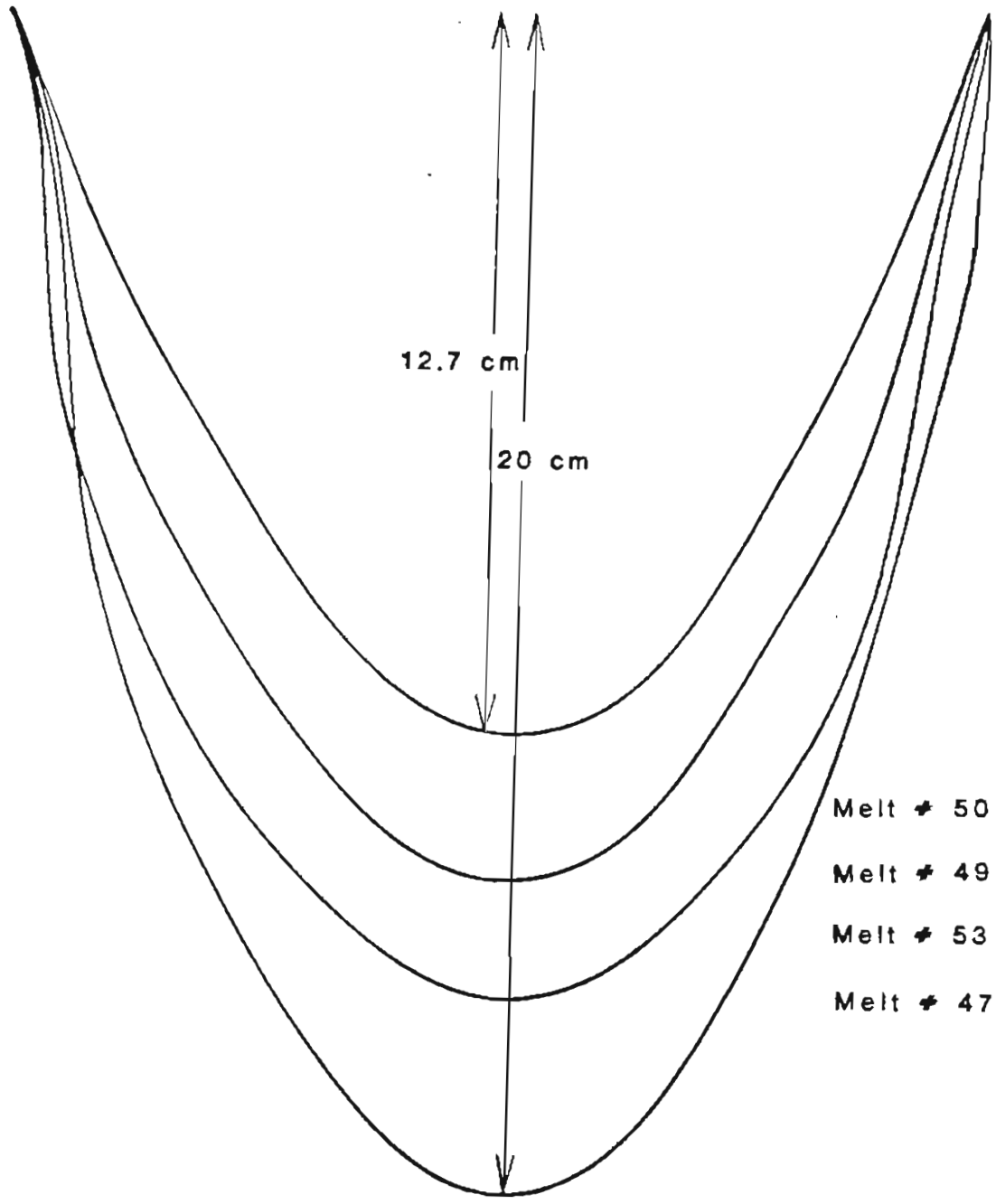

Figure 5.42. Comparison of molten metal pool depths under various cooling conditions.

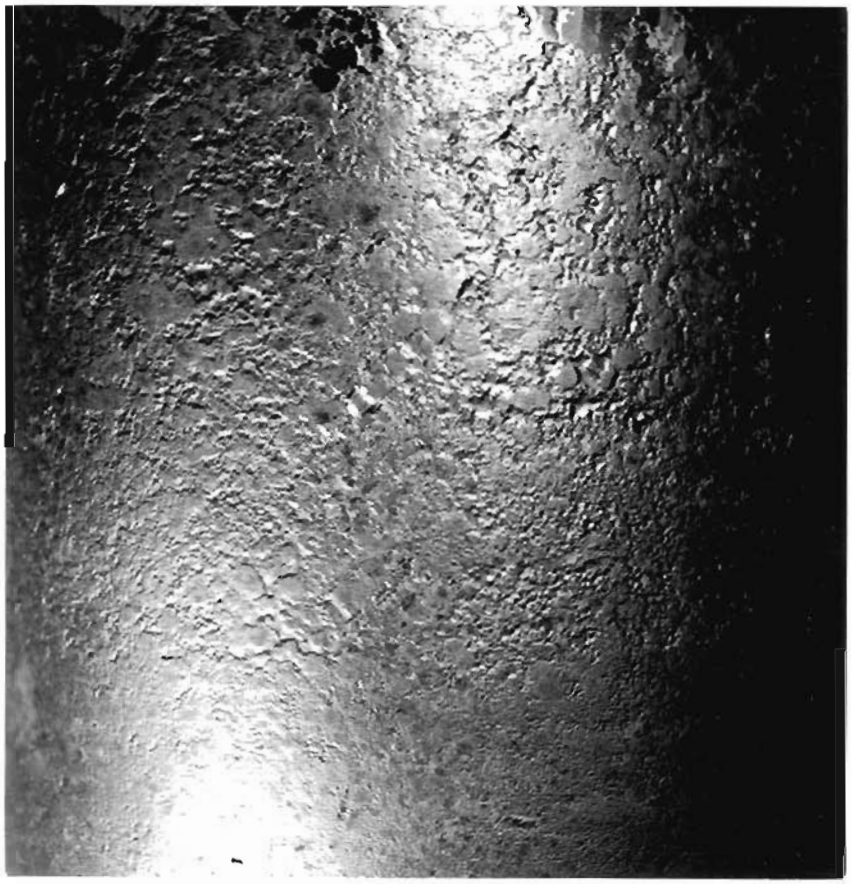

Figure 5.43. Surface condition of ingot number 50 (60 mm Hg helium). Scale 1:0.75

ingot corresponds to no gas cooling. Figure 5.44 shows a comparison of surface condition of the ingot with gas cooling and without gas cooling. The surface of ingot number 47 is smoother as compared to surface of the ingot number 49 which was done with 40 mm of helium gas cooling. Hence, the surface quality of the ingot deteriorated with gas cooling. This may be due to the combined effect of two factors. The first may be due to increased splatter deposition on the crucible inside wall for a gas cooled ingot. The second factor might be connected with the higher ingot growth rate for gas cooled ingot. Both of these might have resulted in only partial remelting of the splatter, producing a rough surface. During the melting process metal pool was observed through the viewing port for any disturbances if any, occurring with gas cooling. Also the whole melting cycle was videotaped. The metal bath seemed to be calm during melting with gas cooling and no bubbling action was observed. Also the increase in pressure in the melting zone with gas cooling was only a few microns more (9 microns) as compared to no gas cooling. The ingots were cut and found to be sound.

5.2.2.5. Grain Growth Pattern

Figure 5.45 shows the photographs of the macro-etched sections of the ingots made without gas cooling and with gas cooling. The grain growth angles were measured from the photographs. The grain growth angle refers to the angle between the grain growth direction and the longitudinal direction. The angles were found to be about 48° , 44° and 42° at the center of the ingots for melt numbers 47, 49 and 50 respectively. The melt number 47 had the deepest pool and melt number 50 had the shallower pool. As the depth of the metal pool increases, the grain growth angle increases. With helium gas cooling, the heat

a) Without gas cooling

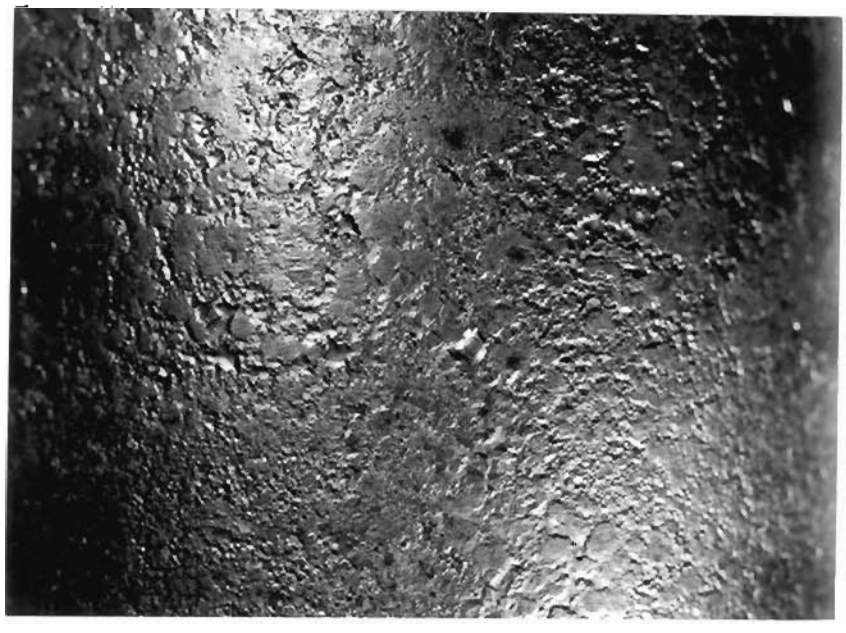

b) with gas coolng (40 mm Hg helium)

Figure 5.44. Comparison of surface condition of ingots. Scale 1:0.75

a) With no gas cooling

b) with 40 mm Hg helium gas cooling

c) with 60 mm Hg helium gas cooling

Figure 5.45. Photographs of macroetched sections of Inconel 718 melts.

extraction rate was increased resulting in a shallower metal pool and this resulted in a decreased grain growth angle. Ideally, an axially oriented grain growth pattern is preferred. Under this condition, the metal pool is almost flat and tendency for segregation is less.

5.2.2.6. Dendrite Arm Spacing

Dendrite arm spacing measurements provide an estimation of the local cooling rates in the ingot and also can be used to determine the mushy zone sizes (as there are no direct means of determining the mushy zone sizes). One of the objectives of the present investigation was to see whether helium gas cooling had any effect on dendrite arm spacing especially at the center of the ingot. Dendrite arm spacing measurements were made at the edge, mid radius and center of each ingot just below the molten metal pool. A minimum of twenty five measurements were made on each sample from several photomicrographs. Figure 5.46 shows a colored photomicrographs of dendritic structure. Figure 5.47 to 5.49 show the photomicrographs of dendritic structure at the center, mid radius and edge of the ingot under various gas cooling conditions. Table 5.13 presents the measured secondary dendrite arm spacings. It can be seen that, the dendrite arm spacing increases from edge to center of the ingot as expected. The cooling rate is highest at the edge of the ingot and lowest at the center of the ingot. The dendritic structure became finer with increased helium gas pressure at the edge as well as at the center of the ingot. In fact, for cases of helium gas cooling using 40 mm and 60 mm helium gas, the dendrites at the center were finer than those measured on the edge of ingot number 47 (no gas cooling). This implied that the cooling rate at the center of all gas cooled ingots (ingot numbers 49, 50 and

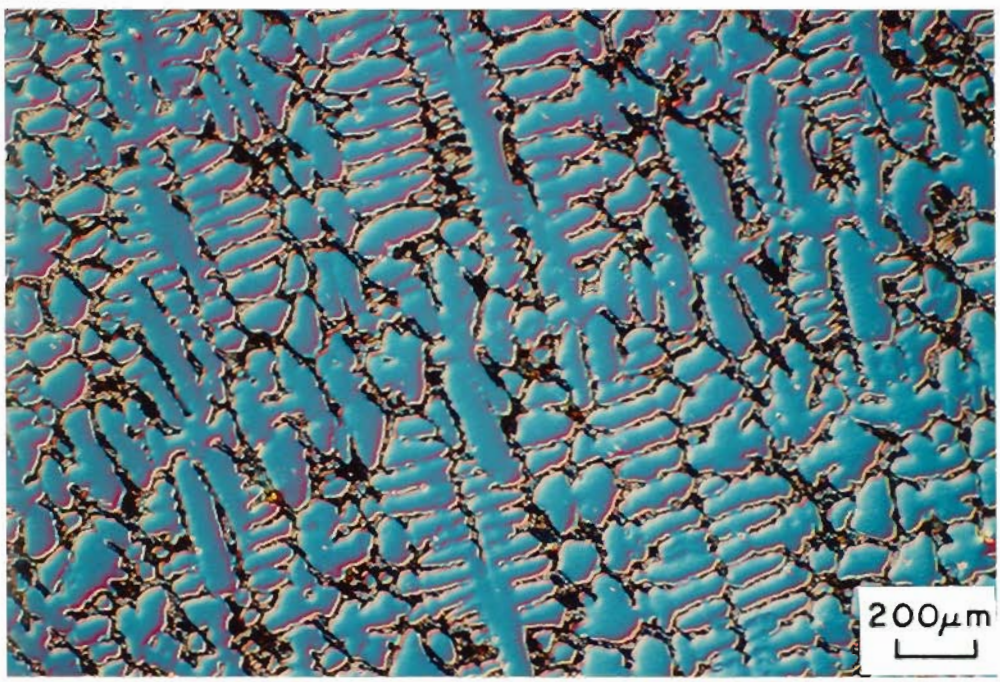

Figure 5.46. Coloured photomicrograph of dendritic structure.

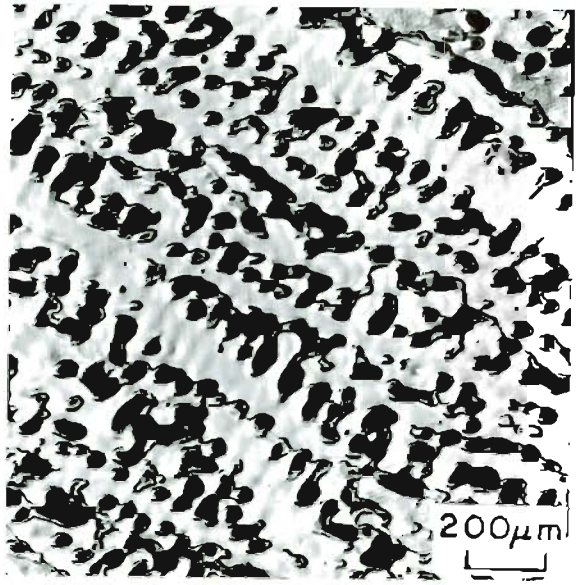

a) Edge

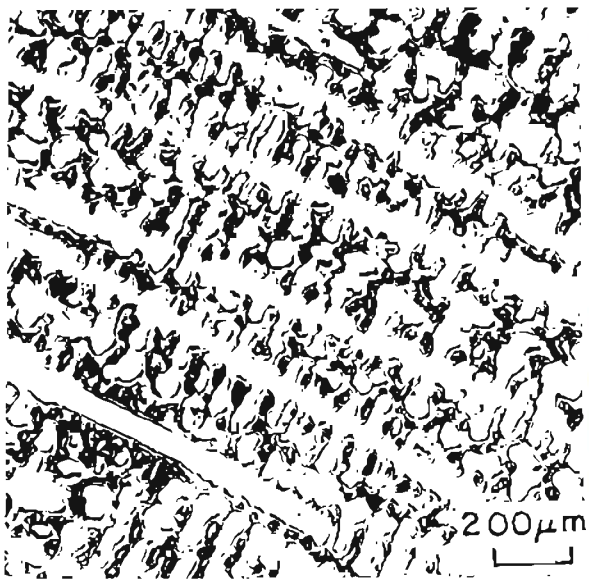

b) Mid radius

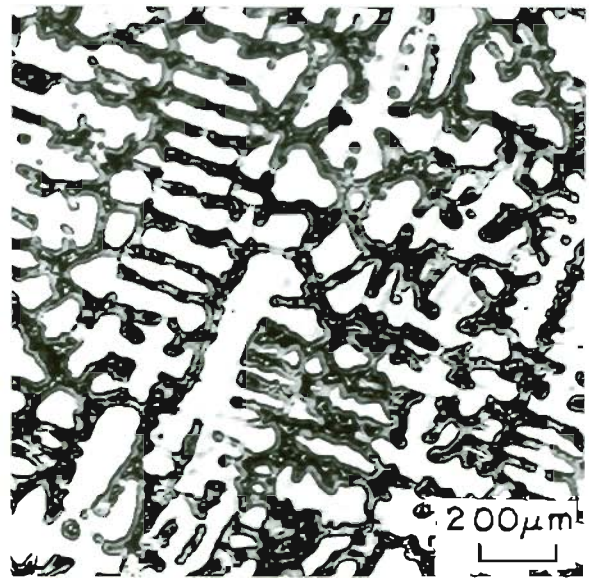

c) Center

Figure 5.47. Photomicrographs of dendritic structure for melt number 47.

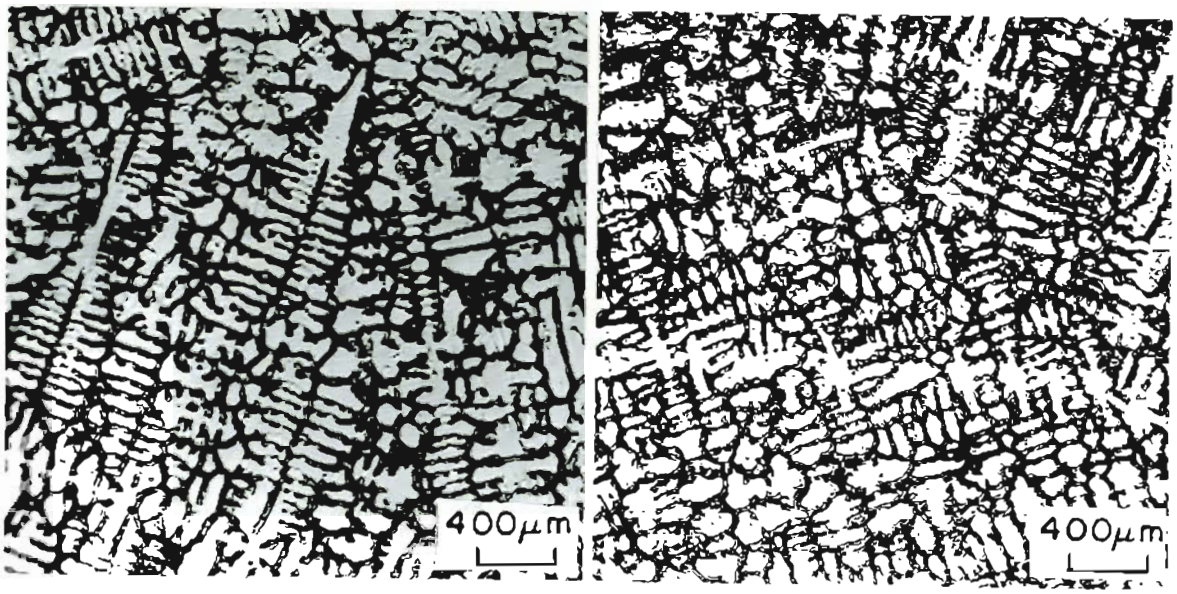

a) Melt number 47 (no gas cooling) b) Melt number 49 (40 mm Hg helium gas)

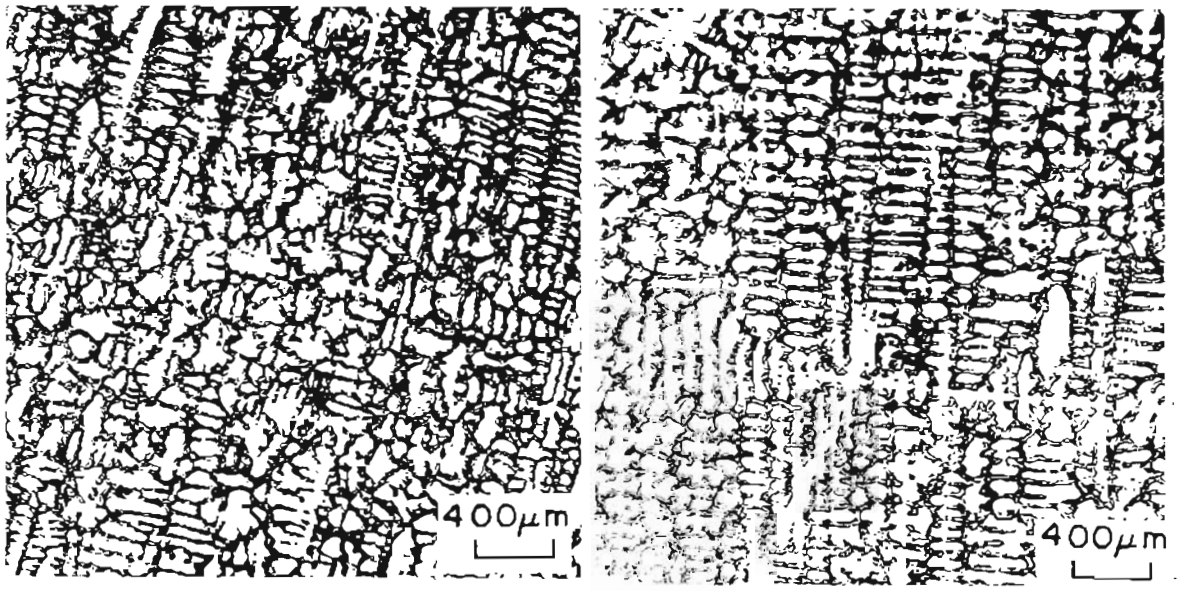

c) Melt number 50 (60 mm Hg Helium gas) d) Melt number 53 (60 mm Hg argon)

Figure 5.48. Photomicrographs of dendritic structure at the center of ingots

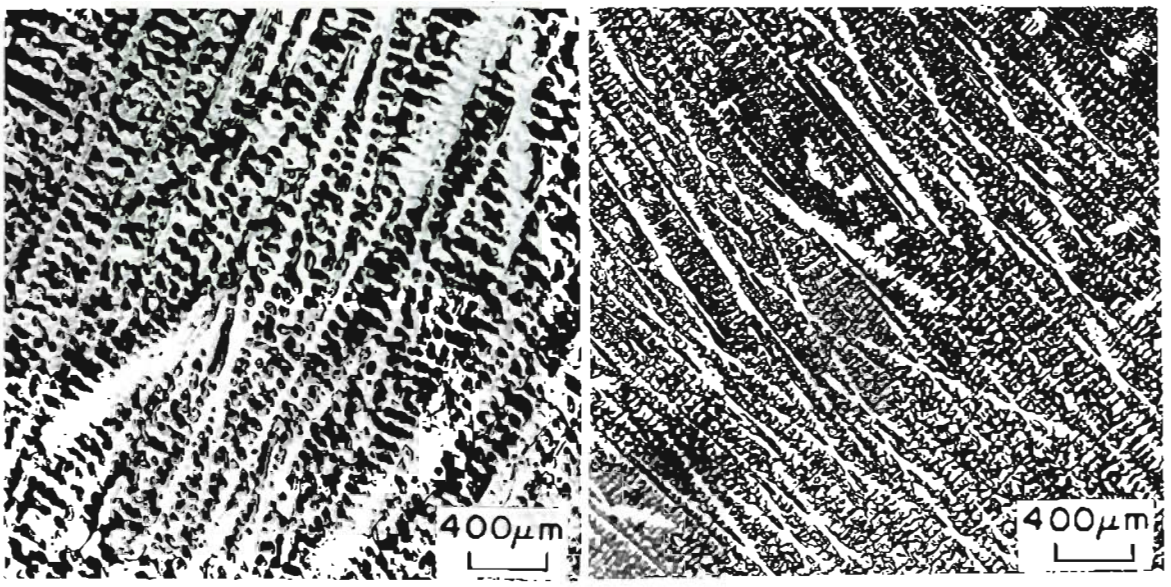

a) Melt number 47 (no gas cooling) b) Melt number 49 (40 mm Hg helium gas)

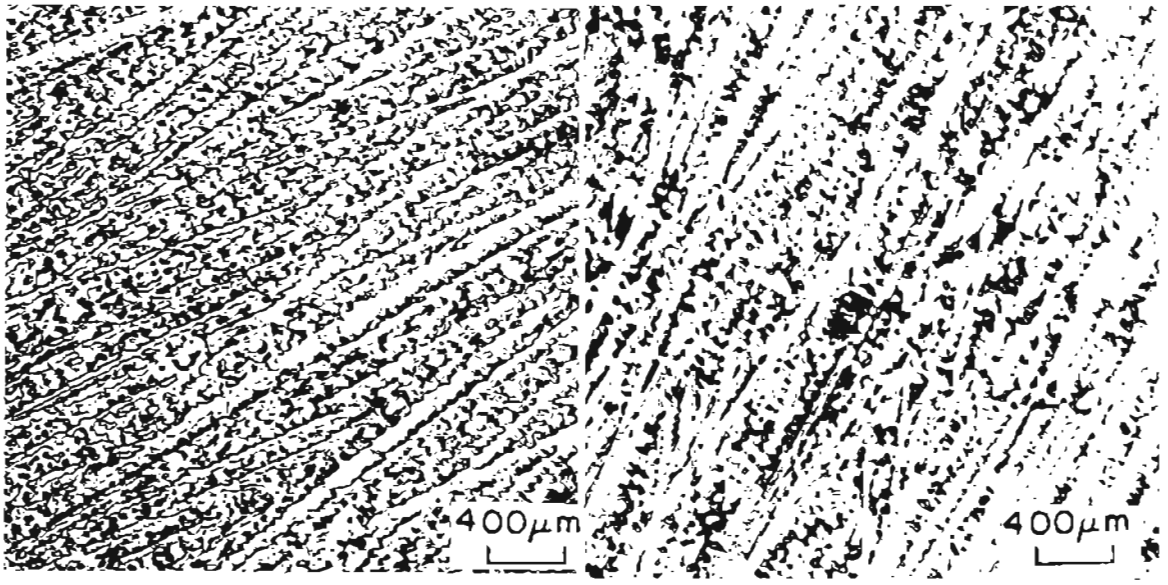

c) Melt number 50 (60 mm Hg helium gas) d) Melt number 53 (60 mm Hg argon)

Figure 5.49. Photomicrographs of dendritic structure at the edge of ingots.

TABLE 5.13

DENDRITE ARM SPACING MEASUREMENTS IN MICRON

Melt No.	Dendrite Arm Spacings in μ		
	Edge	Mid radius	Center
47	63.6	66.6	74.0
49	47.0	53.2	58.9
50	42.5	52.2	55.7
53	55.2	60.0	62.3

53) was higher than the cooling rate at the edge of ingot with no gas cooling (number 47)

5.2.2.7. Mushy Zone Size

The mushy zone size and shape was estimated using the data of secondary dendrite arm spacing. Dendrite arm spacing is related to the local cooling rate by (75),

$$d = a \left[\frac{\partial T}{\partial t}\right]^{-n} \tag{5.76}$$

where,

d = primary or secondary dendrite arm spacing

a, n = constants (different constants for primary and secondary)

$\frac{\partial T}{\partial t}$ = local cooling rate.

Mushy zone is then related to dendrite arm spacing by (75),

$$Z_L - Z_S = \Delta T \, R \, (d/a)^{-n} \tag{5.77}$$

where,

$Z_L - Z_S$ = height of mushy zone at a given distance

ΔT = liquidus minus solidus temperature of the alloy

d = measured secondary dendrite arm spacing

a, n = constants (as above)

R = velocity of solidification front

For Inconel 718, a = 33.85 and n = 0.338, for secondary dendrite arm spacing (76) and $\Delta T = 65^{\circ}C$

For melt number 49, the velocity of solidification front at the center of ingot

was 0.1211 mm/second, and the measured secondary dendrite arm spacing was 58.9μ . This gives the mushy zone depth as,

$$\text{Mushy zone depth} = 65 \times 0.1211 \left(\frac{58.9}{33.85}\right)^{-.338}$$

$$= 40.5 \text{ mm}$$

The velocity of solidification front at mid radius and edge of the ingot was calculated using $R_{midradius} = R_{center} \times \cos 23$ and $R_{edge} = R_{center} \times \cos 45$. The calculated depth of mushy zone sizes for all the melts is shown in Table 5.14. It can be seen that, the mushy zone depth decreases with the helium gas cooling. Ballantyne (47) has reported the predicted effect of helium gas cooling on the mushy zone depth in VAR for a 1000mm diameter ingot melted with 1000 kg/hr melt rate. The mushy zone depth was found to decrease from 140 mm with no gas cooling to 110 mm with 10 mm Hg of helium gas cooling. In the present investigation, for 165 mm diameter ingot the mushy zone depth decreased from 54.75 mm with no gas cooling to 36 mm with 60 mm gas cooling. Hence, the experimental observation of the present investigation is in agreement with the trend predicted by Ballantyne.

Local Solidification Time (LST).

The local solidification time was calculated using,

$$\Delta t_s = \frac{\text{Depth of mushy zone}}{\text{Rate of solidification}} \tag{5.78}$$

The calculated values of local solidification time at the edge, mid radius and center of all the ingots are shown in Table 5.15. The data indicates that helium gas cooling tends to decrease the local solidification time. Ballantyne and Mitchell

TABLE 5.14

MUSHY ZONE SIZE IN MM

Melt No.	Mushy Zone Size in mm		
	Edge	Mid radius	Center
47	24.7	36.9	54.75
49	14.7	27.6	40.5
50	11.4	27.4	36
53	20.3	33.8	41.0

TABLE 5.15

LOCAL SOLIDIFICATION TIME IN SECONDS

Melt No.	Local solidification time in secs.		
	Edge	Mid radius	Center
47	420	480	657
49	170	247	335
50	127	234	283
53	276	353	394

(77-79), have made an attempt to relate local solidification time to solidification structure for Inconel 718. They have estimated that (77), under VAR, ESR and PAR solidification conditions, the LST must be less than 1200 seconds for the Laves phase to be restricted to less than 5% by volume. In the present investigation, the local solidification time were calculated to be lower than 1200 seconds. Hence no serious macro-segregation was expected.

5.2.2.8. Laves Phase

Figure 5.50 shows a colored photomicrograph of the distribution of the eutectic Laves phase. The above figure shows the dendrite core, interdendritic region, Laves phase, carbide and delta phase. Figure 5.51 shows the Laves phase distribution in the center of the ingot with no gas cooling and with various gas cooling conditions. It can be seen that, the amount of Laves phase is highest in melt no. 47 which was done with no gas cooling and lowest in melt 50 which was done with 60 mm helium gas cooling. This could be explained in terms of finer dendritic structure for melt 50 as compared to melt 47. The metal pool and mushy zone were smaller for melt 50. Reduced amounts of Laves phase means niobium is more uniformly distributed in the ingot.

5.2.2.9. Segregation Studies

Table 5.16 shows the SEM/EDAX analysis of dendrite core, interdendritic region and Laves phase for melts with no gas cooling and with gas cooling at various pressures. It can be seen from the table that the eutectic Laves phase contains about 26.4% Nb. There is no significant difference in the Nb content of the Laves phase observed in the melts with gas cooling and without gas cooling.

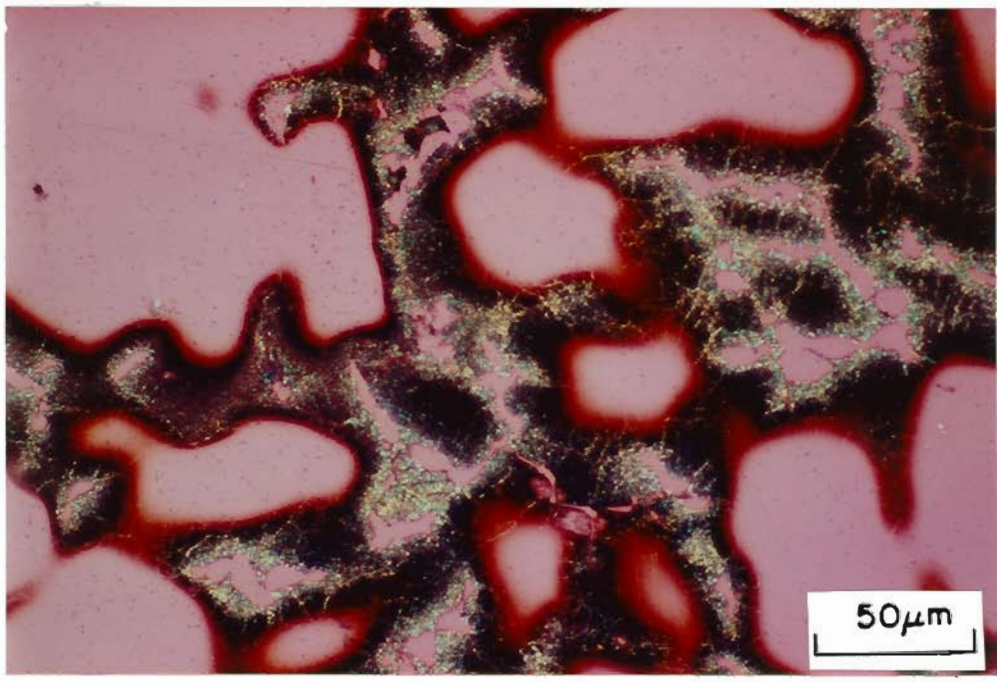

Figure 5.50. Coloured photomicrograph of Laves phase distribution in melt number 47.

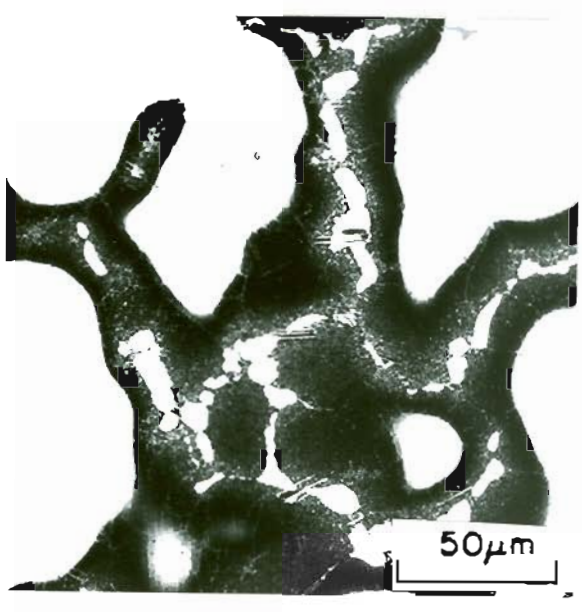

a) With no gas cooling

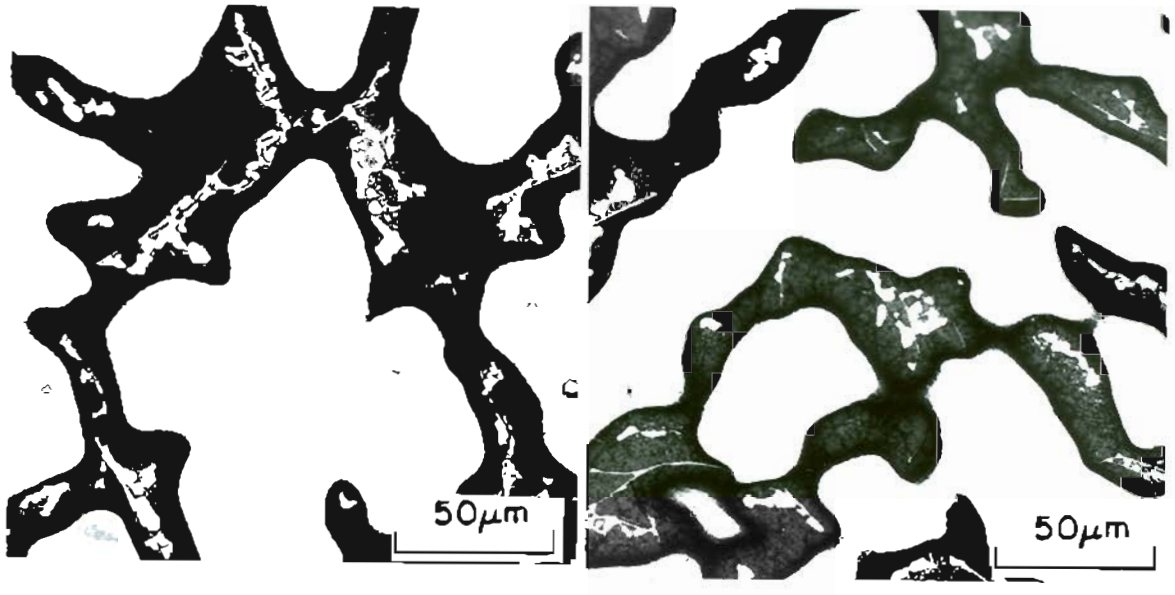

b) with 40 mm Hg helium gas cooling c) with 60 mm Hg helium gas cooling

Figure 5.51. Photomicrographs of Laves phase distribution at the center of ingots.

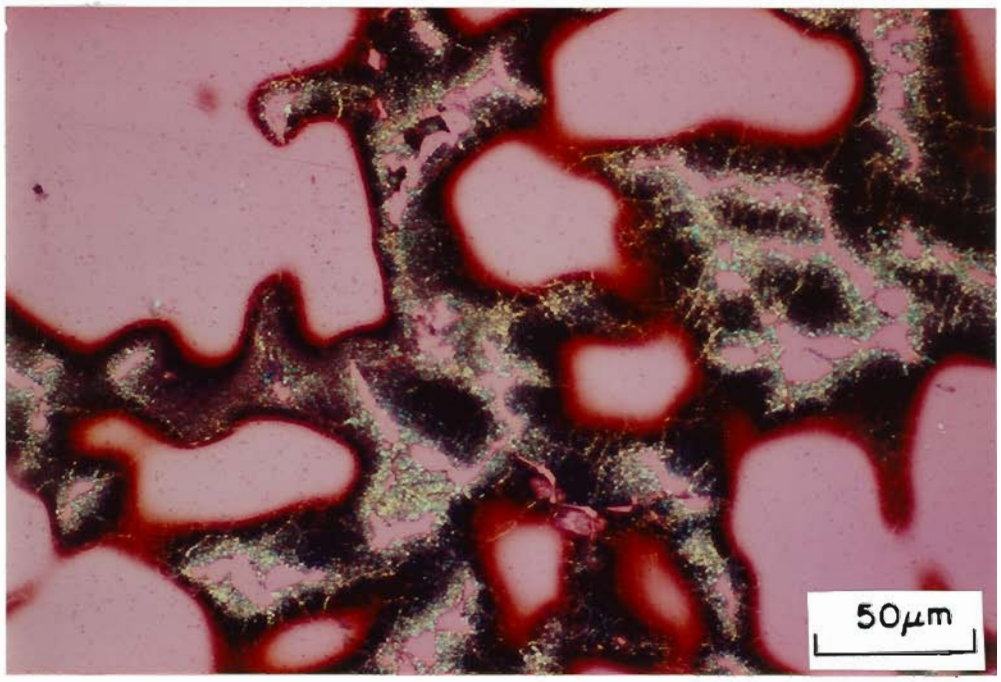

Figure 5.50. Coloured photomicrograph of Laves phase distribution in melt number 47.

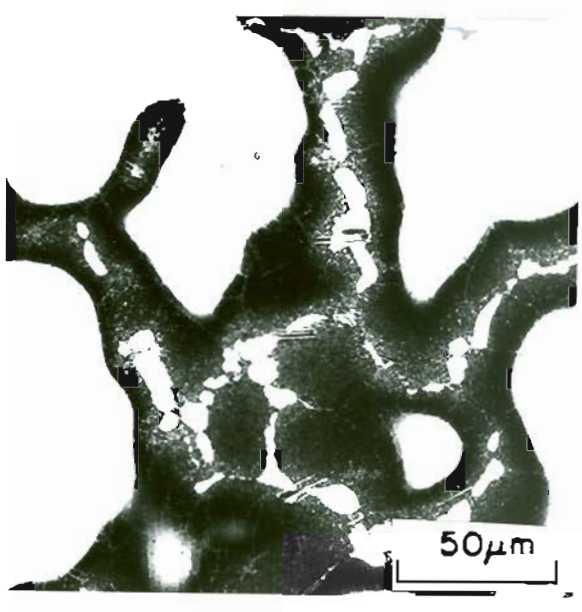

a) With no gas cooling

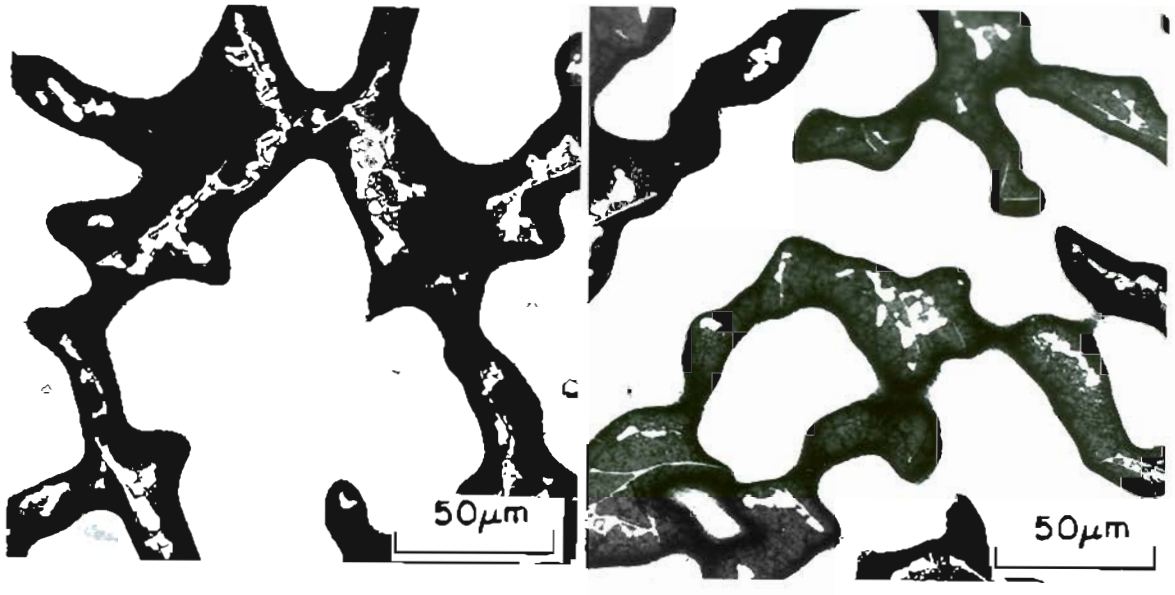

b) with 40 mm Hg helium gas cooling c) with 60 mm Hg helium gas cooling

Figure 5.51. Photomicrographs of Laves phase distribution at the center of ingots.

TABLE 5.16

SEM/EDAX OF DENDRITE CORE, INTERDENDRITIC REGION AND LAVES PHASE

Element	Dendrite Core	Interdendritic Region	Laves Phase
	MELT NUMBER 47 (NO GAS COOLING)		
Ni	56.9	57.5	45.4
Fe	19.7	14.9	11.8
Cr	18.3	15.5	12.5
Ti	0.80	1.57	1.10
Nb	2.20	6.51	26.4
	MELT NUMBER 49		
Ni	56.8	57.3	45.9
Fe	19.4	14.9	12.3
Cr	18.2	16.6	12.1
Ti	0.70	1.30	0.98
Nb	1.90	6.20	25.5

Element	Dendrite Core	Interdendritic Region	Laves Phase
	MELT NUMBER 50		
Ni	56.9	56.5	45.7
Fe	20.4	15.2	11.7
Cr	18.1	16.6	12.1
Ti	0.63	1.40	1.25
Nb	1.90	6.80	26.4
	MELT NUMBER 53		
Ni	56.9	58.6	44.6
Fe	20.0	14.9	11.8
Cr	18.3	15.8	12.2
Ti	0.75	1.60	1.11
Nb	1.88	7.40	27.5

In all these cases the analysis was carried out at the center of the ingot. As discussed in the previous section, the amount of Laves phase decreased with gas cooling.

The Nb content of the dendrite core in all the cases is about 2% and the Nb content of the interdendritic region is about 7%. The dendrite cores are the Nb depleted regions with higher concentration of Ni, Cr, and Fe. Ballantyne et al (78) have analyzed the Laves phase formed under various LST values. The Nb content of the Laves phase is 21% with LST = 230 seconds, and 20.1% with LST = 2600 seconds and 30.4% with LST = 1500 seconds. This indicates that there is an intermediate LST value for which the Nb content of the Laves phase is maximum. In the present investigation, the LST values are lower than 1500 seconds. Hence no significant difference in the Laves phase analysis was observed.

Table 5.17 shows the chemical analysis at the edge and center of the ingots made with gas cooling and without gas cooling. It can be seen that there is no difference in the composition at the edge and center of the ingot for all the melts. SEM/EDAX analysis of the unetched specimens was also carried out for chemical analysis on macro-scale at the center, mid radius and edge of the ingots. About 2.5 square mm area was analyzed. This area involved about 10 dendrites. Again there was no significant difference in the chemical composition at various distances from the edge of the ingot in all the cases. As the size of the ingots was only 165 mm diameter, no serious macro-segregation problems were observed. But on the micro-scale the amount of Laves phase formed was decreased with the gas cooling. Hence on bigger size ingots, the gas cooling between the ingot and

TABLE 5.17

CHEMICAL ANALYSIS OF INCONEL 718 MELTS IN WEIGHT PERCENTAGE.

	Electrode		Melt 47		Melt 49		Melt 50	
Element	Edge	Center	Edge	Center	Edge	Center	Edge	Center
C	0.035	0.035	0.035	0.035	0.036	0.034	0.035	0.035
Si	0.11	0.11	0.11	0.11	0.11	0.11	0.11	0.11
Cr	17.6	17.61	17.70	17.68	17.67	17.78	17.62	17.73
Ni	53.34	53.33	53.43	53.38	53.37	53.42	53.51	53.37
Fe	Bal.	Bal.	Bal.	Bal.	Bal.	Bal.	Bal.	Bal.
Mo	2.97	2.98	2.98	2.98	2.99	2.99	2.99	2.98
Nb	5.30	5.38	5.38	5.36	5.39	5.37	5.36	5.37
Ti	1.0	0.99	0.99	0.99	0.98	0.98	0.99	0.99
Al	0.48	0.48	0.48	0.50	0.48	0.48	0.49	0.50
S	0.0014	0.0014	0.0013	0.0012	0.085	0.057	0.0014	0.0014

crucible is expected to minimize the occurrence of macro and micro segregation.

5.2.3. Summary of Results and Discussions.

The results and discussions are summarized as follows.

1. Vacuum Arc furnace was successfully installed and instrumented

2. Regression models for melt rate, metal pool depth and voltage were successfully developed.

3. The predicted melt rate for production VAR furnaces with the regression model was in good agreement with the observed production melt rate.

4. Surface quality of the ingot deteriorated with long electrode gaps. A smooth surface was obtained with high current and short electrode gap.

5. Increasing the magnetic field strength decreases the metal pool depth.

6. Theoretical model for heat transfer by gas conduction between the ingot and crucible was derived from the first principle and heat transfer coefficients were predicted.

7. Using the experimentally measured temperature on the outside of the crucible, heat flux distribution on the crucible was computed. Increased helium gas pressure resulted in increased heat extraction rate. With 60 mm helium gas pressure, the total heat extracted was about 103% as against 86% with no gas cooling.

8. With 60 mm of argon gas pressure in the gap, the amount of heat removed was 96% as compared to 103% with 60 mm helium gas.

9. Molten metal pool depth decreased with the increased gas pressure. With 60 mm helium pressure, the metal pool depth decreased to 12.7 cm from 20.0 cm for no gas cooling, about 36% decrease.

10. Surface quality of the ingot deteriorated slightly with the gas cooling.

11. The dendritic structure became finer with the increased gas pressure at the edge as well as at the center of the ingot. The mushy zone depth and the local solidification time decreased with the gas cooling.

12. The amount of Laves phase formed was decreased with the gas cooling. No difference in the Nb content of the Laves phase with gas cooling and without gas cooling was observed.

6. CONCLUSIONS

Following conclusions are drawn from the present investigation.

- Melt rate model developed based on laboratory experiments closely predicts melt rate for production size ingots. Hence laboratory developed models have potential for extending to large production size ingots.

- The magnetic field strength of the stirring coil influences the metal pool depth and the surface quality of the ingot. But, as the melting current increases, the effect of the magnetic field decreases.

- The theoretical model developed for the heat transfer between the ingot and the crucible for gas conduction, describes the trend observed in the experimental work.

- Helium gas between the ingot and the crucible enhances the heat extraction rate. The heat extraction rate is dependent on the thermal conductivity of the gas, the gas pressure, the flow rate and the gap width between the ingot and the crucible. As the gap width between the ingot and the crucible increases, the heat removal rate decreases. As the size of the ingot increases, the gap width between the ingot and the crucible increases. Hence, the heat extraction rate with gas cooling for large size ingots, may be lower as compared to that for smaller size ingots.

The factors like deep molten metal pool depth, deeper mushy zone size and higher local solidification time, which lead to increased segregation in VAR melted alloys, are decreased with gas cooling. Hence, with gas cooling technique, between the ingot and the crucible, it is possible to minimize segregation in large size ingots.

REFERENCES

1) K. O. Yu, J. A. Dominuge and H. D. Flanders, " Control of Macrosegregation in ESR and VAR Processed IN-718.", 8th International Conference on Vacuum Metallurgy, Austria, 1985, p 1279.

2) M. C. Flemings, " Solidification Processing.", McGraw-Hill, 1974, p 244-252.

3) M. C. Flemings and G. E. Nereo, " Macrosegregation Part I.", Trans. Met. Soc., AIME, 212, 1967, p 1449.

4) M. C. Flemings, R. Mehrabian and G. E. Nereo, " Macrosegregation Part II.", Trans. Met. Soc., AIME, 242, 1968, p 41.

5) M. C. Flemings and G. E. Nereo, " Macrosegregation Part IV.", Trans. Met. Soc., AIME, 242, 1968, p 50.

6) R. Mehrabian, M. Keane and M. C. Flemings, " Interdendritic Fluid Flow and Macrosegregation : Influence of gravity.", Met. Trans., Vol 1, 1970, p 1209.

7) R. A. Beall et al, " Cold Mold Arc Melting and Casting.", Bulletin 646, U.S. Bureau of Mines, Department of the Interior, 1968.

8) K. Bungardt and K. Tromel, " Melting in Arc Vacuum Furnace with Consumable Electrode.", BISI, Translation 3942, 1965.

9) V. V. Tetyukhin et al, " Laws of Obtaining the Required Structure, Composition and Properties of Two Phase Titanium Alloy Ingots in Vacuum Arc Remelting.", Titanium and Titanium Alloys, Scientific and Technological Aspects, Vol 1, Ed. J. C. Williams and A. F. Belov, 1982, p 141.

10) F. J. Zanner et al, " Observations of Melt Rate as a Function of Arc Power, CO Pressure and Electrode Gap during Vacuum Consumable Arc Remelting of

Inconel 718.", Met. Trans., Vol 15B, 1984, p 117.

11) I. V. Samarasekera and J. K. Brimacombe, " The Continuous Casting Mold.", International Metals Reviews, No. 6, 1978, p 286.

12) J. M. Wentzell, " Method for Controlling the Cooling of Cast Metal.", U.S. Patent 3,353,585, 1967.

13) W. E. Kuhn " The Past, Present and Future of Controlled Atmosphere Arcs ", Arcs in Inert Atmospheres and Vacuum, Ed. W. E. Kuhn, 1956.

14) F. J. Zanner and L. A. Bertram, " Vacuum Arc Remelting - An Overview ", 8th International Conference on Vacuum Metallurgy, Austria, 1985, p 512.

15) L. A. Bertram and F. J. Zanner, " Measurement of Ingot-Crucible Boundary Conditions During VAR ", Conf. Proc. on Modelling, Casting and Welding Processes, Eds. G. Dantzig and J. T. Berry, 1984.

16) F. J. Zannner, " Metal Transfer During Vacuum Consumable Arc Melting ", Met. Trans., B , Vol 10B, 1979, p 133-142.

17) F. J. Zanner, " Observation of the Vacuum Arc and Metal Transfer during Vacuum Consumable Arc Remelting ", Proc. Int. Conf. on Special Melting, eds. G. K. Bhat and R. Schlatter, 1979, p 414-427.

18) F. J. Zanner, " Vacuum Consumable Arc Remelting Electrode Gap Control Strategies based on Drop Short Properties ", Met. Trans., Vol 12B, 1981, p 721-728.

19) F. J. Zanner and L. A. Bertram, " Computational and Experimental Analysis of a U-6%Nb Vacuum Consumable Arc Remelt Ingot ", Sandia report, SAND80-1156, 1981.

20) F. J. Zanner, L. A. Bertram, R. Harrision and H. Flanders, " Relationship

between Furnace Voltage Signatures and the Operational Parameters, Arc Power, Arc Current, CO Pressure and Electrode Gap during VAR of Inconel 718 ", Met. Trans, Vol. 17B, 1986, p. 357-365.

21) F. J. Zanner and L. A. Bertram, " Sustained High Current Arcs on Molten Metal Alloy Electrodes during VAR ", IEEE Trans. on Plasma Science, No. 3, 1983, p 223-232.

22) W. Knorr, " Critical Review of Melting and Casting ", IV Int. Conf. on Titanium, Japan, 1980, p 233.

23) M. Schlienger, " Melting System for Production of Titanium Ingots and Castings ", Int. Conf. on Titanium, W. Germany, 1984, p 15.

24) R. Schlatter, " Melting and Refining Technology of High Temperature Steels and Superalloys ", Proc. of 2nd Int. Conf. on Superalloys, 1972.

25) H. L. Eiselstein, " Metallurgy of a Cb Hardened Ni-Cr-Fe Alloy ", Advances in the Technology of Stainless Steels and Related Alloys, ASTM STP 369, 1965, p 62-79.

26) S. Kou, " Macrosegregation in Electroslag Remelted Ingot ", PhD Thesis, MIT, 1978.

27) K. O. Yu, J. A. Domingue, G. E. Maurer and H. D. Flanders, " Macrosegregation in ESR and VAR Processes ", Journal of Metals, Jan 1986, p 46.

28) R. Mehrabian, " Segregation Control in Ingot Solidification " Proc. of the Army Materials Technology Conf. 1972, Ed. J. Burke etal p. 299-315.

29) S. Kou, D. R. Poirer and M. C. Flemings, " Macrosegregation in Electroslag Remelted Ingots ", Electric Furnace Proceedings, 1977, 35, p 221.

30) R. P. DeVries and G. R. Mumau, " Importance of a Relationship between Dendrite Formation and Solidification in Highly Alloyed Materials ", Journal of Metals, 1968, p 33.

31) T. Niimi, M. Miura, S. Matumoto and A. Suzuki, " An Evaluation of the Electroslag Remelted Large Ingot ", 4th Int. Conf. on ESR, Tokyo, 1973, p 322.

32) W. Holzgruber, " Possibilities and Limitations to Influence the Structure of ESR Ingots and Properties of ESR Products ", 5th Int. Conf. on ESR, 1974, p 70.

33) P. Dewsnap and R. Schlatter, " Process and Product Characteristics of DC Electroslag Remelting of Alloy Steels ", 5th Int. Conf. on ESR, 1974, p 91.

34) K. O. Yu and D. H. Flanders, " Comparision of ESR - VAR Processes Part II ", Vacuum Metallurgy Conference on Speciality Melting, Pittsburgh, 1984, p 109.

35) P. O. Mellberg, " Thermal Conditions in the ESR Process ", 6th Int. Conf. on Vacuum Metallurgy, 1979, p 535.

36) F. S. Suarez et al, " Ingot Size Optimization in a Superalloy - Inconel 706 ", 5th Int. Conf. on ESR, 1974.

37) C. F. Jeanfils, J. H. Chen and H. J. Klein, " Temperature Distribution in an ESR Ingot during Transient Conditions ", 6th Int. Vacuum Metallurgy Conf. 1979, p 543.

38) C. L. Jeanfils et al, " Modeling Solidification in an ESR Ingot ", Conf. on Modelling of Casting and Welding Processes, 1980, p 313.

39) A. Mitchell and R. M. Smailer, " Practical Aspects of ESR Technology ", International Metals Reviews, Nos. 5 and 6, 1979, p 231.

40) V. I. Dobatkin and M. I. Musatov, " The Effect of Rate of Filling Moulds on the Solidification of Titanium Alloy Ingots ", Titanium Science and Technology,

Proc. of Conf., eds. R. I. Jaffee and H. M. Burte, 1973, p 319.

41) H. Jacobi, " Heat Transfer between Ingot and Mould during Casting of Iron under Vacuum and Various Gas Atmospheres ", Proc. of 5th Int. Conf. on Vacuum Metallurgy, 1976.

42) Charles R. Taylor, " Continuous Casting Update ", 1975 Howe Memorial Lecture, Met. Trans., Vol 6B, 1975, p 359.

43) K. Cliff and R. J. Dain, " Computerised Calculation of Operating Conditions in Continuous Casting Machines ", JISI 1967, p 278.

44) V. A. Boyarshinov and V. N. Gotin, " Heat Transfer Intensification in the Vacuum Arc Furnace ", Int. Conf. on Heat and Mass Transfer, 1979.

45) V. N. Gotin and V. A. Boyarshinov, " Controlling Cooling of Metal in Vacuum Arc Remelting ", Steel in the USSR, April 1981, Vol II, p 216.

46) K. O. Yu, " Comparision of ESR - VAR Processes - Part I : Heat Transfer Characteristics ", Proc. of Conf. on Vacuum Metallurgy, 1984.

47) A. S. Ballantyne, " Heat Flow in Consumable Electrode Remelted Ingot ", UBC, PhD Thesis, 1978.

48) A. S. Ballantyne and A. Mitchell, " Modelling of Ingot Thermal Fields in Consumable Electrode Remelting Processes ", Ironmaking and Steelmaking, No. 4, 1977, p 222.

49) Yu G. Semyonov, S. F. Borisov and P. E. Suetin, " Investigation of Heat Transfer in Rarefied Gases over a Wide Range of Knudsen Numbers ", Int. Journal of Heat and Mass Transfer, Vol 27, No. 10, 1984, p 1789.

50) Lester Lee and Chung-Yen Liu, " Kinetic Theory Description of Conductive Heat Transfer from a Fine Wire ", Physics of Fluids, Vol 5, No. 5, 1962, p 1137.

51) D. B. Sheldon and G. E. Springer, " Experimental Study of Rarefied Argon Contained between Concentric Cylinders ", Physics of Fluids, Vol 11, No. 6, 1968, p 1312.

52) E. Y. Yu, " Heat Conduction between Concentric Cylinders in the Slip Regime ", Physics of Fluids, Vol 13, No. 10, 1970, p 2484.

53) Alexender Dybbs and George S. Springer, " Heat Conduction Experiments in Rarefied Gases between Concentric Cylinders ", Physics of Fluids, Vol 8, No. 11, 1965, p 1946.

54) Piero Bassanini, Carlo Cercignani and Franco Sernagiatto, " Flow of Rarefied Gas in a Tube of Annular Section ", Physics of Fluids, Vol 9, No. 6, 1966, p 1174.

55) E. P. Gross and S. Ziering, " Heat Flow between Parallel Plates ", Physics of fluids, Vol 2, No. 6, p 701.

56) F. C. Hurlbut, " Note on Conductive Heat Transfer from Fine Wire ", Physics of fluids, Vol. 7, 1964.

57) G. E. P. Box, W. G. Hunter and J. S. Hunter, " Statistics for Experimenters ", J. Wiley and Sons, 1978.

58) C. Chatfield, " Statistics of Technology ", Chapman and Hall, 1983.

59) Smithells Metals Reference Book, Ed. Eric. A. Brandes, 1983.

60) F. I. Shved et al, " Influence of Proccess Parameters on Energy Balance and Thermal Working of Mould in VAR ", Steel in the USSR, Vol 11, 1981, p 516.

61) B. E. Paton et al, " Mathematical Simulation and Prediction of Electroslag Refining of Large Forging Ingots ", Proc. of Int. Conf. on ESR, 1973, p 16.

62) J. Preston, " Pool Size in Vacuum Consumable Electrode Arc Melting of

Alloy Steel Ingots ", Trans. of Conf. on Vacuum Metallurgy, 1964, ed. Micheal A. Cocca, p 366.

63) E. H. Kennard, " Kinetic Theory of Gases ", McGraw-Hill Inc., 1938, p 311-324.

64) Saul Dushman, " Scientific Foundation of Vacuum Technique ", John Wiley and Sons Inc., p 44-58.

65) B. G. Dickens, " The Effect of Accomodation on Heat Conduction through Gases ", Proc. Royal Society of London, 1933, Vol 143A, p 517.

66) Chemical Engineers Handbook, Ed. R. H. Perry and C. H. Chilton, 1973.

67) J. O. Hirschfelder, C. F. Cutiss and R. B. Bird, " Molecular Theory of Gases and Liquids " Wiley, 1964.

68) Warren Ibele, " Modern Developments in Heat Transfer ", Academic Press, 1963.

69) W. M. Rohsenow and H. Y. Choi, " Heat Mass and Momentum Transfer ", Prentice Hall, p 281.

70) I. V. Samarasekara and J. K. Brimacombe, " The Influence of Mold Behavior on the Production of Continuously Cast Steel Billets ", Met. Trans., Vol 13B, 1982, p 105.

71) A. M. Ross and R. L. Stoute, " Heat Transfer Coefficient between UO2 and Zircalloy 2 ", CRFD-1075 Report, 1962.

72) K. Ho and R. D. Pehlke, " Mechanisms of Heat Transfer at Metal Mold Interface ", AFS Transactions, 84-61, p 587.

73) Frank Keith, " Principles of Heat Transfer ", International Textbook Company, 1962.

74) S. Hayashi et al, " Mechanisms of Heat Transfer in Continuous Casting Moulds ", BISI Transational 9318.

75) S. D. Ridder et al, " Steady State Segregation and Heat Flow in ESR ", Met. Trans. B , Vol 9B, 1978, p 415.

76) R. Mehrabian, " Relationship of Heat Flow to Structure in Rapid Solidification Processing ", Int. Conf. on Rapid Solidification, Virginia, 1977, p 9-27.

77) A. S. Ballantyne and A. Mitchell, " Prediction of Structure in Industrial VAR, ESR and PAR Ingots Using Computed Local Solidification Times ", Int. Conf. on Solidification, 1976, p 363.

78) A. S. Ballantyne et al, " The Prediction of Ingot Structure in VAR/ESR Inconel 718 ", Int. Conf. on Vacuum Metallurgy, 1979, p 599.

79) A. Mitchell and A. S. Ballantyne, " Factors Affecting Solidification and Ingot Temperatures in ESR ", Int. Conf. on Vacuum Metallurgy, 1979, p 569.

80) D. Hiatt, Oregon Metallurgical Corporation, Albany, Oregon, Personal Communication,1987.

APPENDIX

```
C PROGRAM TO CALCULATE HEAT FLUX ON THE CRUCIBLE WALL
C
C     FUNCTION WHICH CALCULATES F1
      DOUBLE PRECISION FUNCTION F1(X)
C
      EXTERNAL H
      EXTERNAL T
      DOUBLE PRECISION X,H,T
      INTEGER I
      F1 = H(T(X)) * (T(X) -17)
      RETURN
      END

C
      EXTERNAL F1
      EXTERNAL H,T
      DOUBLE PRECISION X,H,T,F1
      INTEGER NCP,NK,NMU,NT
      DOUBLE PRECISION XCP(10),YCP(10),BCP(10),CCP(10),DCP(10)
      DOUBLE PRECISION XK(10),YK(10),BK(10),CK(10),DK(10)
      DOUBLE PRECISION XMU(10),YMU(10),BMU(10),CMU(10),DMU(10)
```

```
      DOUBLE PRECISION XT(15),YT(15),BT(15),CT(15),DT(15)
      COMMON /CPSPL/ NCP,XCP,YCP,BCP,CCP,DCP
      COMMON /KSPL/ NK,XK,YK,BK,CK,DK
      COMMON /MUSPL/ NMU,XMU,YMU,BMU,CMU,DMU
      COMMON /TSPL/ NT,XT,YT,BT,CT,DT
      DOUBLE PRECISION X1,X2,ABSERR,RELERR,HF,ERREST,FLAG
      INTEGER NOF1,I

C
      CALL LOADSP
      DO 10 I = 1,15
      WRITE(6,200) XT(I), T(XT(I)),H(T(XT(I))),F1(XT(I))
   10 CONTINUE
      RELERR = 1.0D-10
      ABSERR = 1.0D-10
      X1 = 0.0001
      X2 = 1.02
      CALL QUANC8(F1,X1,X2,ABSERR,RELERR,HF,ERREST,NOF1,FLAG)
      WRITE(6,100) HF
  100 FORMAT(6H HF = ,F20.5)
  200 format(4f12.3)
      STOP
      END
```

```
      SUBROUTINE LOADSP

C     SI UNITS
      DOUBLE PRECISION XCP(10),YCP(10),BCP(10),CCP(10),DCP(10)
      DOUBLE PRECISION XK(10),YK(10),BK(10),CK(10),DK(10)
      DOUBLE PRECISION XMU(10),YMU(10),BMU(10),CMU(10),DMU(10)
      DOUBLE PRECISION XT(15),YT(15),BT(15),CT(15),DT(15)
      INTEGER NCP,NK,NMU,NT
      COMMON /CPSPL/ NCP,XCP,YCP,BCP,CCP,DCP
      COMMON /KSPL/ NK,XK,YK,BK,CK,DK
      COMMON /MUSPL/ NMU,XMU,YMU,BMU,CMU,DMU
      COMMON /TSPL/ NT,XT,YT,BT,CT,DT
      INTEGER I,J


      NCP = 10
      NK = 10
      NMU = 10
      NT = 15
      DATA XCP/10,20,30,40,50,60,70,80,90,100/
      DATA YCP/4193,4182,4180,4179,4182,4186,4191,4195,4203,4215/
      DATA XK/10,20,30,40,50,60,70,80,90,100/
      DATA YK/0.582,0.5996,0.6150,0.6286,0.6405,0.6507,0.6594,0.6668,0.6
     +727,0.6775/
      DATA XMU/10,20,30,40,50,60,70,80,90,100/
```

```
      DATA YMU/1308,1003,797.8,653.1,547.1,466.8,404.4,355,315,282.2/
      DO 50 J=1,10
        YMU(J) = YMU(J) / 1000000 50    CONTINUE
      DATA XT/0.0001,5.08,10.16,15.24,20.32,25.4,31.75,33.0,38.1,43
     +.2,48.25,53.3,58.4,63.5,102/
      DATA YT/22,24,32,35,41,58,90,96,71,55,39,32,24,24,20/

      DO 100 I=1,15
        XT(I) = XT(I) / 100
  100 CONTINUE
      CALL SPLINE (NCP,XCP,YCP,BCP,CCP,DCP)
      CALL SPLINE (NK,XK,YK,BK,CK,DK)
      CALL SPLINE (NMU,XMU,YMU,BMU,CMU,DMU)
      CALL SPLINE (NT,XT,YT,BT,CT,DT)
      RETURN
      END


C     FUNCTION WHICH CALCULATES CP
C
      DOUBLE PRECISION FUNCTION CP(T)
C
      INTEGER NCP
      DOUBLE PRECISION XCP(10),YCP(10),BCP(10),CCP(10),DCP(10)
      COMMON /CPSPL/ NCP,XCP,YCP,BCP,CCP,DCP
```

```
      DOUBLE PRECISION T,SEVAL C
      CP = SEVAL(NCP,T,XCP,YCP,BCP,CCP,DCP)
      RETURN
      END


C     FUNCTION WHICH CALCULATES MU
C
      DOUBLE PRECISION FUNCTION MU(T)
C
      INTEGER NMU
      DOUBLE PRECISION XMU(10),YMU(10),BMU(10),CMU(10),DMU(10)
      COMMON /MUSPL/ NMU,XMU,YMU,BMU,CMU,DMU
      DOUBLE PRECISION T,SEVAL C
      MU = SEVAL(NMU,T,XMU,YMU,BMU,CMU,DMU)
      RETURN
      END

C     FUNCTION WHICH CALCULATES K
C
      DOUBLE PRECISION FUNCTION K(T)
C

      INTEGER NK
      DOUBLE PRECISION XK(10),YK(10),BK(10),CK(10),DK(10)
      COMMON /KSPL/ NK,XK,YK,BK,CK,DK
```

```
      DOUBLE PRECISION T,SEVAL C
      K = SEVAL(NK,T,XK,YK,BK,CK,DK)
      RETURN
      END

C     FUNCTION WHICH CALCULATES T
C
      DOUBLE PRECISION FUNCTION T(X)
C
      INTEGER NT
      DOUBLE PRECISION XT(15),YT(15),BT(15),CT(15),DT(15)
      COMMON /TSPL/ NT,XT,YT,BT,CT,DT
      DOUBLE PRECISION X,SEVAL C
      T = SEVAL(NT,X,XT,YT,BT,CT,DT)
      RETURN
      END

C     FUNCTION WHICH CALCULATES H
C
      DOUBLE PRECISION FUNCTION H(T)
C
      DOUBLE PRECISION T,TAVG
      DOUBLE PRECISION CP,K,MU
      DOUBLE PRECISION PR,RE,G,DH
      DH = 0.036
```

```
G =246
TAVG = (T + 18)/ 2
PR = MU(TAVG) * CP(TAVG) / K(TAVG)
RE = G * DH / MU(TAVG)
H = 0.023 * (CP(TAVG) * G /(PR ** (.667))) / (RE ** (0.2))
RETURN
END
```

BIOGRAPHICAL NOTE

The author was born on May 10, 1951 in Kalliguddi, India. He graduated from School in 1967 from Kaujalagi, India. He attended the Regional Engineering College at Surathkal and received B. E. degree in Metallurgical Engineering in 1973. In 1975 the author received M. Tech. from I. I. T. Bombay, India. In August 1975, the author accepted a position with Indian Tools Bombay to develop Electro Slag Remelting technique. He left Indian Tools in April 1976 and accepted a position with Mishra Dhatu Nigam Ltd., Superalloys plant where he served as a melting engineer in various capacities. In January 1984, the author enrolled at the Oregon Graduate Center, Beaverton Oregon and completed the requirements for his Ph.D. degree in Materials Science and Engineering in April 1988. The author is currently with Precision Castparts Corp., Portland, Oregon.